Investigations of Metal-Organic Frameworks (MOFs) in Bulk and Nanoscale

A Thesis Submitted for the Degree of

Master of Science (Engg.)

By

NIVEDITA SIKDAR

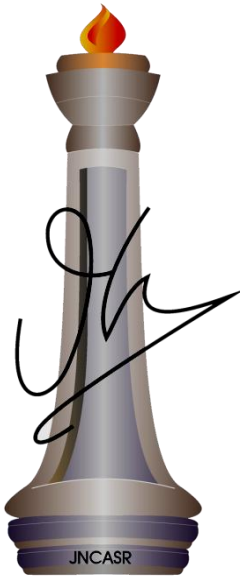

Chemistry and Physics of Materials Unit (CPMU)

Jawaharlal Nehru Centre for Advanced Scientific Research

(A Deemed University)

Bangalore – 560064

Dedicated
to My Beautiful
Family

DECLARATION

I hereby declare that the matter embodied in the thesis entitled "***Investigations of Metal-Organic Frameworks (MOFs) in Bulk and Nanoscale***" is the result of investigations carried out by me at the Chemistry and Physics of Materials Unit, Jawaharlal Nehru Centre for Advanced Scientific Research, India under the supervision of Prof. Tapas Kumar Maji and that it has not been submitted elsewhere for the award of any degree or diploma.

In keeping with the general practice in reporting the scientific observations, due acknowledgement has been made whenever the work described is based on the findings of other investigators. Any omission that might have occurred due to oversight or error in judgement is regretted.

Nivedita Sikdar

CERTIFICATE

I hereby certify that the work described in this thesis entitled "***Investigations of Metal-Organic Frameworks (MOFs) in Bulk and Nanoscale***" has been carried out by Nivedita Sikdar under my supervision at the Chemistry and Physics of Materials Unit, Jawaharlal Nehru Centre for Advanced Scientific Research, India and that it has not been submitted elsewhere for the award of any degree or diploma.

Prof. Tapas Kumar Maji

CPMU, JNCASR

(Research Supervisor)

ACKNOWLEDGEMENT

It is my great pleasure to express my sincere gratitude to my research supervisor, Prof. Tapas Kumar Maji. I am thankful to him for all his support, criticism, guidance and invaluable suggestions, which I have been experienced all through the course of these investigations. I have had enough freedom to work on my own area of interest, and I am grateful to him for that. I am thankful to him for giving me an opportunity to work under his guidance.

Prof. C. N. R. Rao has always been a constant source of inspiration, with all his extraordinary enthusiasm and energy.

I would like to sincerely thank Dr. Debajyoti Ghoshal (Jadavpur University) for E.P.R measurements and Dr. Subi Jacob George for fruitful discussions.

I thank past and present chairmen of CPMU and NCU (Prof. C. N. R. Rao, Prof. G. U. Kulkarni, Prof . S. Balasubramanian) for allowing me to use the various facilities in the center.

I am thankful to the faculty members of JNCASR and Indian Institute of Science (IISc) for the wonderful courses that have been really enjoyable with the pleasure to learn new things. In particular, I would like to thank Prof. S. Balasubramanian, Prof. A. Sundaresan, Prof. T. K. Maji, of JNCASR and Prof. T. N. Guru Row of IISc for their courses.

I am thankful to the technical staffs namely Mr. Anil, Mr. Vasu, Mr. Mahesh, Ms. Selvi, Mr. Shiva, and Mrs. Usha of JNCASR for their prompt and willing assistance, during various experiments.

I thank JNCASR Library, Complab, Hostel, Health Centre, Academics and Administrative staffs for providing and maintaining all the helpful facilities.

I am grateful to my labmates Mr. Jayramulu, Mr. Arpan Hazra, Mr. Ritesh Haldar, Ms. Anindita Chakraborty, Mr. Venkata Suresh, Mr. Syamantak Roy, Ms. Papri Sutar, Ms. Komal Prasad and also my past labmates: Dr. Prakash Kanoo, Dr. Sudip Mohapatra

for providing a nice and healthy environment in the lab. It has been really very helpful to learn many things from them and their unlimited help during measurements.

I would like to thank Mr. Jiaul Hoque, Ms. Sunita Dey, Mr. Abhijit Saha, Mr. Somnath Ghara, Ms. Bhavani N and Mr. Bharath R for their help during various measurements.

I am honoured to acknowledge my all school, college and university teachers for building not only my academic career at initial stage but also to nourish the moral character.

I am cordially thankful to my very special friends Mrs. Minati Sikdar, Mrs. Nabanita Sikdar, Ms. Mitali Kundu, Ms. Anamika Pramanik, Ms. Sunita Dey, Ms. Anindita Chakraborty and Ms. Papri Sutar for their constant support, help and being very nice to me.

My heartfelt thanks to my lovely parents: Maa (Mrs. Minati Sikdar), Baba (Mr. Ashim Sikdar), my sweet elder sister: Didi (Mrs. Nabanita Sikdar), and my brother-in law (Dr. Abhijit Das) for being the greatest strength for me always. Words are indeed insufficient to acknowledge them. They have been tremendous loving, caring, supportive to me and always showed me the right way to take any decision to go forward.

Last but not the least, I would like to express my gratitude to My Dear God, My Almighty for blessing me with constant help at any time along with a perfect family members, very inspiring teachers, true friends and a peaceful life.

PREFACE

Chapter 1 gives a brief overview of functional metal-organic frameworks (MOFs) or Porous Coordination Polymers (PCPs) at bulk and nanoscale, discusses their importance, properties and applications.

Chapter 2 reports a strategic size and shape-controlled fabrication of bulk $\{[Zn_2(H_2dht)(dht)_{0.5}(azpy)_{0.5}(H_2O)]\cdot 4H_2O\}_n$ (**1**) [H_4dht = 2,5-dihydroxyterephthalic acid; (azpy) = 4,4′-azobipyridine] MOF into nano MOF (NMOF) adopting coordination modulation method. This experiment has been followed up preferring two completely different types of modulators (sodium formate/dodecanoic acid with long alkyl chain). It has been possible to modulate different sized and shaped nanoparticles, from nanosheet to hexagonal disks or spherical particles with dramatic increase in surface area. Gas sorption measurements revealed size and shape dependent unprecedented off/on N_2 uptake and different CO_2 uptake characteristics. Furthermore, highly luminescent isomorphous compound has been synthesised in bulk as well as in nanoscale. Solvatochromism has been performed with this isomorphous nanocrystal and studied in details.

Chapter 3 describes synthesis, structural characterizations and gas storage properties of two new two-fold interpenetrated 3D frameworks $\{[Zn_2(bpdc)_2(azpy)]\cdot 2H_2O\cdot DMF\}_n$ (**1**) and $\{[Zn_3(bpdc)_3(azpy)]\cdot 2DEF\}_n$ (**2**) [bpdc = biphenyl dicarboxylate; azpy = 4,4′-azobipyridine] from mixed linker systems. The two different SBUs, paddle-wheel for compound **1** and trinuclear for compound **2,** direct the network topologies and the corresponding porosity in the systems. Both of the frameworks show structural flexibility and selective CO_2 uptake properties at 195 K. Furthermore compound **1** has been fabricated in nanoscale as a spherical morphology through coordination modulation method which exhibits higher uptake of CO_2 compared to bulk form. Kinetic measurements based on water vapor suggest greater diffusion rate

for the nanoparticles compared to bulk, suggesting the smaller diffusion barrier and higher uptake of CO_2 at nanoscale.

Chapter 4 depicts a new strategy to control the interpenetration in MOFs by simple rational designing of organic building blocks based on dicarboxylic acid. In general, it has been observed that 3D framework with α-Po type network topology with paddle-wheel type SBU undergoes interpenetration. Such as, framework $\{[Zn_2(bdc)_2(bpNDI)]\cdot 4DMF\}_n$ (**1**) [bdc = 1,4-benzenedicarboxylic acid; bpNDI = *N*,*N*′-dipyrid-4-yl-1,4,5,8-naphthalenediimide] is interpenetrated due to presence of 1,4-dicarboxylic acid (bdc) and long linker bpNDI. Hence , simply replacing bdc by bulky 9,10-anthracenedicarboxylic acid (adc) (which is acting as strut-impenetrable scaffolds) has led to highly desired noncatenated frameworks $\{[Zn(adc)(bpNDI)_{0.5}]\cdot 2H_2O\cdot DMF\}_n$ (**2**) with higher void space in a controlled fashion. Adsorption isotherms also prove and support their structural features. Additionally, **2** exhibits long range electron transfer from donor adc to acceptor bpNDI through coordination bonds.

Chapter 5 reports the synthesis, structural characterizations of a redox active, luminescent, porous, 2-fold interpenetrated, three dimensional framework $\{[Cd(bpdc)(bpNDI)]\cdot 4H_2O\cdot DMF\}_n$ (**1**) (bpdc = biphenyl dicarboxylate; bpNDI = *N*,*N*′-dipyrid-4-yl-1,4,5,8-naphthalenediimide) using mixed linker systems. The framework shows SBU directed high rigidity and exhibit highly selective CO_2 uptake properties at 195 K. A detailed photophysical study has been performed considering the photoactive framework strut bpNDI. The framework shows blue emission due to MLCT (from bpdc to metal Cd^{II}) along with negligible interactions between host units. A guest induced strong host-guest interaction has been realized through complete one electron transfer from electron rich aromatic guest (like 1,5-or 2,6-dinaphthol, DMPT) to electron deficient bpNDI. Fairly strong confinement effect between host and guest units has been considered as suitable explanation for this kind of phenomenon.

Table of Contents

Chapter 1

Introduction

1.1 Metal-Organic Frameworks (MOFs): An Overview

Metal-organic frameworks (MOFs) are novel class of crystalline hybrid materials [1–3] existing as infinite array of metal ions or clusters (Fig. 1) and organic struts, connected by coordination bonds.[4] These are mostly porous frameworks with well-defined nanoscale tunable channels. It has drawn considerable attention because a large number of framework structures of different topologies would be possible to obtain through exploitation of both organic and inorganic components. The frameworks are modular in nature and can be prepared by mild synthetic conditions.[5] Organic molecules provide tunable shape, size, and functionality and the inorganic elements provide the potential for similar properties to traditional zeolites, including thermal and mechanical stability,[6] as well as optical,[7] magnetic[8] and electronic properties.[9,10]

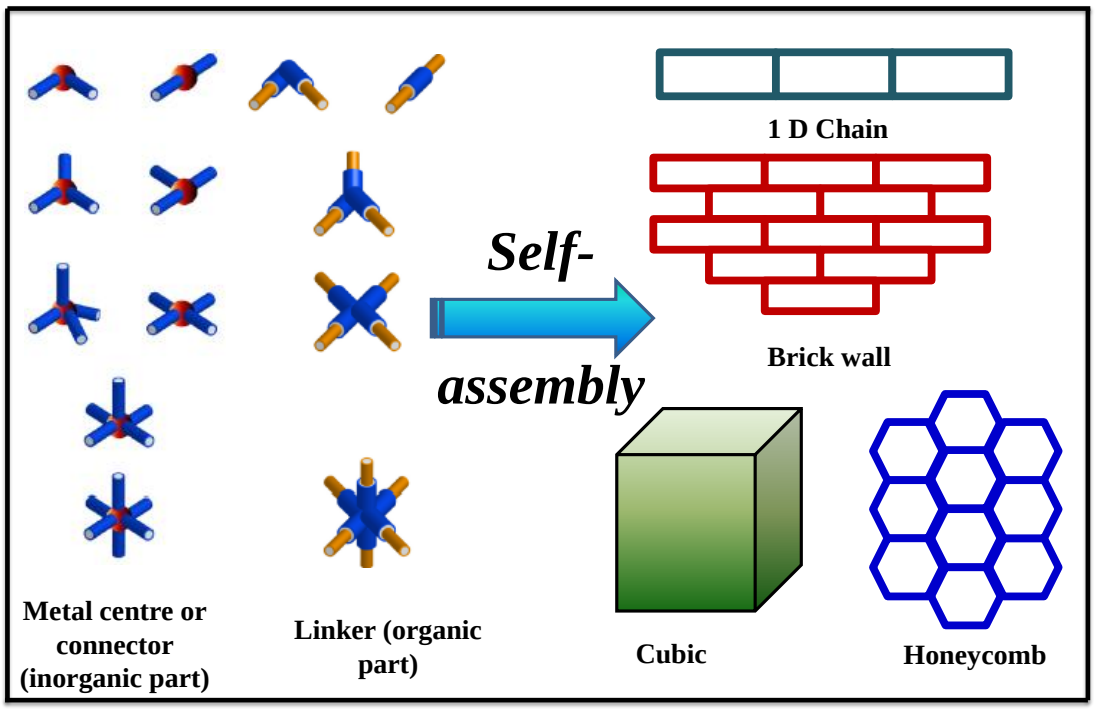

Fig. 1: Construction of different extended architectures by using metal ions and organic bridging ligands *via* coordination driven self-assembly process.

1.2 Synthetic Procedures

The synthesis of MOFs is straightforward, well-soluble metal salts e.g. metal nitrates, sulfates or acetates in combination with organic linkers, which mostly are mono-, di-, tri- and tetracarboxylic acids or amine based linkers, are assembled in water/organic solvents or mixture. After combinat' ion of these inorganic and organic components in appropriate proportion under stirring, the MOFs are synthesized at room temperature or under hydro/solvothermal conditions. Several conditions such as stoichiometry, nature of metals, structure of ligands, temperature, solvent and pH etc. also play crucial role in determining the final structure of the resulting MOFs. Recently, more advanced techniques such as microwave, sonochemical, and mechanochemical syntheses, have been adopted for the improved synthesis of MOFs.[11]

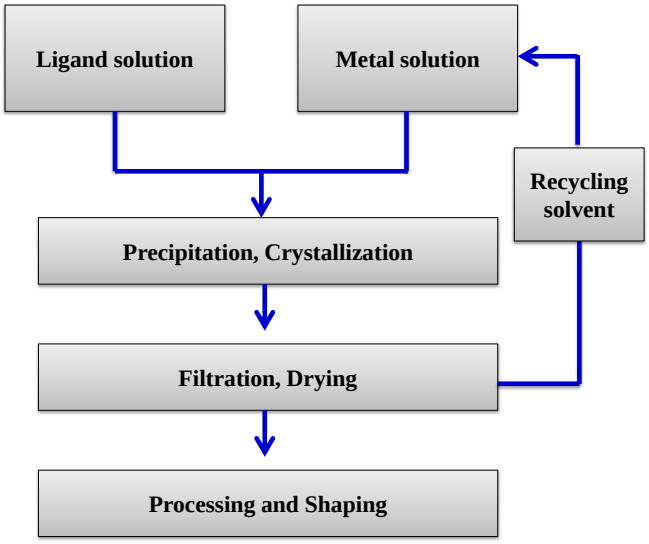

Flow Chart: Simplified flow diagram of bulk scale synthesis of metal–organic framework synthesis procedures

1.3 Classifications of MOFs

MOFs can be 1D, 2D, or 3D depending upon geometry and also the binding mode, shape, symmetry of the organic linkers. In 1998, Kitagawa *et al.* classified MOFs into three categories, viz. first, second and third generations (Fig. 2) depending on their structural response upon guest removal or exchange.[12a,b] The first-generation materials

are those, whose structure collapse irreversibly after removal of the guest molecules, which means, there is no permanent porosity in the framework. The second generation has stable and robust frameworks, which maintain the original porous structures after the guest removal. The second-generation compounds can be used as an adsorbent and are regarded as analogous to zeolites. The third-generation compounds have flexible or dynamic porous frameworks, which reversibly respond to external stimuli, not only chemical but also physical. A wide range of chemistry can be exploited with the third-generation porous solids.

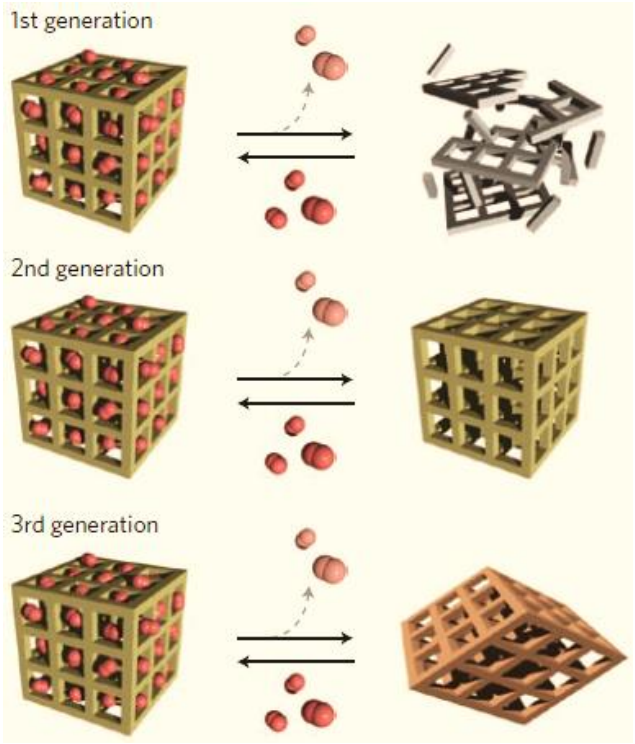

Fig. 2: Classification of MOFs into three generations, first, second (rigid) and third (flexible) based on their structural response upon guest removal. From reference 12b. Reproduced by permission of Nature.

1.4 Rigid and Flexible Frameworks

The most characteristics difference between rigid and flexible MOFs (FMOFs) lies in the predictability of their solid state properties. This fine line between rigid and FMOFs is highly dependent on the functional group and length of the constituting ligand. The rigid frameworks contains very regular and open channel and hence a wide range of

guest molecules could be accommodated, hence good materials for storage applications. For example, Yaghi *et al.* showed a strategy based on reticulating metal ions and organic carboxylate linkers into rigid 3D extended networks possessing particular $[Zn_4O(COO)_6]$ secondary building unit (SBU), to design porous structures in which pore size and functionality could be varied systematically [13a] (Fig. 3) by changing length and functional groups of the linkers.

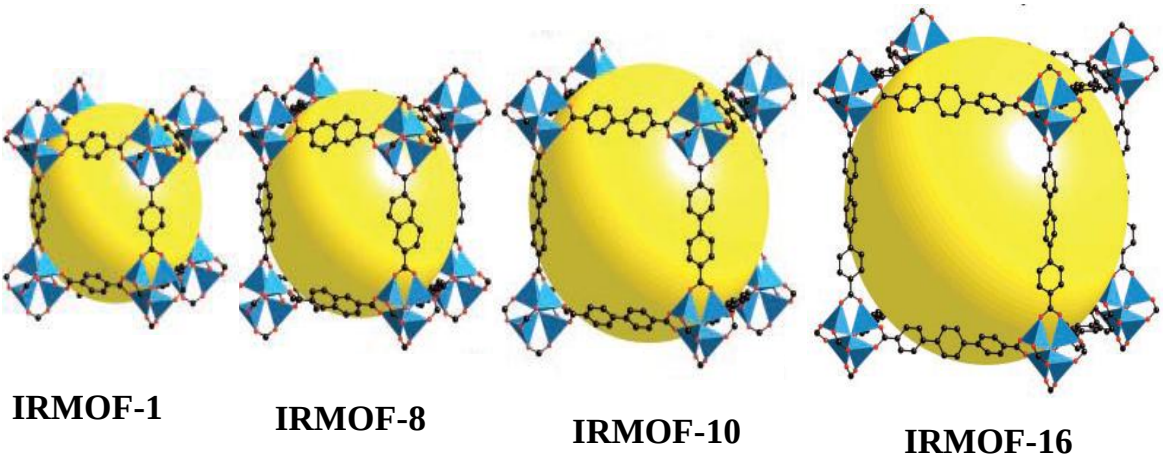

Fig. 3: Isoreticular MOFs (IRMOFs) constructed based on $[Zn_4O(COO)_6]$ SBU with different organic linkers. From reference 13a. Reproduced by permission of Science.

The FMOFs always undergo structural transformation upon guest removal and their behaviour towards incoming guest molecules is primarily dependent on several parameters, such as (a) chemical nature of the guest molecule; (b) extent of pore deformation and size of the pore window; (c) onset pressure; (d) temperature etc. Guest molecules with significant dipole/quadrupole moment could bring about enhanced interaction with the polar pore surfaces and ultimately diffuse into the channel at definite onset pressure, known as gate opening pressure. This is very important from the perspective of gas storage, separation and selectivity since only certain molecules would be able to interact whereas it rejects other molecules. Specific recognition characteristics of flexible compounds easily discriminate the incoming guest molecules in a particular way and the response can be recorded by various means, e.g., emission, adsorption studies with mixed-component systems etc. For example, Kitagawa *et al.*[13b] have reported gas detection in a FMOF. Here, a composite between a FMOF and fluorescent reporter distyrylbenzene (DSB) has been prepared and has found to selectively adsorbs

CO_2 over other atmospheric gases without any chemical interaction or energy transfer. The adsorption of CO_2 was accompanied by conformational variations of the included DSB followed by host structure transformation and resulted in a critical change in DSB fluorescence at a specific threshold pressure.

MOFs made up of 2D structure generally exhibit greater degree of flexibility compared to 3D framework because of the possible movement of the 2D networks during guest removal or accommodation (Figure 6). Maji *et al.* have previously demonstrated such kind of structural change, like irreversible sliding of 2D grids resulting into permanently porous structure [14a] (Fig. 4). Later, same group has further proved this sliding of net through guest selective single/double-step adsorption of vapour correlated to the successive confinement of adsorbates in a 1D channel and a 2D interlayer space [14b] (Fig. 5).

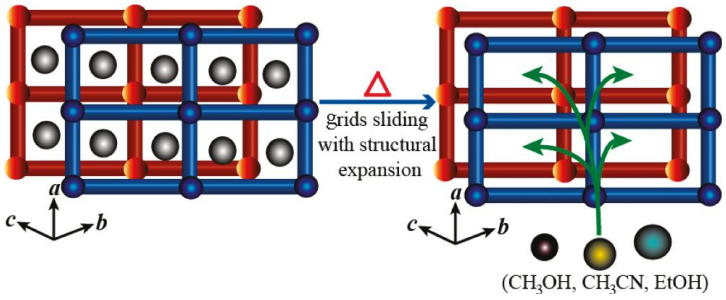

Fig. 4: Guest induced sliding of the 2D rectangular grids toward structural expansion. From reference 14a. Reproduced by permission of ACS.

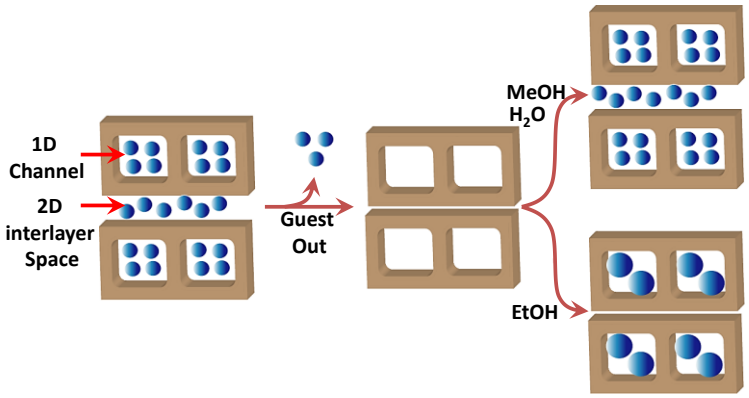

Fig. 5: Schematic of guest selective accommodation in the 1D channel and the 2D interlayer space.

1.5 Applications of MOFs

1.5.1 Gas Storage

The most intriguing characteristic of porous MOFs is their specific surface area. The highest surface area till reported in MOFs is from NU-110 (NU- North Western University) with an exceptional surface area of 7140 $m^2 g^{-1}$ [15].Other landmark examples in this respect are MOF-177 (16) (high surface area of 5640 $m^2 g^{-1}$), MIL-101[17] (surface area of 5900 $m^2 g^{-1}$), UMCM-2 [18] (with 6000 $m^2 g^{-1}$) and MOF-210 [19] with BET surface area of over 6240 $m^2 g^{-1}$. These significant high surface areas of porous MOFs definitely differentiate them for standing out from other porous materials.

The depletion of fossil fuel and climate change due to combustion of fossil fuel have prompted us to search for alternative clean energy source. Among various alternatives, hydrogen stands at the forefront due to its clean combustion and high gravimetric energy density. Safe and effective hydrogen storage is widely recognized as a critical enabling technology for a 'Hydrogen Economy' in the 21st century. Scientists are looking for novel materials which can hold sufficient hydrogen in terms of gravimetric and volumetric densities at ambient conditions. MOFs have also attracted worldwide attention in the area of hydrogen energy, particularly for hydrogen storage.[21-29] In 2003, Yaghi and co-workers first reported MOF-based hydrogen storage result.[30] Highest hydrogen storage at 1 bar and 77 K, has been reported by Zhou *et al.,* which is about 3.05 wt%.[31a] Hupp *et al.* reported highest hydrogen storage capacity of 9.05 wt% at 77 K and 56 bar [31b] based on a mesoporous MOF NU-110. Therefore by introducing the functional groups on the pore surface it is possible to modulate the pore volume and corresponding surface area. Thus, MOFs have proved themselves as one of the potential candidates to meet the target set by DOE for room temperature adsorption. Some of the MOFs exceed the required wt% set by DOE at respective low temperatures. Recent theoretical calculations suggest that materials with ΔH value of 22-25 kJ mol^{-1} will work fruitfully at room temperature and onset pressure of 30 bar.

Natural gas, is predominantly and significantly methane, has been considered to be a key transitional fuel among existing hydrocarbon-based fuels such as oil and coal, to renewable sources. It has heat of combustion of ΔH^{298}_{Comb} ~ 890 kJ mol^{-1}) [31c], and has higher hydrogen content than any other hydrocarbon fuel that means its carbon dioxide

emissions relative to the energy generated from its combustion are also favourable. The DOE has set the storage target by 2015 for CH_4 to be 180 v/v STP at 298 K and 35 bar [31d]. First reports of methane uptake by a MOF were published by Kitagawa and co-workers in 1997 for the compound $\{Co_2(4,4'\text{-}2,20\text{-bipyridine})_3(NO_3)_4]\cdot 4H_2O\}_n$ with an uptake of 77 v/v STP at 30 bar.[31d] Studies have flourished since which have led to frameworks being designed with this specific purpose of methane uptake. The current highest methane uptake MOF known is that reported by Zhou and co-workers, known as PCN-14.[31e] This MOF has a methane uptake of 230 v/v STP at 290 K and 35 bar, which is 28 % higher than the DOE target.

The high internal surface areas of metal-organic frameworks also provide an opportunity for large CO_2 storage capacities to be achieved. For example, at 35 bar, the volumetric CO_2 adsorption capacity for MOF-177 (Langmuir surface area of 5640 $m^2\ g^{-1}$) reaches a storage density of 320 cm^3 (STP)/cm^3 and it is approximately 9 times higher than the quantity stored at this pressure in a container without the metal-organic framework and is higher than conventional materials, namely, zeolite 13X and MAXSORB.[20] But at low pressure (1 atm) Mg-MOF-74 shows highest storage capacity of 27.5 wt% at 298 K.

1.5.2 Selective Adsorption and Separation

Adsorptive separation is very important in industry. Generally, the process uses porous solid materials such as zeolites, activated carbons, or silica gels as adsorbents. With an ever increasing need for a more efficient, energy-saving and environmentally benign procedure for gas separation, adsorbents with tailored structures and tunable surface properties must be found. MOFs are promising candidates as adsorbents for gas separations due to their large surface areas, adjustable pore sizes and controllable properties as well as acceptable thermal stability. In adsorptive separation processes, gas separation is achieved based on the differences of adsorption capability of different components in the adsorbent. The performance of any such process is directly determined by the characteristics of the adsorbent in both adsorption equilibrium and kinetics. In addition to acceptable mechanical properties, a promising adsorbent should possess not only good adsorption capacity and selectivity, but also favourable adsorption kinetics and regenerability. And all these criteria are mainly governed by one particular parameter, the

interactions of gas molecules to the polar pore surface of the material. Gas separation techniques include cryogenic distillation, membrane-based, and adsorption-based technologies.[32,34]

For real time applications, *e.g.* separation of hazardous CO_2 from flue gases and gas mixtures, it is important to design MOFs that can capture CO_2 efficiently at low pressure and high temperature. Maji *et al.* showed an unusual CO_2 adsorption behaviour in a fluoro-functionalized MOF $\{[Zn(SiF_6)(pyz)_2]\cdot 2MeOH\}_n$ (pyz = pyrazine) with a 1D channel system [35a]. Surprisingly, it adsorbs higher amounts of CO_2 at 298 K than at 195 K, which is in contrast to the usual trend and would have potential importance for separation purposes.

For example, Mg-MOF-74 has been found to selectively adsorb CO_2 over CH_4 through breakthrough experiment.[35b] Zaworotko *et al.* have further shown an unprecedented CO_2 sorption selectivity over N_2, H_2 and CH_4, even in the presence of moisture. Here, they have reported a series of SiF_6^- anion based MOFs and have been subjected to CO_2 separation in the context of post-combustion (flue gas, CO_2/N_2), pre-combustion (shifted synthesis gas stream, CO_2/H_2) and natural gas upgrading (natural gas clean-up, CO_2/CH_4) through combining equilibrium and kinetic adsorption selectivity.[35c] Frameworks $Mg_3(ndc)_3$, (ndc = naphthalenedicarboxylic acid) [35d] PCN-13, [36] etc. have been found to selectively adsorb H_2 over N_2 at 77 K. A unique selective adsorption of C_2H_2 over CO_2 was achieved by $[Cu_2(pzdc)_2(pyz)]_n$ (pzdc = pyrazinedicarboxylic acid; pyz = pyrazine).[37] Yaghi *et al.* have reported a square-grid-based 3D framework, $[Zn_2(bdc)_2(bpy)]_n$ (MOF-508) (bdc = 1,4-benzenedicarboxylic acid, bpy = 4,4′-bipyridyl) that can separate linear and branched isomers of pentane and hexane molecules.[38] When the crystalline powder was placed in a gas chromatographic (GC) column, it was found, for example, that 2-methylpentane runs through the column faster than its linear isomer *n*-hexane, and the other isomer, 2,2-dimethylbutane, elutes even faster. The separation capability of GC is a result of its differential interaction with the alkane isomers.

1.5.3 Catalysis

The ability to incorporate functional groups into porous MOFs makes them excellent candidates as heterogeneous catalysts. The well-defined pores and channels in MOFs have the potential for the size- and shape-selective catalysis that is the landmark

of zeolites. The diversity of zeolites, however, is rather limited due to the use of exclusively SiO_4/AlO_4 tetrahedral building units. The resulting 3D frameworks of zeolites are microporous with channels/cavities of up to 1.3 nm, and as a result, the catalytic applications of zeolites are restricted to relatively small organic molecules (typically no larger than xylenes). But MOF has the potential to offer unique structural and chemical features that can be beneficial for an industrial application such as the lack of non-accessible bulk volume, very open architecture, and the self-diffusion coefficients of molecules in the pore system are only slightly lower than in the bulk solvent.[39] This means that mass transport in the pore system is not hindered. In this scheme (Fig. 6,7) it can be seen that the metal-connecting points in MOFs typically have coordinated water or other solvent molecules that can be readily removed without distorting the framework structures. Such accessible, coordinatively unsaturated metal centres can be used to catalyse organic reactions. In the second approach, catalytic sites are incorporated directly into the bridging ligands used to construct MOFs. Although more synthetically demanding, the second approach is much more versatile and allows for the incorporation of a wide variety of catalysts. In this regard Kitagawa *et al.* have reported Knoevenagel condensation reaction, which is a well-known base catalyzed model reaction, with $\{[Cd(4\text{-btapa})_2(NO_3)_2]\cdot 6H_2O\cdot 2DMF\}_n$ (4-btapa = 1,3,5-benzenetricarboxylic acid

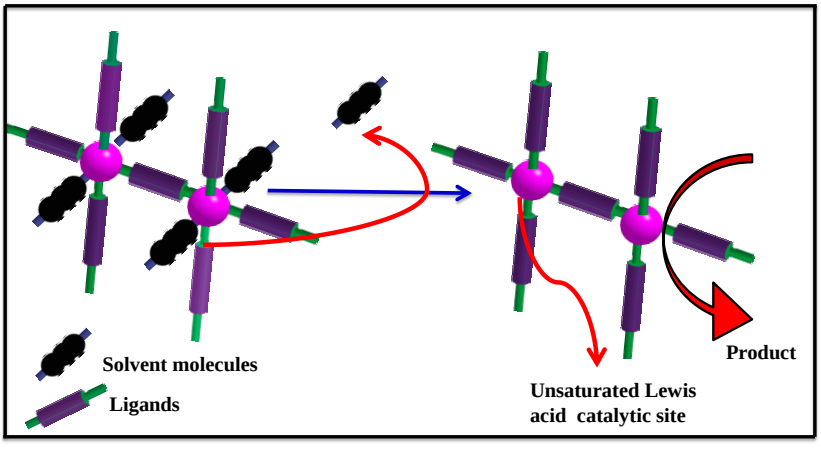

Fig. 6: Schematic illustrating the generation of unsaturated Lewis acidic metal sites (spheres) as active catalytic sites.

tris[N-(4-pyridyl)amide]).[40a] The activated compound selectively accommodated guests

(substrates) in its channels because of the active amide groups. As a result, the reaction proceeded with good selectivity with benzaldehyde.

Kaskel *et al.* have chosen HKUST-1 or as MOF-199 as a catalyst because of its large pore window size and unsaturated active Lewis acid site Cu^{II}. Upon removal of

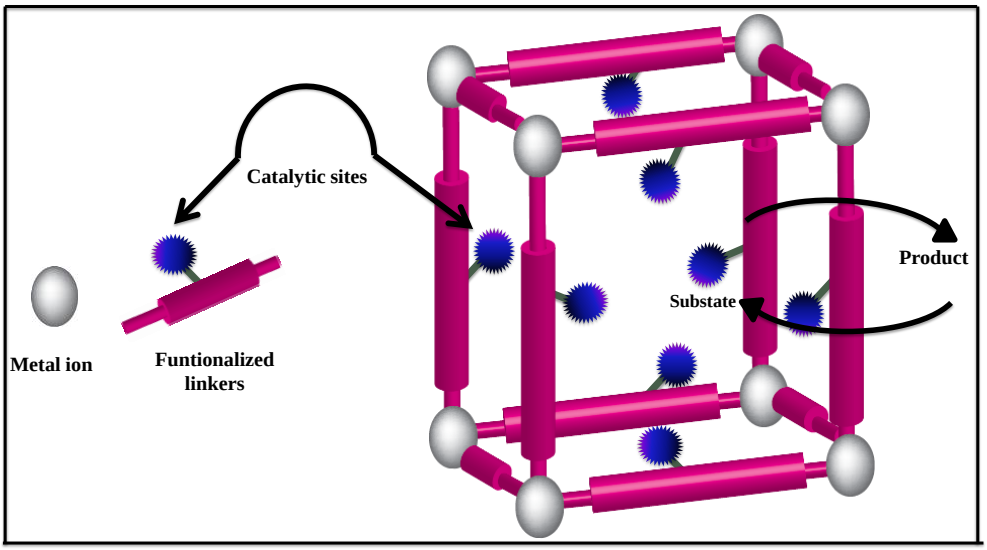

Fig. 7. Schematic showing the use of functional groups as active catalytic sites.

coordinated solvent molecules, the lewis acid site Cu^{II} becomes open and could be used for cyanosilylation of benzaldehyde or acetone.[40b] Same group has further found MIL-101 to be better catalyst than HKUST-1 for the same cyanosilylation purpose due to presence of more active site Cr^{III} and also the side product formation, phenol, could have been controlled .(40c)

1.5.4 Luminescence and Sensing

MOFs provide a potential platform for the field of solid state luminescent materials as a large number of lumophores can be incorporated into the framework and the resulting emissions can be tuned in a predictable manner.[41] The hybrid nature of MOF materials consisting of both an organic linker and metal ion, enables a wide range of emissions, like linker based emissions, ligand-to-metal charge transfer (LMCT) or metal–to-ligand charge transfer (MLCT), excimer and exciplex emission, metal based emission and finally adsorbate based emission and sensitization (Fig. 8). Zaworotko *et al.*

reported the first example of exciplex formation in MOFs, $\{[Zn(bpy)_{1.5}(NO_3)_2]\cdot Pyrene\}_n$; (bpy = 2,2′- bipyridine) where pyrene, an electron rich core acts as a donor and metal coordinated 2,2′- bpy acts as an acceptor.[42,43] A close look in such systems shows face-to-face or face-to-edge stacking of donor and acceptor which is responsible for the red shifted exciplex in the system. Kitagawa *et al.* reported an bpNDI core containing porous MOF, $\{[Zn_2(bdc)_2(bpNDI)]\cdot 4DMF\}_n$ (bdc = 1,4-benzenedicarboxylic acid and bpNDI = *N*,*N*′-di(4-pyridyl)-1,4,5,8-naphthalenediimide)) and based on the inclusion of different aromatic guest molecules they observed a competitive interaction between exciplex emission and charge transfer[44] which results in a guest dependent tunable emissions in the whole visible region of the spectrum. Apart from these excited state processes, emissions based on MLCT and LMCT are also well known in framework materials. The most commonly reported structures are for Cd^{II} and Zn^{II}, which have filled *d*-orbitals and thus no *d*–*d* transitions are possible.[41] In such frameworks with π-conjugated linker

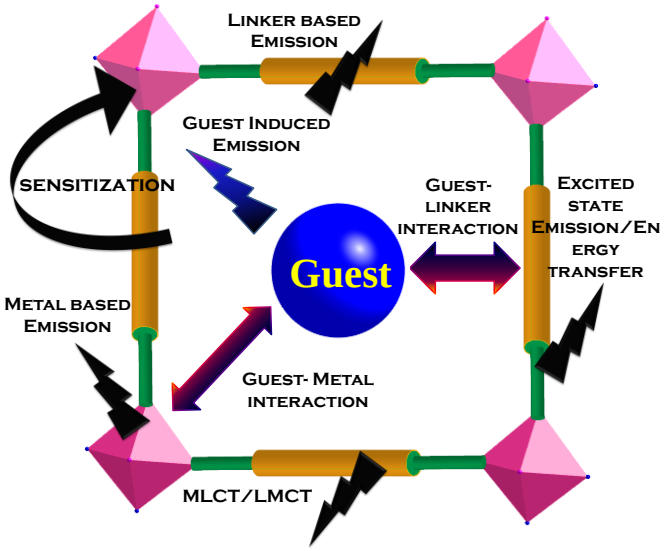

Fig. 8: Emission possibilities in a porous MOF.

LMCT/MLCT based emission is observed.

For many years, a popular strategy for highly luminescent framework has been to introduce lanthanide (Ln) ions into the supramolecular system as scaffold. Eu^{III} and Tb^{III} are attractive luminophores for such purposes because of their confined (narrow) emission in the visible regions. However, Ln electronic transitions are forbidden by

Laporte selection rules, and gives rise to weak absorbance and low quantum yields. A common way to overcome this problem is through coordination of the lanthanide ion with a strongly absorbing organic strut. A direct energy transfer occurs from the more readily accessible linker excited state to the appropriate metal energy level. This coupling leads to a significant increase in luminescence intensity as well as quantum yield and is commonly known as the ‘‘antenna’’ effect. The primary application for these kinds of frameworks is sensing.(45) Jing Li *et al.* have shown a Tb^{III} based framework and utilized for anion sensing.(46a) Maji *et al.* have shown that it is possible to tune emission colours ranging from green to red under same excitation wavelength through doping in a pure Tb^{III} based MOF $\{[Tb_2(Mu^{2-})_3(H_2O)_2]\cdot 4H_2O\}_n$ with different percentage of Eu^{III} $\{[Tb_{2-2x}Eu_{2x}(Mu^{2-})_3(H_2O)_2]\cdot 4H_2O\}_n$ (Fig. 9).(46b)

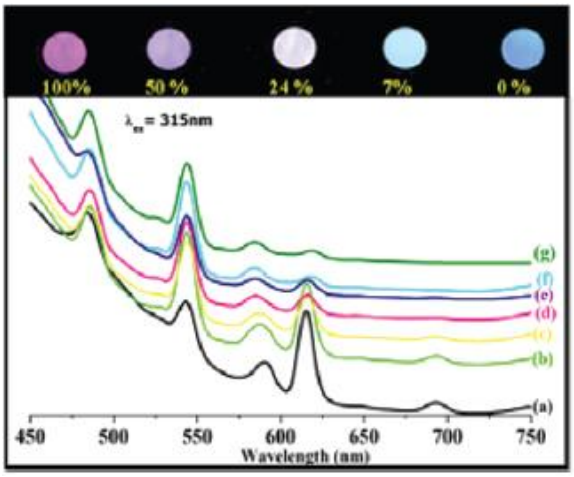

Fig. 9: (Top) Color of different samples of different Eu^{III} contents under UV light. (Bottom) Emission spectra of mixed Tb^{III}–Eu^{III} compounds with different percentages of Eu doping (λex = 315 nm): (a) 50%; (b) 24%; (c) 15%; (d) 7%; (e) 4%; (f) 1.24%; (g) 0.6%. From reference 46b. Reproduced by permission of ACS.

Hupp *et al.* recently reported a light harvesting framework Zn_2(Zn-L2)(L3) [where L2 = tetraacid porphyrin; L2 = boron dipyrromethene (bodipy)] based on porphyrine core based framework which shows an efficient strut-to-strut energy transfer between donor and acceptor.(47)

1.5.5 Magnetism

Metal-organic approach could also combine magnetically active metal ions with

organic linkers as a polytopic ligand and in some cases may also be a spin-bearing unit and provide ferro-, antiferro- or ferromagnetic systems.[48,49] This strategy results to magnetic materials with higher T_c (critical temperatures) than purely organic magnets. Two main families can be distinguished. On one side are the magnets are formed by magnetically active metal ions and organic moieties with a closed-shell electronic structure. In this case, the magnetic behaviour originates from the metal ion and the organic ligand has only a structural function promoting the magnetic interaction.[50]

Magnetism in MOFs has become more effective when porosity and magnetism are combined together in the same material. First, versatile molecular chemistry provides a large number of ligands whose shape and topology can be controlled. Second, these ligands have been proven to service as good superexchange pathways. Kurmoo *et al.* have reported a reversible crystal-to-crystal transformation accompanied by change from ferromagnetic to antiferromagnetic ground states at 8 K upon dehydration-rehydration in a nanoporous MOF $\{[Co^{II}_3(OH)_2(C_4O_4)_2]\cdot 3H_2O\}_n$ (C_4O_4 = squaric acid).[51a] Porous and magnetic solids constructed around carboxylate-based ligands (O–C–O), allow the formation of 1D, 2D or 3D frameworks with M–O–C–O–M and/or M–O–M connectivities with magnetically active metal ions. In these systems, organic molecules are either small or extended polytopic ligands, but the magnetic properties are governed by the M–O–C–O–M or M–O–M structural motifs, which lead to strong interactions compared to the magnetic pathways defined by bridged metal ions through multitopic ligands without such connectivities.[51b]

Maji *et al.* have beautifully shown that through fixation of atmospheric CO_2, $Cu(CO_3)$ based kagomé layers have been formed which on pillaring through linkers gave pillared layer structure. It exhibited weak antiferromagnetic interaction in the kagomé layer and interlayer ferromagnetic coupling at low temperature.[51c]

1.6 Nanoscale Metal–Organic Materials

The physical and chemical properties of a material are governed by the types of allowed electronic motion to execute and it is determined by the atomic space in which the moving electrons have been confined. Unbound (unconfined) electronic motion is not quantized and can thus absorb any amount of energy given to them and it is utilised simply to move more rapidly. Once bound in an atom, a molecule or a material, their

motion becomes highly confined and quantization sets in. The allowed types of motion in atomic or molecular orbitals are of well-defined energies that are completely separated from one another. The smaller the space for the bound motion, the stronger the confinement, the larger is the energy separation between the allowed energies of the different types of motion. The nuclear confinement is the strongest type of confinement of the motion for subatomic particles. The motion of the nucleons is thus strongly confined to the femtometer scale within the atomic nucleus. This results further electronic confinement in atoms. For example, In the hydrogen atom, the electron is confined to a length scale of ~ 50 pm.

This thus decreases the space in which the charge carriers (the excitons) confine their motion. If we consider, the motion of an electron (particle) in a box, with decrease in the size of the box, the kinetic energy, as well as its excitation energy, increases. Similarly, when the sizes of the particles become smaller than their Bohr radius, their band gap energy increase. Thus, the optical and other physical and chemical (e.g., oxidation-reduction) properties of semiconductor nanoparticles become highly sensitive to the size and shape of the particles.

Although a reasonable number of nanomaterials have been brought into this field as nanocarriers for different purposes such as imaging and therapeutic agents etc.[52a] but the majority of them are categorized into either purely inorganic materials (such as quantum dots, Fe_3O_4, and Au nanoparticles) or purely organic (such as liposomes, dendrimers, polymers). But each of these classes of nanomaterials has its disadvantages' too. Here, the hybrid material, MOFs comes into picture. It has been possible to fabricate bulk MOF into NMOF through several adopted techniques. NMOFs possess some potential advantages over existing nanocarriers. First, MOFs are compositionally and structurally diverse, allowing for the facile synthesis of NMOFs of different compositions, shapes, sizes, and chemical properties. Second, NMOFs are intrinsically biodegradable as a result of relatively labile metal-ligand bonds, making it possible to rapidly degrade and clear the nanocarriers after the intended task is completed.

Fabrication to the nanoscale is a very fruitful strategy for the development of new materials with novel and often better properties compared to traditional bulk materials. It has opened up a huge potential for better technological and biomedical applications in future, including drug-delivery, catalysis, diagnostics, solar cells, etc. However, metal–

organic materials in the form of traditional bulk crystalline materials do not always fulfil all specific needs for these applications. When the MOF crystals are fabricated to nanometer scale, the contribution from the crystal interface must need to be considered; the ratio of surface area over volume (S/V) is no longer negligible resulting in a smaller diffusion length. Hence, the crystal interface is expected to influence the sorption kinetics or even the sorption type, especially in liquid phase application. Indeed, emerging fields such as porous membranes,[52b] thin film devices,[53] or carrier particles for drug delivery [54] are highlighting that fabrication and controlling the crystal size and shape (morphology) of these porous coordination frameworks are key features to strengthen their contribution to the development of nanotechnology.[55] For example, nanomaterials are typically essential to provide sufficient small sizes for their internalization into cells, and this limits the applications of bulk MOF as delivery vehicles, diagnostics, etc. But nanoscale MOFs combine this small dimension with well-defined and uniform sizes and morphologies. Hence, it is easily dispersible in aqueous media or other solvents efficiently can be coated for improvement in biocompatibility or other recognition capabilities and these NMOFs are also expected to hold highly desirable size-dependent optical, electrical and magnetic properties.

1.7 Synthetic Procedures

There are several major strategies for synthesizing nanoscale metal–organic materials (Fig. 10): (i) confined growth of the supramolecular assembly at nano dimensions by using emulsions or templates; (ii) coordination modulation method (iii) the controlled precipitation of self-assembled metal–organic polymers by the use of poor solvents, (iv) microwave radiation (v) ultrasounds and (vi) solvo/hydrothermal method.[56]

Nanoemulsion is a suspension of small droplets, usually stabilized by a surfactant (a water-in-oil or reverse microemulsion), with diameters ranging from 50 to 1000 nm. Because of these nanodimensions of the micelle cores, these can be used as ‘‘nanoreactors’’ to confine the self-assembly, nucleation and growth of metal–organic nanostructures.(Fig. 10).

In coordination modulation method, the addition of modulator with the same functionality as of organic linkers impedes the coordination interaction with metal ions and organic linkers and perturbs the rate of growth of crystals which results into

nanoscale. In presence of any kind of external stimuli such as temperature, light or microwave radiation, it is possible induce polymerisation in a controlled manner.

In some cases, direct precipitation has been obtained through direct exposure to external stimuli, such as ultrasound, microwave, temperature and direct addition of poor solvents.

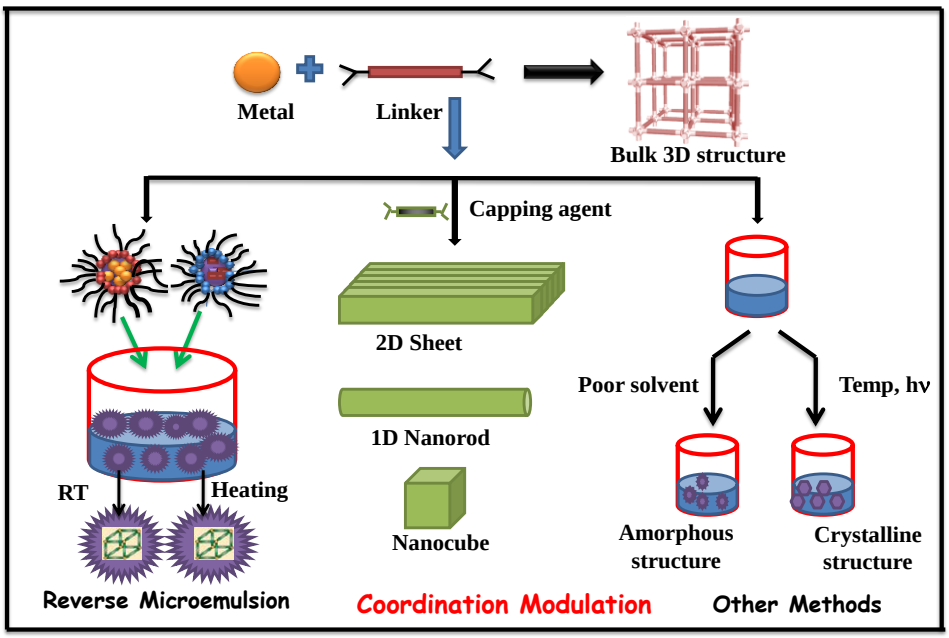

Fig. 10: Different synthetic strategies for fabrication of bulk MOF to NMOF.

1.8 Applications in Nanoscale

1.8.1 Gas Sorption Properties

Because of the quite satisfactory properties exhibited by bulk MOFs, their nanoscopic counterparts are expected to exhibit interesting, novel and even improved gas sorption properties. Groll *et al*. have adopted a new technique for the rapid preparation of a flexible porous coordination polymer nanocrystals of $[Zn(ip)(bpy)]_n$ (ip = isophthalic acid, bpy = 4,4′-bipyridyl) that combines non-aqueous inverse microemulsion with ultrasonication. Adsorption experiments with methanol showed that the overall adsorption capacities of nanoparticles and bulk are almost identical, but the shapes of the sorption isotherms differ significantly and the adsorption kinetics increase dramatically.[63] Kitagawa *et al.* showed that fabrication from bulk to nanorods through coordination modulation method has shown with significant improvement over the surface area as well

as CO_2 storage capacity.[64a] Oh *et al.* successfully synthesized NMOFs based on In^{III} metal ions and BDC ligands that showed a H_2 and CO_2 uptake of 140 $cm^3 g^{-1}$ (77 K) and 333 $cm^3 g^{-1}$ (195 K) respectively.[64b] Exarhos *et al.* have recently described a reversible uptake and release of CO_2 in an imidazolate NMOF with 35 % of weight capacity at 30 bar.[64c]

1.8.2 Drug Delivery Systems

The development of drug delivery in nanoscale metal–organic systems has been obtained by incorporating those drugs using different strategies: (i) drug molecules as one of the building blocks of the metal–organic structure; (ii) encapsulation of drugs inside a metal–organic matrix; and (iii) drugs are adsorbed in porous NMOFs. Lin *et al.* have used the precipitation approach by addition of poor solvent for synthesising nanospheres from the coordination of a Pt^{IV} based anticancer drug and Tb^{III} metal ions.[57] The same authors also applied the post synthetic covalent attachment of drug molecules in porous NMOFs

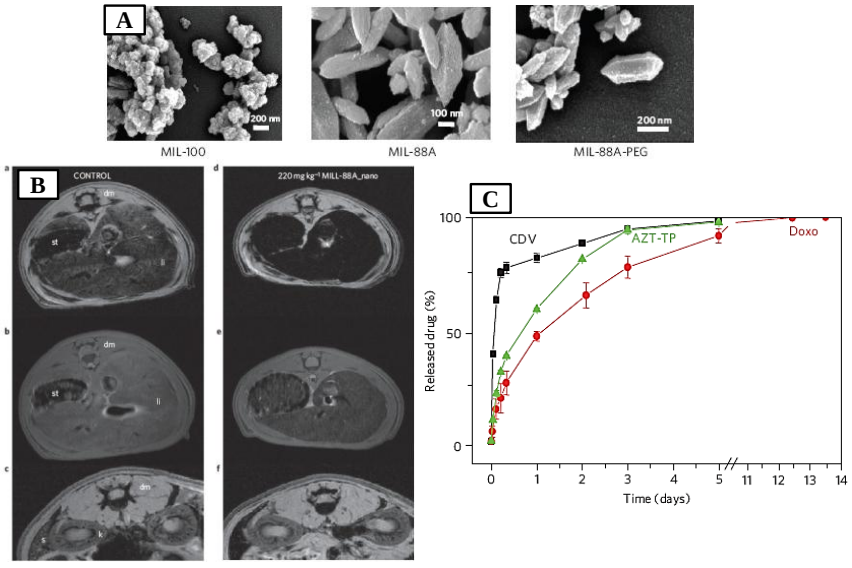

Fig. 11: A. Scanning electron micrographs of MIL-100 (left), MIL-88A (centre) and PEGylated MIL-88A nanoparticles (right) B. CDV (black), doxo (red) and AZT-TP (green) delivery under simulated physiological conditions (PBS, 37 °C) from MIL-100 nanoparticles C. Magnetic resonance images. The images were acquired with gradient echo (a, c, d, f) or spin echo (b, e) sequence of control rats (left; a–c) and rats injected with 220 mg kg^{-1} MIL-88A (right; d–f), in liver (a, b, d, e) and spleen (c, f) regions. 30 min after injection, product effect is observable on the liver and spleen. (dm, dorsal muscle; k. kidney; li, liver; s, spleen; st, stomach.). From reference 59. Reproduced by permission of Nature.

built up from Fe^{III} metal ions and 2-aminoterephthalic acid.[58] The pendent amino groups on the porous NMOFs has been utilised to covalently interact with an ethoxysuccinato-cisplatin pro-drug activated with 1,1-carbonyldiimidazole. Horcajada, Gref *et al.* have recently synthesized porous non-toxic NMOFs [59] composed of Fe^{III} metal ions and different dicarboxylate ligands (e.g. BDC or BTC) to load a wide variety of antitumoral drugs, such as DOX, busulfan, cidofovir and azidothymidine triphosphate. The loading was achieved by soaking these porous NMOFs in saturated drug solutions. Interestingly, in all these cases, the successful design of the drug delivery system was confirmed by proving the controlled and progressive release of the encapsulated drug as well as their in *vitro* anticancer efficacies; thus opening the way to start considering the use of metal–organic nanostructures as novel drug delivery systems (Fig. 11).

1.8.3 Contrast Agents

Nano MOFs are excellent potential candidates to act as contrast agents because it can be constructed from highly paramagnetic metals ions, such as Gd^{III} and Mn^{II}, and, since, being in small size, it allows different biodistribution and opportunities beyond the

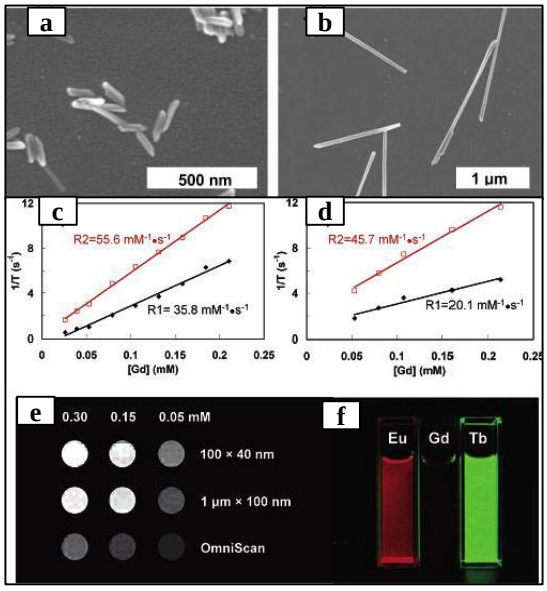

Fig. 12: (a,b) SEM images of $Gd(BDC)_{1.5}(H_2O)_2$ nanorods (**1**) (c) *R*1 and *R*2 relaxivity curves of **1** of ~100 nm in length by 40 nm in diameter (d) *R*1 and *R*2 relaxivity curves of **1** of 1 µm in length by ~100 nm in diameter (e) *R*1 and *R*2 relaxivity curves of **1** of ~1 µm in length by ~100 nm in diameter (d) Luminescence images of ethanolic suspensions of **1**, **1a** (**1** doped with 5 mol %

of Eu^{III}), and **1b** (**1** doped with 5 mol % of Tb^{III}). From reference 60. Reproduced by permission of ACS

conventional imaging of chemical agents. Lin *et al.* have shown the efficiency of NMOFs to modify the relaxation times of the water protons in the surrounding medium when a magnetic field is applied. For example, Gd^{III} based nanorods have shown exceptionally high longitudinal *R*1 and transverse *R*2 relaxivities of 35.8 s^{-1} and 55.6 s^{-1} per mM of Gd^{III} (Fig. 9),[60] whereas nanoparticles built up from Gd^{III} metal ions connected through benzenehexacarboxylate ligands have an impressive *R*2 relaxivity of 122.6 s^{-1} per mM of Gd^{III}.[61]

1.8.4 Cell Imaging

Optical imaging is widely used in biological studies. Visible light is used to excite dye molecules within a tissue, which fluoresce at longer wavelengths. This technique is ubiquitous for in *vitro* and ex *vivo* studies but is limited by poor tissue penetration in *vivo* applications. A number of NMOFs have been synthesized which are inherently luminescent, but have not been evaluated as biomedical imaging agents. [28, 29, 39] NMOFs are not ideal for biomedical imaging applications due to its non-optimal absorption properties and low quantum yields. Lin and co-workers synthesized NMOFs containing a phosphorescent $Ru(bpy)_3^{II}$ derivative as the bridging ligand and Zn^{II} [14] or Zr^{IV} [15] metal connecting points [64] . It has been further coated with a layer of amorphous silica, functionalized with PEG, and targeted to cancer cells. Confocal microscopy studies using human lung cancer cells demonstrated increased uptake of the targeted nanoparticles, which was confirmed by ICP-MS analysis.

1.8.5 Catalytic Properties

Fabrication of catalytically active metals into nanoparticles is a promising route towards a more efficient heterogeneous catalysis due to the possibility of higher surface area as well as increase in the concentration of active sites. Sweigart *et al.* used the precipitation approach to assemble Rh based metal–organic catalysts and Al^{III} metal ions into nanospheres.[62]This has enhanced the stereoselective polymerization of phenylacetylene and the catalytic activity of these metal–organic nanocatalysts is

dependent on the size of the particles. As expected, smaller nanospheres were more active than the bigger ones.

1.8.6 Optical Properties

Luminescent coordination nanoparticles of 5 nm in diameter were prepared by Mallah et al. by controlling the growth of the already known coordination polymer based on Tb^{III} or Eu^{III} metal ions and BDC ligands with poly(vinyl pyrrolidone).[65a] The water dispersion of Tb^{III} and Eu^{III} are found to be stable for several weeks. Emission spectra of the nanoparticles have been recorded every hour for 20 h without any change, which shows good consistency towards stability of the nanoparticles in solution. The size of these particles did not exceed 10 nm together and their good water dispersibility makes them interesting for biological applications. Xu *et al.* have synthesized Tb^{III} and 4,4′,4′′-benzene-1,3,5-triyl-tri-benzonate based (BTB) infinite coordination polymer (ICP) hollow microspheres. It has been possible to tune the luminescent characteristics of the Tb-BTB hollow spheres within a wide spectral range by simply varying the excitation lines or the doping concentration of Eu^{III} in order to get white light emission.[65b]

1.9 Multifunctional Hybrid Materials

Now the recent trend is functionalized nanoparticles with various molecular and biomolecular units in order to assemble into complex hybrid systems. A variety of such composites have been prepared and have been utilized for several purposes such as specific sensing of substrates,[66a] tunable electroluminescence,[66b] and enhanced photoelectrochemistry[67] fabricated nanoscale devices such as single-electron transistors,(68) NP based molecular switches,[69] and metal–insulator–nanoparticle–insulator–metal (MINIM) capacitors.[70]

The convergence of biotechnology and nanotechnology has led to the development of hybrid nanomaterials that incorporate the highly selective catalytic and recognition properties of biomaterials, such as proteins/enzymes and DNA, with the unique electronic, photonic, and catalytic features of nanoparticles. The importance of functionalized nanoparticles for biomedical applications cannot be overestimated. For instance, targeted entry into cells is an increasingly important area of research.[71] The nucleus is a desirable target because the genetic information of the cell and transcription

machinery resides there. Targeted nuclear delivery is a challenging task because a nuclear probe must, at least, satisfy the following requirements: 1) it should enter the cell (e.g. through receptor-mediated endocytosis), 2) it should escape endosomal/ lysosomal pathways, 3) it should possess a nucleus localization signal to interact with the nuclear-core complex, and 4) the probe should be small enough (<30 nm) to cross the nuclear membrane. The most-efficient nuclear targets in biology are viruses, which commonly utilize different peptides for crossing each cell-membrane barrier. Artificial systems that model viral behaviour could be designed on derivatives of functionalized nanoparticles. In a biologically inspired model system, Au NPs (20 nm) were modified with shells of bovine serum albumin (BSA) which were conjugated to various cellular targeting peptides to provide functional nanoparticles that penetrate the biological membrane and target the nuclei.[71b] Various NPs are applied as targeted biomarkers and drug-delivery agents to tumours in the analysis and medical treatment of cancers.[72] Hybrids of silver NPs with amphiphilic hyperbranched macromolecules exhibit antimicrobial properties and are used as drugs.[73]

It has been always welcome for bio-friendly nanoparticle which is biologically compatible and shows minimum toxicity for human cells rather than toxic metal nanoparticles. It is worthy to give effort to synthesize those hybrid nanomaterials and testing for in *vivo* and in *vitro* study. Maji *et al.* have prepared multi-functional carbon nanospheres with magnetic Prussian blue nanoparticles and luminescent lanthanide ions.[74] The negatively charged surface of the glucose derived carbon sphere facilitates the nucleation of Prussian blue nanoparticles on its surface. The luminescent lanthanide probes were attached to the surface of the carbon sphere through a benzene tricarboxylic acid linker. These multifunctional hybrid organic–inorganic composites are superparamagnetic and show enhanced luminescent properties. Their ability to cross the blood–brain barrier (enter the brain cell nucleus with no animal toxicity) in a mouse model indicate that these nanocomposites are promising theranostic agents for the treatment of brain diseases.

In the foregoing discussions, several aspects of MOFs will be highlighted from two different perspectives; bulk and nanoscale.

2.1 References

1. M. O'Keeffe, M. A. Peskov, S. J. Ramsden and O. M. Yaghi, *Acc. Chem. Res.*, 2008, **41**, 1782.

2. G. Férey, *Chem. Soc. Rev.*, 2009, **37**, 191.

3. S. Horike, S. Shimomura and S. Kitagawa, *Nat. Chem.*, 2010, **1**, 695.

4. D. J. Tranchemontagne, J. L. Mendoza-Cortes, M. O'Keeffe and O. M. Yaghi, *Chem. Soc. Rev.*, 2009, **38**, 1257.

5. M. Eddaoudi, D. B. Moler, H. Li, B. Chen, T. M. Reineke, M. O'Keeffe and O. M. Yaghi, *Acc. Chem. Res.*, 2001, **34**, 319.

6. U. Mueller, M. Schubert, F. Teich, H. Puetter, K. Schierle-Arndt and J. Pastre, *J. Mater. Chem.*, 2006, **16**, 626.

7. Y. Huang, B. Ding, H. Song, B. Zhao, P. Ren, P. Cheng, H. Wang, D. Liao and S. Yan, *Chem. Commun.*, 2006, 4906.

8. M. Kurmoo, *Chem. Soc. Rev.*, 2009, **38**, 1353.

9. S. Bordiga, C. Lamberti, G. Ricchiardi, L. Regli, F. Bonino, A. Damin, K. Lillerud, M. Bjorgenn and A. Zecchina, *Chem. Commun.*, 2004, 2300.

10. G. J. Halder, C. J. Kepert, B. Moubaraki, K. S. Murray and J. D. Cashion, *Science*, 2002, **298**, 1762.

11. S. T. Meek, J. A. Greathouse and M. D. Allendorf, *Adv. Mater.*, 2011, **23**, 249.

12. (*a*) S. Kitagawa and M. Kondo, *Bull. Chem. Soc. Jpn.*, 1998, **71**, 1739; (*b*) S. Horike, S. Shimomura and S. Kitagawa, *Nat. Chem.*, 2009, **1**, 695.

13. (*a*) M. Eddaoudi, J. Kim, N. Rosi, D. Vodak, J. Wachter, M. O'Keeffe and O. M. Yaghi, *Science*, 2002, **295,** 469; (*b*) N. Yanai, K. Kitayama, Y. Hijikata, H. Sato, R. Matsuda, Y. Kubota, M. Takata, M. Mizuno, T. Uemura and S. Kitagawa, *Nat. Mater.*, 2011, **10**, 787.

14. (*a*) K. L. Gurunatha and T. K. Maji, *Inorg. Chem,*. 2009, **48**, 10886; (*b*) P. Kanoo, G. Mostafa, R. Matsuda, S. Kitagawa and T. K. Maji, *Chem. Commun.*, 2011, **47**, 8106.

15. O. K. Farha, I. Eryazici, N. C. Jeong, B. G. Hauser, C. E. Wilmer, A. A. Sarjeant, Q. Snurr, S. T. Nguyen, A. Ö. Yazaydın and J. T. Hupp, *J. Am. Chem. Soc*. 2012, **134**, 15016

16. H. K. Chae, D. Y. Siberio-Perez, J. Kim, Y. Go, M. Eddaoudi, A. J. Matzger, M. O'Keeffe and O. M. Yaghi, *Nature* 2004, **427**, 523.

17. G. Férey, C. Mellot-Draznieks, C. Serre, F. Millange, J. Dutour, S. Surble and I. Margiolaki, *Science*, 2005, **309**, 2040.

18. K. Koh, A. G. Wong-Foy and A. J. Matzger, *J. Am. Chem. Soc.*, 2009, **131**, 4184.

19. H. Furukawa, N. Ko, Y. B. Go, N. Aratani, S. B. Choi, E. Choi, A. O. Yazaydin, R. Q. Snurr, M. O'Keeffe, J. Kim and O. M. Yaghi, *Science*, 2010, **329**, 424.

20. A. R. Millward, O. M Yaghi, *J. Am. Chem. Soc*. 2005, **127**, 17998.

21. D. Zhao, D. Q. Yuan and H. C. Zhou, *Energy Environ. Sci.*, 2008, **1**, 222.

22. M. Dincă and J. R. Long, *Angew. Chem. Int. Ed.*, 2008, **47**, 6766.

23. M. Hirscher, B. Panella and B. Schmitz, *Microporous Mesoporous Mater*. 2010, **129**, 335.

24. Y. H. Hu and L. Zhang, *Adv. Mater.*, 2010, **22**, E117.

25. S. V. Kolotilov and V. V. Pavlishchuk, *Theor. Exp. Chem.*, 2009, **45**, 277.

26. S. V. Kolotilov and V. V. Pavlishchuk, *Theor. Exp. Chem.*, 2009, **45**, 75.

27. L. J. Murray, M. Dincă and J. R. Long, *Chem. Soc. Rev.*, 2009, **38**, 1294.

28. K. M. Thomas, *Dalton Trans.*, 2009, 1487.

29. B. Xiao and Q. C. Yuan, *Particuology*, 2009, **7**, 129.

30. N. L. Rosi, J. Eckert, M. Eddaoudi, D. T. Vodak, J. Kim, M. O'Keeffe and O. M. Yaghi, *Science*, 2000, **300**, 1127.

31. (*a*) X.-S.Wang, S. Ma, P. M. Forster, D. Yuan, J. Eckert, J. J. López, B. J. Murphy, J. B. Parise, and H.-C. Zhou, *Angew. Chem. Int. Ed*. 2008, **47**, 7263; (*b*) O. K. Farha, A. Ö. Yaza -ydın, I. Eryazici, C. D. Malliakas, B. G. Hauser, M. G. Kanatzidis, S. T. Nguyen, R. Q. Snurr and J. T. Hupp, *Nat. Chem*., 2010, **2**, 944 (*c*) T. Burchell and M. Rodgers, *SAE Tech. Pap. Ser*., 2000, 2201; (*d*) M. Kondo, T. Yoshitomi, H. Matsuzaka, S. Kitagawa and K. Seki, *Angew. Chem., Int. Ed. Engl*., 1997, **36**, 1725; (*e*) S. Q. Ma, D. F. Sun, J. M. Simmons, C. D. Collier, D. Q. Yuan and H. C. Zhou, *J. Am. Chem. Soc*., 2008, **130**, 1012.

32. C. J. King, *Separation Progress*, McGraw-Hill, New York, 2nd edn, 1980. 2003.

33. R. T. Yang, *Adsorbents: Fundamentals and Applications*, John Wiley & Sons, Hoboken, 2003.

34. B. L. Karger, R. L. Snyder and H. Horvath, *An Introduction to Separation Science*, Wiley, New York, 1973.

35. (*a*) P. Kanoo, S. K. Reddy, G. Kumari, R. Haldar,C.Narayana,S.Balasubramanian and T. K. Maji, *Chem. Commun*., 2012, **48**, 8487; (*b*) D. Britt, H. Furukawa, B. Wang, T. G. Glover, and O. M. Yaghi, *PNAS*, 2009, **106**, 20637; (*c*) P. Nugent, Y. Belmabkhout, S. D. Burd, A. J. Cairns, R. Luebke, K. Forrest, T. Pham, S. Ma1, B. Space, L. Wojtas, M. Eddaoudi and M. J. Zaworotko1, *Nature*, 2013, **495**, 80; (*d*) M. Dincă and J. R. Long, *J. Am. Chem. Soc*., 2005, **127**, 9376.

36. S. Q. Ma, X. S.Wang, C. D. Collier, E. S. Manis and H.-C. Zhou, *Inorg. Chem*., 2007, **46**, 8499.

37. L. Pan, D. H. Olson, L. R. Ciemnolonski, R. Heddy and J. Li, *Angew. Chem., Int. Ed*., 2006, **45**, 616.

38. B. Chen, C. Liang, J. Yang, D. S. Contreras, Y. L. Clancy, E. B. Lobkovsky and O. M. Yaghi, S. Dai, *Angew. Chem. Int. Ed.*, 2006, **45,** 1390.

39. O. R. Evans, H. L. Ngo and W. B. Lin, *J. Am. Chem. Soc.*, 2001, **123**, 10395.

40. (*a*) S. Hasegawa, S. Horike, R. Matsuda, S. Furukawa, K. Mochizuki, Y. Kinoshita and S. Kitagawa, *J. Am. Chem. Soc.*, 2007, **129**, 2607; (*b*) K. Schlichte, T. Kratzke and S. Kaskel, *Microporous Mesoporous Mater*., 2004, **73**, 81; (*c*) A. Henschel, K. Gedrich, R. Kraehnert and S. Kaskel, *Chem. Commun*., 2008, 4192.

41. M. D. Allendorf, C. A. Bauer, R. K. Bhaktaa and R. J. T. Houka, *Chem. Soc. Rev*., 2009, **38**, 1330.

42. G. J. McManus, J. J. Perry, M. Perry, B. D. Wagner and M. J. Zaworotko, *J. Am. Chem. Soc*., 2007, **129**, 9094.

43. B. D. Wagner, G. J. McManus, B. Moulton and M. J. Zaworotko, *Chem. Commun*. 2002, 2176.

44. Y. Takashima, V. M. Martínez, S. Furukawa, M. Kondo, S. Shimomura, H. Uehara, M. Nakahama, K. Sugimoto and S. Kitagawa, *Nat. Commun*., 2011, **2**, 168.

45. M. D. Allendorf, C. A. Bauer, R. K. Bhakta, R. J. T. Houk, *Chem. Soc. Rev*., 2009,

38, 1330.

46. (*a*) A. Lan, K. Li, H. Wu, D. H. Olson, T. J. Emge, W. Ki, M. Hong and J. Li, *Angew. Chem. Int. Ed.*, 2009, *48*, 2334; (*b*) S. Mohapatra, S. Adhikari, H. Riju and T. K. Maji, *Inorg. Chem.*, 2012, **51**, 4891.

47. C. Y. Lee, O. K. Farha, B. J. Hong, A. A. Sarjeant, S. T. Nguyen and J. T. Hupp, *J. Am. Chem. Soc*., 2011, **133**, 15858.

48. C. -T. Chen and K. S. Suslick, *Coord. Chem. Rev.,* 1993, **128**, 293.

49. C. N. R. Rao, A. K. Cheetham and A. Thirumurugan, *J. Phys. Condens. Matter* 2008, **20**, 083202.

50. S. J. Blundell and F. L. Pratt, *J. Phys.Condens*. *Matter*., 2004, **16**, R771.

51. (*a*) M. Kurmoo, H. Kumagai, K. W. Chapman, C. J. Kepert, *Chem. Commun.*, 2005, 3012; (*b*) H. Kumagai, M. A.-Tanaka, K. Inoue, M. Kurmoo, *J. Mater. Chem.*, 2001, **11**, 2146; (*c*) C. M. Nagraja, J. N. Behera, T. K. Maji, S. K. Pati and C. N. R. Rao, *Dalton Trans.*, 2010, **39**, 6947; (*d*) A. Hazra, P. Kanoo and T. K. Maji, *Chem. Commun.*, 2011, **47**, 538.

52. (*a*) E. Katz and I. Willner, *Angew. Chem. Int. Ed*. 2004, **43**, 6042; (*b*)W. Lin, W. J. Rieter and K. M. L. Taylor, *Angew. Chem., Int. Ed*., 2009, **48**, 650.

53. A. M. Spokoyny, D. Kim, A. Sumrein and C. A. Mirkin, *Chem. Soc. Rev*., 2009, **38**, 1218.

54. I. Imaz, J. Hernando, D. R.-Molina and D. Maspoch, *Angew. Chem., Int. Ed*., 2009, **48**, 2325.

54. S. Jung and M. Oh, *Angew. Chem., Int. Ed*., 2008, **47**, 2049.

55. A. Carne´, C. Carbonell, I. Imaz and D. Maspoch, *Chem. Soc. Rev.*, 2011, **40**, 291

57. W. J. Rieter, K. M. Pott, K. M. L. Taylor and W. B. Lin, *J. Am. Chem. Soc*., 2008, **130**, 11584.

58. K. M. L. T.-Pashow, J. D. Rocca, Z. Xie, S. Tran and W. Lin, *J. Am. Chem. Soc*., 2009, **131**, 14261.

45. M. D. Allendorf, C. A. Bauer, R. K. Bhakta, R. J. T. Houk, *Chem. Soc. Rev*., 2009,

59. P. Horcajada, T. Chalati, C. Serre, B. Gillet, C. Sebrie, T. Baati, J. F. Eubank, D. Heurtaux, P. Clayette, C. Kreuz, J.-S. Chang, Y. K. Hwang, V. Marsaud, P.-N. Bories, L. Cynober, S. Gil, G. Fe´rey, P. Couvreur and R. Gref, *Nat. Mater*., 2010, **9**, 172.

60. W. J. Rieter, K. M. L. Taylor, H. Y. An, W. L. Lin and W. Lin, *J. Am. Chem. Soc*., 2006, **128**, 9024.

61. K. M. L. Taylor, A. Jin and W. Lin, *Angew. Chem., Int. Ed*., 2008, **47,** 7722.

62. K. H. Park, K. Jang, S. U. Son and D. A. Sweigart, *J. Am. Chem.Soc*., 2006, **128**, 8740.

63. D. Tanaka, A. Henke, K. Albrecht, M. Moeller, K. Nakagawa, S. Kitagawa and J. Groll, *Nat. Chem*., 2010, **2**, 410.

64. (*a*) T. Tsuruoka, S. Furukawa, Y. Takashima, K. Yoshida, S. Isoda, and S. Kitagawa, *Angew. Chem. Int. Ed*., 2009, **48**, 4739; (*b*) W. Cho, H. J. Lee and M. Oh, *J. Am. Chem. Soc*., 2008, **130**, 16943; (*c*) S. K. Nune, P. K. Thallapally, A. Dohnalkova, C. Wang, J. Liu and G. J. Exarhos, *Chem. Commun*., 2010, **46**, 4878.

65. (*a*) N. Kerbellec, L. Catala, C. Daiguebonne, A. Gloter, O. Stephan, J. C. Bunzli, O. Guillou and T. Mallah, *New J. Chem*., 2008, **32**, 584; (*b*) S.-L. Zhong, R. Xu, L.-F. Zhang, W.-G. Qu,. G.-Q. Gao,. X.-L. Wub and A.-W. Xu, *J. Mater. Chem*., 2011, **21**, 16574.

66. (*a*) M. Lahav, A. N. Shipway and I. Willner, *J. Chem. Soc. Perkin Trans*. 1999, **2**, 1925; (*b*) W. Chen, D. Grouquist and J. Roark, *J. Nanosci. Nanotechnol*. 2002, **2**, 47.

67. A. N. Shipway and I. Willner, *Chem. Commun*. 2001, **20**, 2035.

68. (*a*) D. L. Feldheim and C. D. Keating, *Chem. Soc. Rev*. 1998, **27**, 1; (*b*) T. W. Kim, D. C. Choo, J. H. Shim and S. O. Kang, *Appl. Phys. Lett*. 2002, **80**, 2168.

69. J. Liu, M. Gomez-Kaifer and A. E. Kaifer, *Structure and Bonding*, 2001, **99**, 141.

70. D. L. Feldheim, K. C. Grabar, M. J. Natan and T. E. Mallouk, *J. Am. Chem. Soc*. 1996, **118**, 7640.

71. (*a*) V. Escriou, M. CarriTre, D. Scherman and P. Wils, *Adv. Drug Delivery Rev*. 2003, **55**, 295; (*b*) A. G. Tkachenko, H. Xie, D. Coleman, W. Glomm, J. Ryan, M. F. Anderson, S. Franzen and D. L. Feldheim, *J. Am. Chem. Soc*. 2003, **125**, 4700.

72. I. Brigger, C. Dubernet and P. Couvreur, *Adv. Drug Delivery Rev*. 2002, **54**, 631.

73. C. Aymonier, U. Schlotterbeck, L. Antonietti, P. Zacharias, R. Thomann, J. C. Tiller and S. Mecking, *Chem. Commun*. 2002, **24**, 3018.

74. P. Chaturbedy, S. Chatterjee, R. B. Selvi, A. Bhat, M. K. Kavitha, V. Tiwary, A. B. Patel, T. K. Kundu+,T. K. Maji and M. Eswarmurthy, *J. Mater. Chem. B*, 2013, **1**, 939.

Chapter 2

Coordinatively Modulated Tunable Nanoscale Morphologies in MOF: Unprecedented 'Off-On' Porosity, CO_2 Uptake Characteristics and Solvent Dependent Emission Properties

Abstract

This chapter reports size and shape-controllable fabrication of bulk MOF $\{[Zn_2(H_2dht)(dht)_{0.5}(azpy)_{0.5}(H_2O)]\cdot 4H_2O\}_n$ (**1**) to nanoscale by adopting very well-known coordination modulation method. A comparative examination based on two different types of modulators has been carried out in order to study the relative effects on the size and morphological aspects in nanoscale. Sodium formate and dodecanoic acid have been purposely chosen and found to distinctly influence the morphologies from nanosheets through nanorods (hexagonal cross section) to hexagonal nanoparticles and finally nanospheres (descending order of size) in a controlled manner. Gas sorption measurements revealed size and morphology dependent unprecedented off/on N_2 uptake and different CO_2 uptake characteristics respectively. Furthermore, highly luminescent isomorphous compound $\{[Zn_2(H_2dht)(dht)_{0.5}(bpee)_{0.5}(H_2O)]\cdot 4H_2O\}_n$ (**2**) has been synthesized and characterized in bulk as well as in nanoscale. The ligand H_2dht is luminescent due to well-known ESIPT process and utilising this, solvatochromism has been performed with these isomorphous nanocrystals and studied in details.

2.1 Introduction

Metal–organic frameworks (MOFs) or porous coordination polymers (PCPs) are a new class of porous materials assembled through inorganic metal ions with rigid/ flexible polytopic organic linkers. Considering the different structural features and the variable functionalities with tunable properties, these have been used in the field of gas storage and separation, catalysis, ion exchange, sensing, molecular recognition and drug delivery.[1-7] To date, research on MOFs has been mainly concerned about the bulk crystalline powder and focused to correlate the physical and chemical properties with the crystal structure. Recently, the synthesis of nanosized MOFs (NMOFs) has been found to significantly contribute due to considerable high value of surface area to volume (S/V) ratio and corresponding decrease in diffusion barrier. These NMOFs have been found to be potentially applicable from liquid phase catalysis, adsorption to porous membranes, thin film devices etc.[8] It also offers an interesting approach to design functional luminescent nanomaterials for different biological and biomedical purposes for example magnetic resonance imaging contrast agents, biosensing, biolabeling, and drug delivery applications.[9]

Researches on nanoscale MOF, controlling the size, morphology and finally prediction over the respective properties, are still at a preliminary stage. Control over size and morphology would not only explore these new types of nanomaterials in future but will also upgrade the discoveries of their novel functional properties.[8-13] Materials with identical chemical compositions, similar metal-coordination environments but with different particle sizes and morphologies, has been considered as an alternative route towards tuning of surface area, gas storage and selectivity.[8,13,15]. But there is no such comparative report, where the effect of different capping agents on the size and morphological aspects has been explored on an identical system. Solvatochromic effect in luminescent NMOFs also has not been studied which could be potentially effective in biological field for different purposes mentioned above.

Several synthetic strategies [14, 15, 16] have been adopted for the synthesis of nano MOFs such as reverse micelles, surfactant mediated hydrothermal synthesis, microwave assisted method, sonochemistry and coordination modulation. But the precise control of nanoscale crystal morphology over wide distribution still remains challenging. Here, in this

study, coordination modulation method has been chosen as a synthetic strategy for fabrication of bulk MOF to NMOF.

We have chosen a porous non-interpenetrated luminescent framework $\{[Zn_2(H_2dht)(dht)_{0.5}(azpy)_{0.5}(H_2O)]\cdot 4H_2O\}_n$ (**1**) (H_2DHT = 2,5-dihydroxyterephthalic acid, azpy = 4,4′-azobipyridine)[17] for fabrication to nanoscale. This Framework is structurally distinguishable from other regular systems, generally we encounter with.[1e] Bulk **1** shows highly selective CO_2 adsorptions over other gases, such as N_2, H_2, O_2 and Ar, at 195 K.

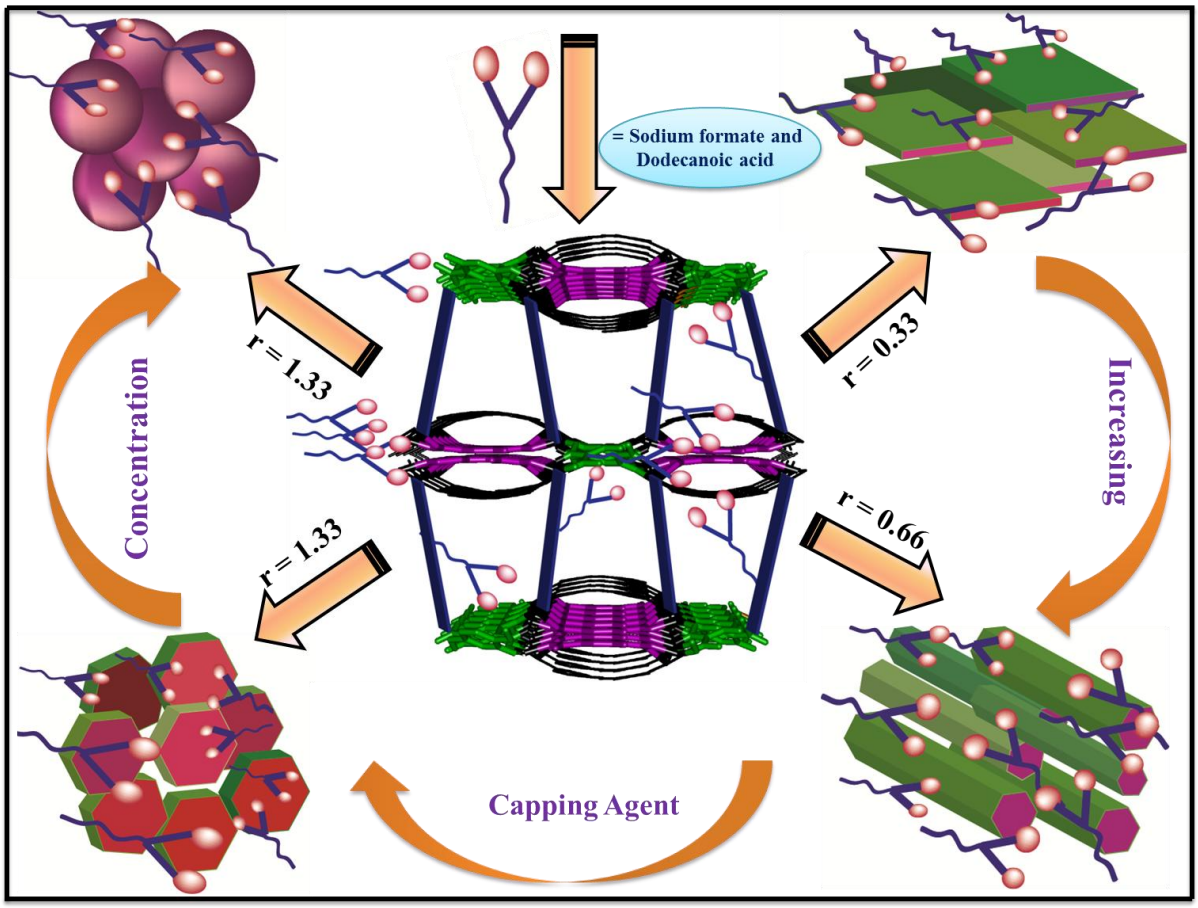

Scheme 1: Schematic representation of the synthetic strategy used for fabrication of 3D MOF to nano morphologies by applying conventional coordination modulation method. The addition of capping agent with the same functionality as organic linkers impedes the coordination interaction between metal ions and organic linkers and perturbs the rate of framework extension into nanoscale.

Photoluminescence studies show that, **1** luminesces green emission (λ_{max} at 530 nm) due to the excited-state intramolecular proton-transfer (ESIPT) process of the strut H_2dht linker. In

this framework, two dht linkers are involved for 2D layer construction and the remaining one is acting as a pillar.

We have envisioned that, this different structural packing of the framework might render to different morphologies on modulation and could hold different properties. Two different capping agents, dodecanoic acid and sodium formate have been chosen for studying the respective capping ability on crystal growth, size, morphology and sorption behaviour as well. Increase in modulator concentration in controlled fashion has enabled stepwise fabrication from micron sized sheet morphology to nanospheres through nanorods and hexagonal nanobeads (Scheme 1). The variations in sizes and morphologies have been found to dramatically affect the N_2 and CO_2 adsortion behaviour. In order to improve the inherent luminescence property of **1**, analogous isomorphous compound $\{[Zn_2(H_2dht)(dht)_{0.5}(bpee)_{0.5}(H_2O)]\cdot 4H_2O\}_n$ **(2)** [bpee = 1,2-bis(4-pyridyl)ethylene] has been synthesized replacing azpy with isostructural bpee ligand in bulk as well as in nanoscale (**3**). Highly luminescent nanocrystals **3** have been further utilised for tunable emission through solvatochromic effect.

2.2 Experimental Section

2.2.1 Materials

All the reagents and solvents employed were commercially available and used as supplied without further purification. $Zn(NO_3)_2\cdot 6H_2O$, 2,5- dihydroxyterephthalic acid and 1,2-bis(4-pyridyl)ethylene were obtained from Sigma Aldrich Chemical Co.

2.2.2 Physical Measurements

Powder X-ray diffraction (PXRD) patterns were recorded on a Bruker D8 Discover instrument equipped with Cu-Kα radiation over the 2θ range of 5−50°. Thermogravimetric analysis (TGA) was carried out on a METTLER TOLEDO TGA 850 instrument in the temperature range of 30 - 650 °C under nitrogen atmosphere (flow rate of 50 mL min^{-1}) at a heating rate of 5 °C min^{-1}.

UV-Vis and fluorescence spectra were recorded on a Perkin Elmer Model Lambda 900 spectrophotometer and Perkin Elmer model LS 55 spectrophotometer, respectively.

The scanning electron microscopy images were obtained using Nova Nanosem 600, FEI field emission scanning electron microscope (FESEM). SEM samples were prepared by dispersing the powder samples in MeOH and then dropping 5 μL of the solution onto a small piece of silicon wafer and drying in air.

Transmission electron microscopy (TEM) images were taken with a JEOL JEM-3010 transmission electron microscope operating at 200 kV. The samples were prepared in the same way as described above but the drop cast was made onto carbon-coated TEM grid.

A Bruker diInnova scanning probe microscope used in a tapping mode was employed for all atomic force microscopy (AFM) experiments. The sample was prepared by dropping a methanol solution containing dispersed samples onto freshly cleaved silicon wafers and evaporated at room temperature. Measurements were made using silicon cantilevers. The drive frequency for tapping mode was set near the resonance frequency of cantilavers (250-350 kHz). Images were recorded in a 20 × 20 μm and 7.6 × 7.6 μm scan size window at a scan speed of 1 kHz and resolution of 512 × 512. The Nanoscope software was used to obtain the three-dimensional image representations and quantitative measurements of surface topological features.

2.2.3 Adsorption Studies

Adsorption measurements of CO_2 at 195 K and N_2 at 77 K were carried out using QUANTACHROME QUADRASORB-*SI* analyser. The carbon dioxide gas used for the measurements is of scientific/research grade with 99.999% purity. For the measurements, approximately 100 mg of samples were taken in a sample holder and degassed at 433 K under 10^{-1} Pa vacuum for about 12 hours. Helium gas (99.999% purity) at a certain pressure was introduced in the gas chamber and allowed to diffuse into the sample chamber by opening the valve. The amount of gas adsorbed was calculated readily from pressure difference (P_{calc}- P_e), where P_{calc} is the calculated pressure with no gas adsorption and P_e is the observed equilibrium pressure. All operations were computer-controlled and automatic.

2.2.4 Preparation of Nanoparticles

2.2.4.1 Using Sodium Formate as Capping Agent

Disodium salt of 2, 5-dihydroxyterephthalic acid (Na_2H_2dht) (0.048 g, 0.187 mmol) was dissolved in 5 mL of water. 4,4′-azobipyridine (azpy) (0.062 mmol, 0.011 g) was

dissolved in 45 mL of 2-methoxyethanol. The solutions of Na_2H_2dht and azpy were mixed together and stirred for 30 min to prepare the ligand solution. Now $Zn(NO_3)_2 \cdot 6H_2O$ (0.25 mmol, 0.074 g) and sodium formate with three different concentrations [0.062 mmol (4 mg,); 0.125 mmol (8 mg) and 0.25 mmol (16 mg), namely **F-1**, **F-2** and **F-3** respectively] were dissolved in 50 mL of methanol to prepare the metal solution. Now the metal solution is added to the ligand solution dropwise from dropping funnel and the whole mixture is stirred for 2 days. After two days the resulting samples were separated through centrifugation and washed with 2-methoxyethanol/MeOH (1:1) mixture for 4-5 times and air dried. Therefore based on formate concentrations three different samples (F1, F2 and F3) have been prepared.

2.2.4.2 Using Dodecanoic Acid as Capping Agent

Similar above procedure has been followed except dodecanoic acid is used here as capping agent instead of sodium formate. The concentration of dodecanoic acid is following; 0.062 mmol (13 mg); 0.125 mmol (25 mg) and 0.25 mmol (50 mg), resulting to three samples **D-1**, **D-2** and **D-3**, respectively.

2.2.4.3 Preparation of Analogues Compound (2) and Fabricated Nanocompound (3) Using Sodium Formate

Same procedure is followed mentioned above except 1,2-bis(4-pyridyl)ethylene (bpee) is used for preparing **2** instead of 4,4′-azobipyridine (azpy). And for modulation, sodium formate [0.25 mmol (50 mg)] is used to synthesize **3** following similar procedure.

2.3 Results and Discussion

2.3.1 Thermal and PXRD analysis

The phase purity and the crystalline nature of the particles have been confirmed from PXRD (Fig. 1 and 2). Noticeably, the broadening of the Bragg's reflections is observed, suggesting the gradual formation of smaller crystals with narrower size distribution. The thermogravimetric analyses for **1** and other nanocrystals show similar stepwise weight loss, first for guest water molecules and then for coordinated water molecule suggesting the structural integrity has been maintained at nanoscale throughout the course of the experiment.

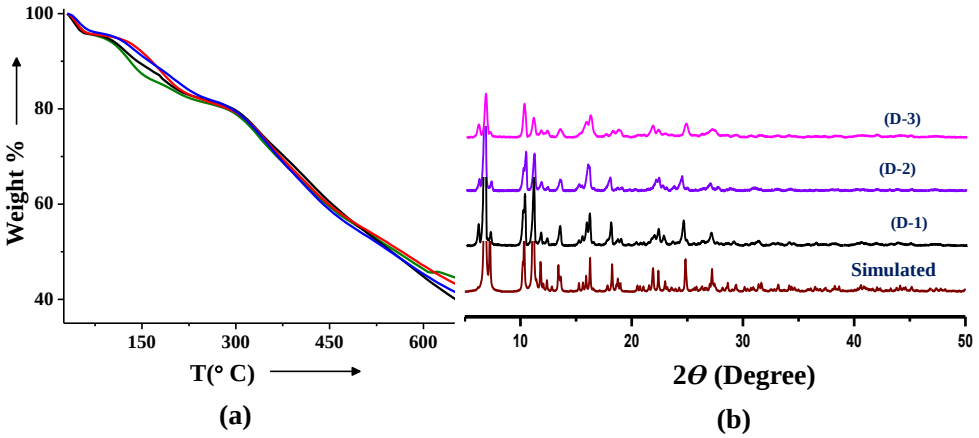

Fig. 1: (a) TGA of blue: bulk **1**, red: **D-1**; green: **D-2** and black: **D-3.**

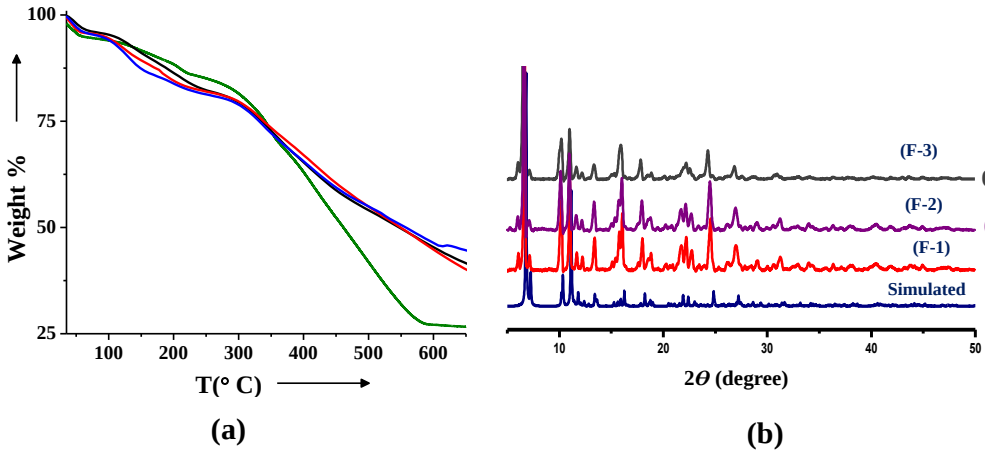

Fig. 2: (a) TGA of red: bulk **1**, green: **F-1**; black: **F-2** and blue: **F-3.**

2.3.2 Fabrication to Nanoscale through Coordination Modulation Method

In order to obtain closer insight about the effect of different capping agents in size distribution as well as on crystal surface environment, several sets of experiments have been performed by using surfactant dodecanoic acid (D-series) with long alkyl chain and sodium formate (F-series) with no tail. In two sets of experiments (Chart 1), the ratio (r) of capping agent to the ligand dht has been varied across the range from 0.33 to 1.33 (r = 0.33, 0.66 and 1.33) keeping the other reaction conditions identical. When r = 0.33 (i.e. 0.062 mmol), sheet nanosheets have been observed. Increase of capping agent concentration by double (r = 0.6;

0.125 mmol) led to nanorods with hexagonal cross sectional area. When r = 1.33 (i.e. 0.25 mmol), hexagonal nanoparticle (**F-3**) and nanospheres (**D-3**) have been found to be observed (Fig. 1 and 2).

Entity	Conc. (mmol)	Weight taken (g)	Morphology
Na_2H_2DHT (Ligand)	0.187	0.048	Bulk
azpy (Ligand)	0.062	0.011	
$Zn(NO_3)_2$ (Metal Soln)	0.25	0.074	
HCO_2Na (Modulator)	0.062 F-1	0.04	Sheet
	0.125 F-2	0.08	Nanorod with Hexagonal Cross Sectional Area
	0.25 F-3	0.012	Hexagonal Nanoparticles
Dodecanoic acid	0.062 D-1	0.012	Sheet
	0.125 D-2	0.025	Nanorod with Hexagonal Cross Sectional Area
	0.25- D-3	0.05	Nanospheres

Chart 1: Two sets of experiments with modulators (sodium formate and dodecanoic acid) at different concentrations.

The morphologies and the particle sizes of NMOFs were investigated by field emission scanning electron microscopy (FESEM), transmission electron microscopy (TEM) and atomic force microscopy (AFM) .The **D-1** (Fig. 3A) and **F-1** (Fig. 4A) both have large sheet like morphology and the sizes range in several micrometer (length ~ 15 ± 9 μm and width ~ 12 ± 10 μm). It has been further characterised through AFM study (Fig. 3E and 4E). AFM study shows the 3D view of these particles and their corresponding height profiles. For D-1 and F-1, height range in ~ 500 ± 300 nm and hence the particles are confirmed to be nanosheets. Increase in additive concentration (r = 0.66) resulted into nanorods (**D-2** and **F-2**) in both cases (Fig. 3B and 4B). The average length of major axis and minor axis of **D-2** are ~ 1.7 ± 0.04 μm and ~ 200 ± 20 nm respectively (Fig. 3F). On the contrary, in case of **F**-series the size distribution is slightly different. For **F-2**, average length of major axis and minor axis are varying within ~ 2.3 ± 0.02 μm and ~ 1 ± 0.1 μm respectively (Fig. 4F). Further increase has been led to significant decrease in length and it results into hexagonal nanoparticles (**F-3**) of ~ 170 ± 30 nm and nanospheres (**D-3**) of ~ 60 ± 30 nm in diameter (Fig. 3C and 4C) with

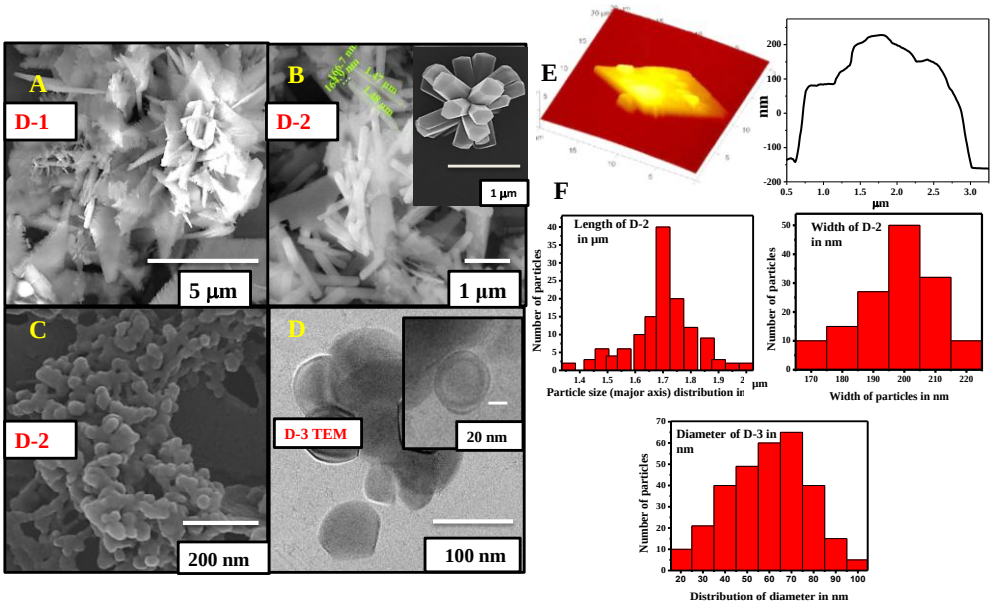

Fig. 3: FESEM images of (a) Nanosheet morphology (**D-1**) (b) nanorod (**D-2**) with hexagonal cross sectional area (c) nanosphere (**D-3**) (d) TEM image of nanosphere (**D-3**). E) AFM 3D surface view along 20× 20 µm scan and corresponding height profiles respectively (F) Size distributions.

narrower size distribution. However, the particles have been observed to be agglomerated when the r value of the sodium formate and dodecanoic acid is more than 0.66. Here the

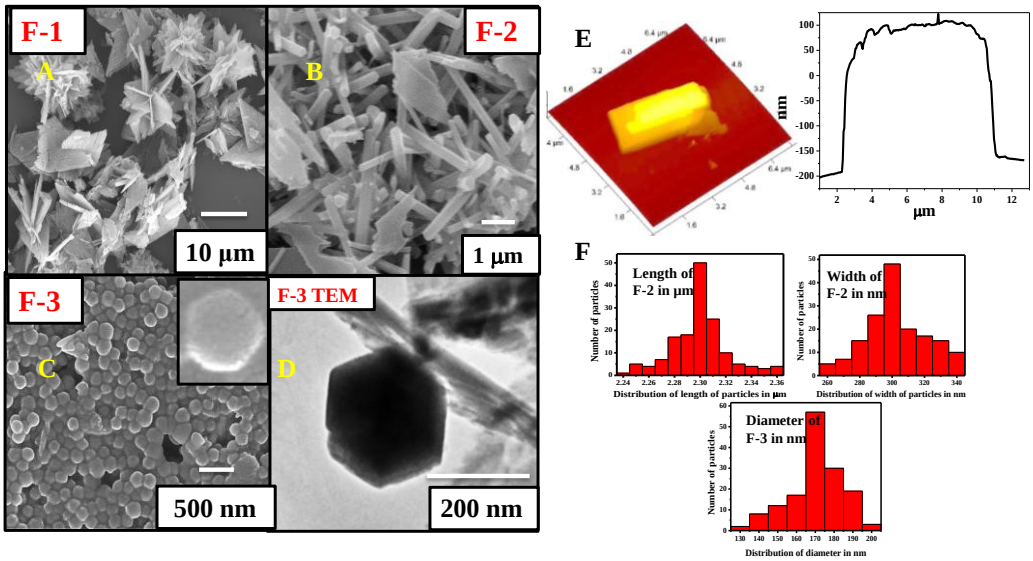

Fig. 4: FESEM images (A) Nanosheet (**F-1**) morphology (B) nanorods (**F-2**) with hexagonal cross sectional area (C) hexagonal nanoparticle (**F-3**) (D) TEM image of one hexagonal nanoparticle (E) AFM 3D surface view along 7.6× 7.6 µm scan and corresponding height profiles respectively (F) Size distributions.

particle size could have been increased because of accelerated nucleation of comparatively higher number of nuclei in presence of higher concentration of capping agent.[16]

When a particle grows, the crystal facets shows tendency to form on the low-index planes and eventually minimizes the surface energy. During the crystal growth process, the additives might get selectively adsorbed on some specific crystal surfaces of the crystal nuclei, and effectively lowers of energy of the particles[16]. This induces particles epitaxy and finally assembled into different morphologies for example sheet, nanorods, hexagonal nanoparticles and nanospheres.

2.3.3 Adsorption Studies

To acquire more information about porous properties at nanoscale, N_2 and CO_2 sorption isotherms (Fig. 5) were recorded for NMOF at 77 K and 195 K respectively. Despite of having sufficient pore size, as-synthesised compound shows no considerable uptake of N_2 (kinetic diameter ~ 3.64 Å) at 77 K. An unprecedented behaviour has been observed in N_2 sorption isotherm in case of different NMOFs with different size and morphologies obtained from different capping agents. For adsorption measurements of **F-1**, **D-2**, **F-3** and **D-3** have been considered as representatives regarding different morphologies. Gradual decrease in particle size and successive increase in surface area are certainly due to stepwise decrease in diffusion barrier.[8,15,16] The **F-1** and **D-2** both exhibit BET surface area of ~ 5 $m^2 g^{-1}$ respectively with type II sorption profile (Fig. 5). Unexpectedly with further decrease, sharp improvement on surface area governs the sorption types. The hexagonal nanoparticles **F-3** exhibit BET surface area of ~ 60 $m^2 g^{-1}$ whereas nanospheres **D-3** has been found to achieve further enhancement over BET surface area of ~ 340 $m^2 g^{-1}$. Steep uptake at low pressure and reversible type I sorption profile clearly suggests microporous behaviour. In the relative high pressure region (near P/P_0 ~ 1), **F-3** and **D-3** show a sudden increment in amount of gas uptake which can be correlated to sorption of N_2 on the higher crystalline surfaces of smaller nanoparticles . Based on the above observations it can be considered that there must be some critical size below which surface energy governs over diffusion barrier effectively (at least in this system).

But the results obtained from CO_2 sorption (Fig. 6) isotherm have been found to be slightly different. The final amount uptake by as-synthesised bulk compound was found to be

108 cm^3 g^{-1} (~ 21 wt%; 2.56 molecules per formula unit). Unexpectedly the highest amount has been adsorbed by **F-3**, 132 cm^3 g^{-1} (~25.9 wt%; 3.1 molecules per formula unit) instead

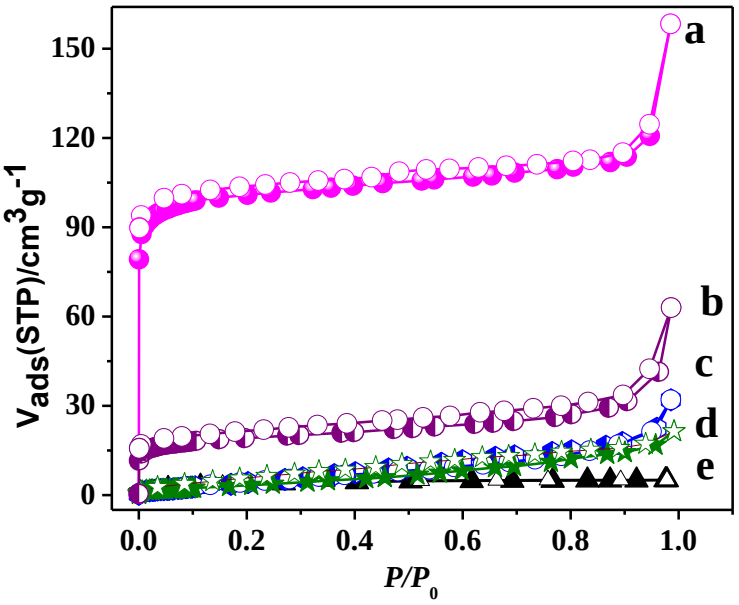

Fig. 5: N_2 adsorption isotherm at 77 K; (a): **D-3** (b) **F-3** (c) **D-2** (d) **F-1** and (e) **1.**

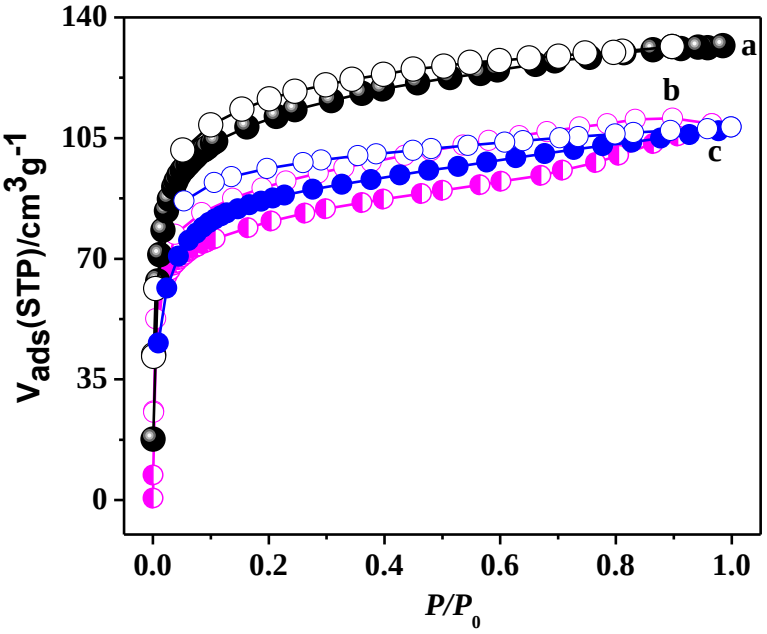

Fig. 6: CO_2 adsorption isotherm at 195K (a) **F-3** (b) **D-3** (c) **1.**

of **D-3** which is of 109 cm^3 g^{-1} (~21.4 wt%; 2.59 molecules per formula). The N_2 adsorption study on **D-3** ensures there is no possibility of presence of modulator on the surface of nanocrystals after the washing process and it is not inducing any significant defect in the framework itself. This adsorption behaviour indicates that apart from surface area there must be one more parameter which is also responsible as well.

It is the morphology of the nanoparticles that might be responsible for effecting diffusion barrier. CO_2 is a polar molecule possessing quadrupole moment of CO_2: 4.30×10^{26} /esu cm^2 and it is expected to interact differently with the adsorptive site of pore compared to inert N_2. Isosteric heat of adsorption (q_{st},ϕ) as calculated by Dubinin-Radushkevich (DR) equation for **1** is ~ 33.4 kJ mol^{-1} whereas **F-3** shows ~ 35.95 kJ mol^{-1} suggesting stronger interaction. So it can be speculated that not only the surface area but also the morphology both are responsible for giving rise to such different behaviour.

With gradual decrease of particle size, the proportion of the atoms lying on the surface bed will increase as well. The atoms lying near the surface area are found to possess higher surface and binding energy compared to internal atoms. Therefore the surface atoms are able to display unsaturated properties and easier to interact with adsorbates and eventually improves their adsorption behaviour as well. In this case, it might have so happened that on modulation of specific crystal facets, the pore channels or cavities along that particular direction have more exposed to adsorbates. This might be reasoned for higher uptake of CO_2 for **F-3** than **D-3**.

2.3.4 Analogous Compound and Fabrication to Nanoscale: Solvatochromic Effect

The photoluminescence studies of **1** exhibited green emission (λ_{max} 530 nm) in the solid state with large Stokes shift at room temperature [18] due to the H_2dht linker based well known ESIPT phenomenon. But absorption of framework strut 4,4′-azobipyridine in that corresponding region quenches the emission a bit. In order to modify this, isostructural 1,2-bis(4- pyridyl)ethylene (bpee) has been introduced (**2**) replacing only –N=N- (azo) functional group by alkene. Compound **2** has also been fabricated to nanoscale (**3**) in order to enhance the processibility and compatibility in solution phase. Well correspondence in PXRD and similar thermal stability ensure the crystallinity and purity of phase (Fig. 7). FESEM images

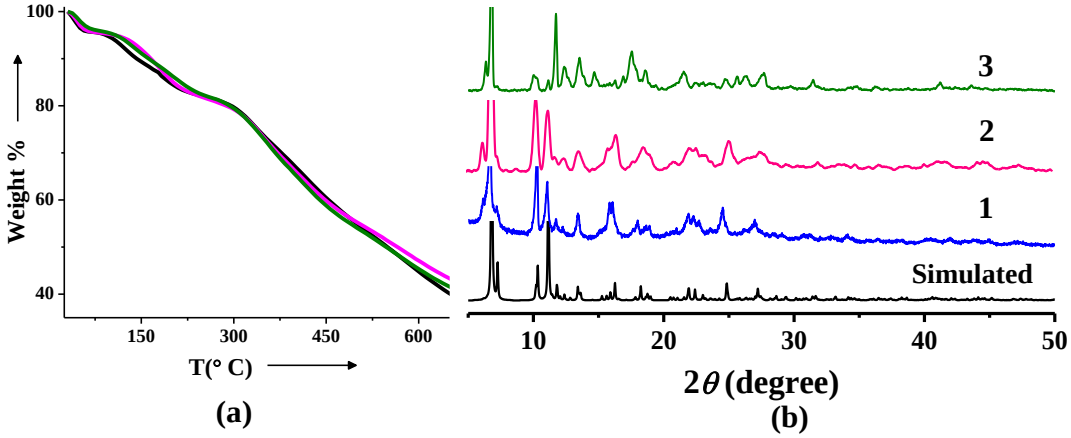

Fig. 7: (a) TGA of Pink: bulk **1**, green: **2**; black: **3** (b) PXRD of simulated, **1**, **2**, and **3.**

show these are oval shaped particles and the sizes range ~ 350 ± 200 nm. Confocal images exhibit that the particles are highly luminescent nanoparticles (λ_{max} at 370 nm) and could be potentially applicable for different biological purposes.

2.3.5 Photophysical Studies

It has been possible to tune the emission (Fig. 8) of **3** when exposed to different solvents. For example, in THF it exhibits blue emission, in MeOH it is cyan, in DMSO it shows green luminescence (λ_{max} at 511 nm) and in water it luminesces yellow (λ_{max} at 540 nm). The comparative lesser intense band in THF and in MeOH in visible region (ESIPT band) compared to main UV band (Fig. 8) in the absorption spectra clearly suggest the preferable dominance of enol tautomers. But comparative higher intensity in DMSO and very higher intensity in water indicate predominance of keto tautomer.

It has been also verified by photoluminescence spectra (Fig. 8). In THF, the emission is blue shifted (λ_{max} 453 nm) compared framework emission in solid state (λ_{max} 530 nm), in MeOH it is cyan, slightly red shifted compared to THF (λ_{max} at 496 nm), In DMSO, it is further bathochromically shifted to green (λ_{max} at 511nm) and in water it is further shifted to yellow (λ_{max} at 540 nm). The blue and cyan emissions are indicative of preference for enol form (E*) over keto tautomer (K*) but green and yellow emissions are responsible for keto tautomer.[19] The broadness of the bands suggests the interplay between intermolecular and intramolecular H-bonding and it results into blue and red shifted emissions respectively. This solvent

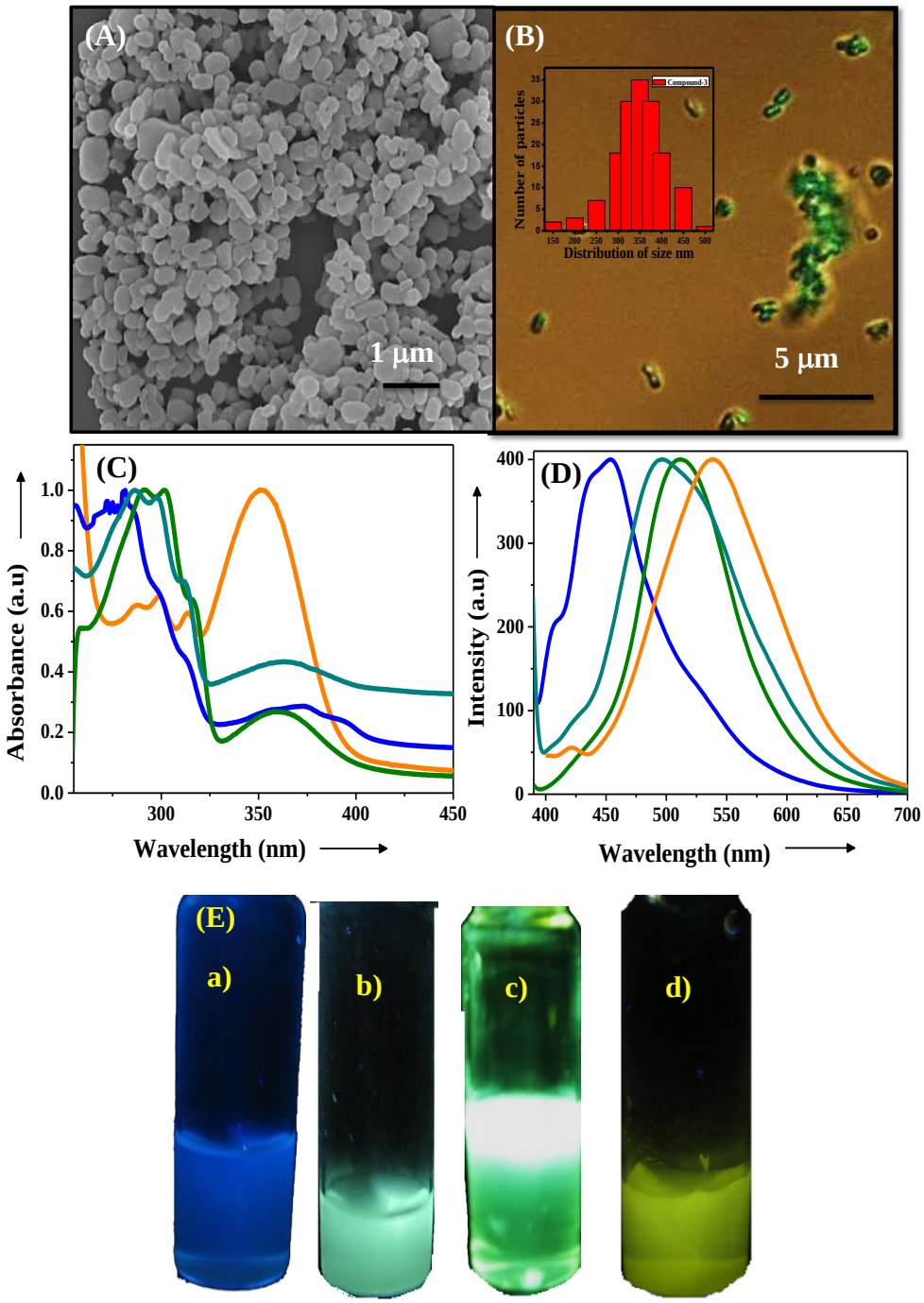

Fig. 8: (A) FESEM images of oval shaped nanoparticles (**3**) (B) Confocal image of **3** (λ_{max} = 370 nm) and in inset particle size distribution has been shown (C and D) UV-Vis and photoluminescence spectra of **3** in different solvents; blue: 3 @ THF; Cyan: 3 @ MeOH; green: 3 @ DMSO; yellow: 3 @ water and (E) Photograph taken for **3** under UV lamp; a. THF b. MeOH c. DMSO and d. water.

induced red shifted broad range of emissions could be explained on the basis of four level photocycle of ESIPT process[19] and from here the solvent dependent predominance of keto and enol tautomers can be easily understood.

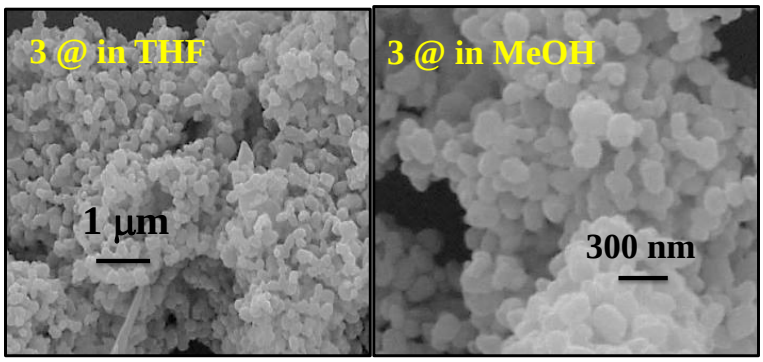

Fig. 9: SEM images of **3** dispersed in THF and MeOH (indicating the particles are stable in THF and MeOH).

2.3.6 Adsorption Studies

Nitrogen (N_2) and carbon dioxide (CO_2) adsorption studies (Fig. 10) have been performed to probe the porous nature of **2**. N_2 adsorption study at 77 K showed typical type II adsorption profile suggesting surface adsorption. The final amount uptake of CO_2 by **2** at 195 K is found to be ~ 85 cm^3 g^{-1}. The reason for smaller uptake is due to presence of carbon atoms in alkene functional group in bpee (in **2**) instead of nitrogen (azo) (in **1**) which causes weaker interaction with CO_2 molecule.

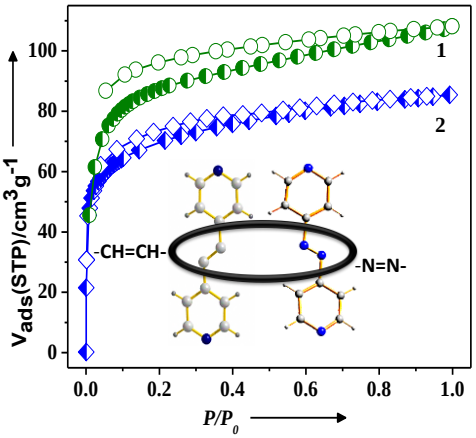

Fig. 10: CO_2 adsorption isotherm at 195 K; green: **1** and blue **2.**

2.4 Conclusions

Here we have reported size and shape-controlled fabrication of bulk MOF into nano MOF (NMOF) adopting coordination modulation method. This experiment has been followed up preferring two completely different types of modulators (sodium formate/dodecanoic acid with long alkyl chain). It has been possible to modulate different sized and shaped nanoparticles, from nanosheet to hexagonal disks or spherical particles with unprecedented increase in surface area. N_2 and CO_2 sorption experiments highlighted the effect of the size, morphology. To the best of our knowledge, this would be the first report where after fabrication to nanoscale, a compound which does not take N_2 (at 77 K) in bulk scale at all, have exhibited such an drastic improvement in its adsorption properties due to gradual decrease in diffusion barrier. Morphology dependent CO_2 has been experimentally observed but needs to be verified in details. The mechanism of modulation of the capping agents is currently under investigation and probably might help to clarify the observations obtained.

2.5 References

1. (a) G. Férey, *Chem. Soc. Rev*., 2008, **37**, 191; (b) S. Kitagawa, R. Kitaura and S. I. Noro, *Angew. Chem., Int. Ed*., 2004, **43**, 2334; (c) T. K. Maji and S. Kitagawa, *Pure Appl. Chem.*, 2007, **79**, 2155; (d) T. K. Maji, R. Matsuda and S. Kitagawa, *Nat. Mater*., 2007, **6**, 142; (e) D. J. Tranchemontagne, J. L. Mendoza-Corte´ s, M. O'Keeffe and O. M. Yaghi, *Chem. Soc. Rev*., 2009, **38**, 1257.

2. (a) H. K. Chae, M. Eddaoudi, J. Kim, S. I. Hauck, J. F. Hartwig, M. ÓKeeffe and O. M. Yaghi, *J. Am. Chem. Soc*., 2001, **123**, 11482; (b) M. Eddaoudi, D. B. Moler, H. L. Li, B. L. Chen, T. M. Reineke, M. ÓKeeffe and O. M. Yaghi, *Acc. Chem. Res*., 2001, **34**, 319; (c) L. Pan, B. Parker, X. Huang, D. H. Olson, J. Y. Lee and J. J. Li, *J. Am. Chem. Soc*., 2006, **128**, 4180; (d) R. Matsuda, R. Kitaura, S. Kitagawa, Y. Kubota, R. V. Belosludov, T. C. Kobayashi, H. Sakamoto, T. Chiba, M. Takata, Y. Kawazoe and Y. Mita, *Nature*, 2005, **436**, 238.

3. (a) P. Kanoo, R. Matsuda, M. Higuchi, S. Kitagawa and T. K. Maji, *Chem. Mater*., 2009, **21**, 5861; (b) P. Kanoo, K. L. Gurunatha and T. K. Maji, *J. Mater. Chem*., 2010, **20**, 1322; (c) S. Q. Ma, D. F. Sun, J. M. Simmons, C. D. Collier, D. Q. Yuan and H. C. Zhou, *J. Am. Chem.*

Soc., 2008, **130**, 1012; (d) P. Kanoo, R. Matsuda, R. Kitaura, S. Kitagawa and T. K. Maji, *Inorg. Chem.*, 2012, **51**, 9141. 4.(a) H. K. Liu, W. Y. Sun, W. X. Tang, T. Yamamoto and N. Ueyama, *Inorg. Chem*., 1999, **38**, 6313

5. (a) J. Fan, W. Y. Sun, T. A. Okamura, J. Xie, W. X. Tang and N. Okamura, *New J. Chem*., 2002, **26**, 199; (b) A. N. Parvulescu, G. Marin, K. Suwinska, V. C. Kravtsov, M. Andruh, V. Parvulescu and V. I. J. Parvulescu, *J. Mater. Chem*., 2005, **15**, 4234.

6. (a) P. Horcazada, C. Serre, M. Sebban, F. Taulelle and G. Férey, *Angew. Chem., Int. Ed*., 2006, **45**, 5974; (b) P. Horcazada, C. Serre, G. Maurin, N. A. Ramsahye, F. Balas, M. Vallet-Regi, M. Sebban, F. Taulelle and G. Férey, *J. Am. Chem. Soc*., 2008, **130**, 6774.

7. (a) S. Henke, R. Schmidt and J. D. Grunwaldt, *Chem. Eur. J*., 2010, **16**, 14296; (b) Z. Q. Wang and S. M. Cohen, *J. Am. Chem. Soc*., 2009, **131**, 16675.

8. S. Diring, S. Furukawa, Y. Takashima, T. Tsuruoka, and S. Kitagawa, *Chem. Mater*., 2010, **22**, 4531.

9. W. J. Rieter, K. M. L. Taylor, and W. Lin , *J. Am. Chem. Soc*. 2007, **129**, 9852.

10. C. Y. Lee, Y.-S. Bae, N. C. Jeong, O. Farha, A. Sarjeant, C. Stern, P. Nickias, R. Snurr, J. T. Hupp and S. Nguyen, *J. Am. Chem. Soc.*, 2011, **133**, 5228.

11. H. J. Lee, W. Cho, S. Jung and M. Oh, *Adv. Mater*., 2009, **21**, 674.

12. O. K. Farha, A. M. Spokoyny, K. L. Mulfort, S. Galli, J. T. Hupp and C. A. Mirkin, *small*, 2009, **5**, 1727.

13. H. Xu, X. Rao, J. Gao, J. Yu, Z. Wang, Z. Dou, Y. Cui, Y. Yang, B. Chen and G. Qian, *Chem. Commun.*, 2012, **48**, 7377.

14. A. Carne, C. Carbonell, I. Imaz and D. Maspoch, *Chem. Soc. Rev.*, 2011, **40**, 291.

15. T. Tsuruoka, S. Furukawa, Y. Takashima, K. Yoshida, S. Isoda, and S. Kitagawa, *Angew. Chem. Int. Ed*., 2009, **48**, 4739.

16. L. Hu, P. Zhang, Q. Chen,. H. Zhong, X. Hu, X. Zheng, Y. Wang, and N. Yan, *Cryst. Growth Des,*. 2012, **12**, 2257

17. J. Zhang, L. Sun, F. Xu, F. Li, H.-Y. Zhou, Y.-L. Liu, Z. Gabelicae and C. Schick, *Chem. Commun.*, 2012, **48**, 759.

18. P. Kanoo, A. C. Ghosh, S. T. Cyriac, and T. K. Maji, *Chem. Eur. J*., 2012, **18**, 237.

19 . K. Jayaramulu, P. Kanoo, S. J. George and T. K. Maji, *Chem. Commun.*, 2010, **46**, 7906.

Chapter 3

Higher CO_2 Uptake in a Nanoscale Flexible MOF Supported by Accelerated Adsorption Kinetics

So far studies on NMOFs, mostly the fabrication of non-interpenetrated frameworks have been prioritised. There is only one report where the kinetics of guest molecule adsorption in interpenetrated NMOF and bulk MOF has shown significant concern. In this work, Kitagawa *et al*. have elegantly shown how the adsorption kinetics significantly affects the sorption type and uptake capacity for both, interpenetrated NMOF and bulk.

Flexible or dynamic interpenetrated MOFs represent a unique class of materials which exhibit characteristic reversible change in their structure and corresponding properties in response to different guest molecules.[11-15] One of the most interesting features of these flexible MOFs is their stepwise sorption behaviour caused by guest induced structural transformation.[16-17] The total storage capacity, the structural transformation during

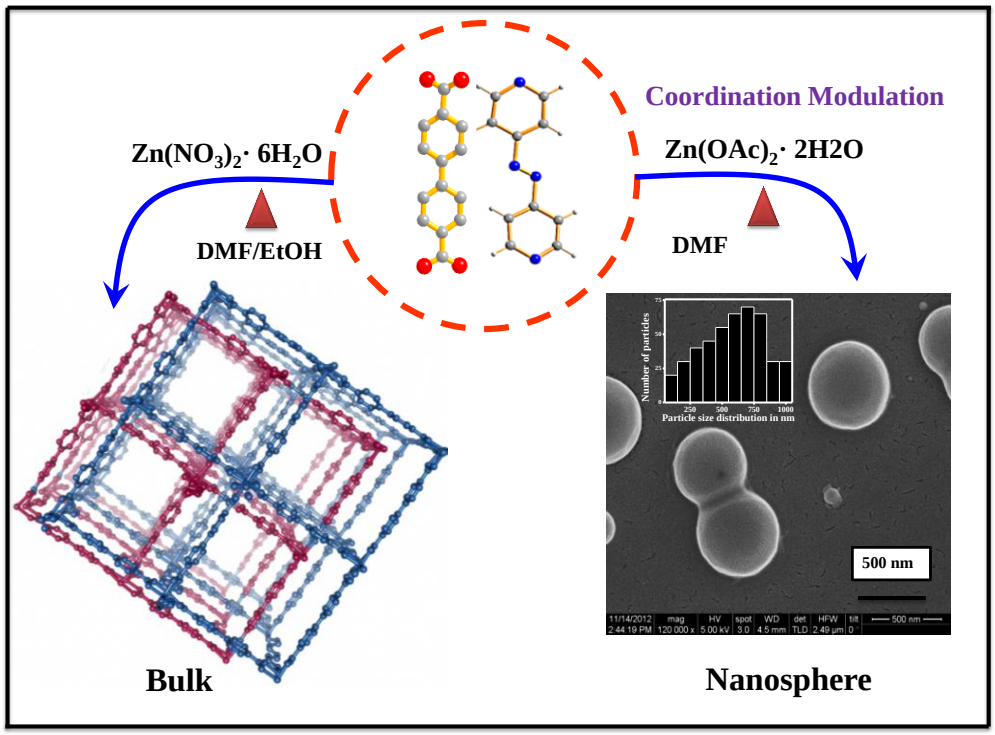

Scheme: Schematic representation of overall work

adsorption and the gate opening step at onset pressure are highly sensitive to the nature of the guest molecules. The principal reason lies in both, the kinetics and thermodynamics of adsorption process which strongly affects the stepwise sorption nature. It has been found that crystal size and crystal surface environment dramatically affects the diffusion kinetics.[18]

Very few reports have attempted to explore the effect of crystal morphology on adsorption properties in case of non-flexible system.[19,20] But through addressing the kinetics, the effect of particle size in flexible system yet to be studied in details.

In this work, synthesis, structural characterizations, and porous properties of two novel, two-fold interpenetrated 3D frameworks $\{[Zn_2(bpdc)_2(azpy)]\cdot 2H_2O\cdot DMF\}_n$ (**1**) and $\{[Zn_3(bpdc)_3(azpy)]\cdot 2H_2O\cdot 2DEF\}_n$ (**2**) [bpdc = 4,4′-biphenyldicarboxylic acid, azpy = 4,4′-azobipyridine] have reported. Both are constructed from similar organic linkers but exhibit SBU directed different structural patterns at different reaction conditions. Both frameworks show CO_2 selectivity at 195 K over other gases, such as N_2, H_2, O_2 and Ar and exhibit stepwise uptake in solvent vapour adsorption isotherms due to structural flexibility. Bulk **1** has been fabricated to crystalline nanospheres (**1N**) through well-known coordination modulation method [8,21]. **1N** has been further studied for adsorption measurements and has been found to exhibit better CO_2 storage capacity compared to bulk scale. This result prompted us to look into the phenomenon from kinetic point of view. Measurement of the adsorption kinetics of water vapour proved higher diffusion rate of adsorbates in nanosphere than bulk due to higher surface area and comparatively much smaller diffusion barrier.

3.2 Experimental Section

3.2.1 Materials

All the reagents employed were commercially available and used as provided without further purification. Metal salt was obtained from Spectrochem. 4,4′-biphenyldicarboxylic acid was obtained from Sigma Aldrich Co.

3.2.2 Physical Measurements

Elemental analysis was carried out using a Thermo Fischer Flash 2000 ElementalAnalyzer.. Thermogravimetric analysis (TGA) was carried out (Metler Toledo) in nitrogen atmosphere (flow rate = 50 mL min^{-1}) in the temperature range 30–500 °C (heating rate 3 °C min^{-1}). Powder XRD pattern of the compounds were recorded by using Mo-Kα radiation (Bruker D8 Discover; 40 kV, 30 mA).The pattern was agreed with those calculated from single crystal structure determination.

3.2.3 X-Ray Crystallography

X-ray single-crystal structure data of **1** and **2** were collected on a Bruker Smart-CCD diffractometer equipped with a normal focus, 2.4 kW sealed tube X-ray source with graphite monochromated Mo-Kα radiation (λ= 0.71073 Å) operating at 50 kV and 30 mA. The program SAINT [22] was used for integration of diffraction profiles and absorption correction was made with SADABS [23] program. All the structures were solved by SIR92 [24] and refined by full-matrix least-squares method using SHELXL-97.[25] All the hydrogen atoms were geometrically fixed and placed in ideal positions. Potential solvent accessible area or void space was calculated using the PLATON multipurpose crystallographic software.[26] All crystallographic and structure refinement data of **1** and **2** are summarized in Table 1. Selected bond lengths and angles for **1** and **2**, are given in Table 2, 3 and 4, 5 respectively**.** All calculations were carried out using SHELXL 97, [25] PLATON, [26, 27] and WinGX system, Ver 1.70.01.[28]

3.2.4 Adsorption Study

The adsorption isotherms of CO_2, H_2, N_2, Ar and O_2 using the dehydrated samples of **1** (**1′**) and **2** (**2′**) were measured by using a QUANTACHROME QUADRASORB-SI analyzer. The desolvated **1′** and **2′** have been prepared by heating at 150 °C and 170 °C under 1×10^{-1} Pa vacuum for about 12 h prior to measurement of the isotherms. Helium gas (99.999% purity) at a certain pressure was introduced in the gas chamber and allowed to diffuse into the sample chamber by opening the valve. The amount of gas adsorbed was calculated readily from pressure difference (P_{calc}- P_e), where P_{calc} is the calculated pressure with no gas adsorption and P_e is the observed equilibrium pressure. All operations were computer-controlled and automatic.

The adsorption isotherms of different solvents (MeOH, at 293 K, H_2O and C_6H_6 at 298 K) were measured in the vapour state by using a BELSORP-aqua volumetric adsorption instrument from BEL, Japan. About ~100−150 mg of **1′** and **2′** were prepared by activating at 150 °C for about 12 h under a vacuum (1×10^{-1} Pa) prior to measurement of the isotherms. The solvent molecules used to generate the vapour were degassed fully by repeated evacuation. Dead volume was measured with helium gas. The adsorbate was placed into the sample tube, then the change of the pressure was monitored, and the degree of adsorption was

determined by the decrease in pressure at the equilibrium state. All operations were computer controlled and automatic.

3.2.5 Synthesis of $\{[Zn_2(bpdc)_2(azpy)]\cdot 2H_2O\cdot DMF\}_n$ (1)

A mixture containing $Zn(NO_3)_2\cdot 6H_2O$ (0.1 mmol, 0.030 g), bpdc (0.1 mmol, 0.024 g) and azpy (0.05 mmol, 0.009 g) was suspended in DMF/ethanol (1:1) mixture (10 mL) in a glass vial (30 mL) and heated to 80 °C for a period of 3 days. The dark block shaped red crystals of **1** were then collected after washing with DMF/ ethanol for several times.Yield: 87%. Anal. Calc. for $C_{41}H_{35}Zn_2N_5O_{11}$: C: 53.76; H: 3.45; N: 7.21; Found C: 53.70; H: 3.43; N: 7.19. FTIR (KBr pellet, 4000–400 cm^{-1}): 3150–3600(S), 3052(w), 1652(w), 1610(S), 1525(m), 1398(S).

3.2.6 Synthesis of $\{[Zn_3(bpdc)_3(azpy)]\cdot 2H_2O\cdot 2DEF\}_n$ (2)

A mixture containing $Zn(NO_3)_2\cdot 6H_2O$ (0.1 mmol, 0.030 g), bpdc (0.1 mmol, 0.024 g) and azpy (0.2 mmol,0.009 g) was suspended in DEF/2-methoxy ethanol (1:1) mixture (10 mL) and heated to 120 °C for a period of 3 days. The resulting dark red crystals of **2** were then filtered and washed with DMF/ 2-methoxy ethanol for several times. Yield: 75%. Anal. Calc. for $C_{62}H_{58}Zn_3N_6O_{16:}$ C: 53.59; H: 3.81; N: 7.62; Found C: 53.53; H: 3.76; N: 7.60. FTIR (KBr pellet, 4000–400 cm^{-1}): 3240–3570(S), 3040(w), 1671(w), 1605(S), 1533(S), 1405(S).

3.2.7 Synthetic Procedure for Nanosphere (1N)

A mixture containing $Zn(OAc)_2\cdot 2H_2O$ (0.1 mmol, 0.022 g), bpdc (0.1 mmol, 0.024 g) and azpy (0.1 mmol,0.018 g) was suspended in DMF (10 mL) and heated to 80 °C for a period of 3 days. The dark red powder **1N** were then collected after washing with DMF for several times and air dried. Anal. Calc. for $C_{41}H_{35}Zn_2N_5O_{11}$: C: 53.76; H: 3.45; N: 7.21; Found C: 53.80; H: 3.47; N: 7.25. FTIR (KBr pellet, 4000–400 cm^{-1}): 3205–3580(S), 3060(w), 1654(m), 1590(S), 1536(m), 1397(S).

3.3 Results and Discussion

3.3.1 Crystal Structure Description of $\{Zn_2(bpdc)_2(azpy)]\cdot 2H_2O\cdot DMF\}_n$ (1) and $\{[Zn_3(bpdc)_3(azpy)]\cdot 2H_2O\cdot 2DEF\}_n$ (2)

Single crystal X-ray diffraction analysis suggests that **1** crystallizes in triclinic *P*$\bar{1}$ space group and has a two-fold interpenetrated 3D pillared-layer framework with *α*-Po topology. There are two Zn^{II} ions, two bpdc and one azpy ligand in the asymmetric unit. Two such Zn^{II} centres form a $\{Zn_2(COO)_4\}$ paddle-wheel type secondary building unit (SBU) which are linked through bpdc linkers and construct a square shaped 2D network along *ab* plane. Each five coordinated Zn^{II} is in a square pyramidal geometry and connected with four carboxylate O atoms [Zn–O 2.007(4)–2.061(4) A˚] from four bpdc linkers and one N atom [Zn–N 1.993(4)–2.018(3) A˚] from a azpy pillar. The 2D networks are further pillared by the azpy along *c* direction to generate an extended 3D framework The presence of long linkers results large cavities in the structure (7.9 × 8.4 $Å^2$) and undergoes self-catenation in the

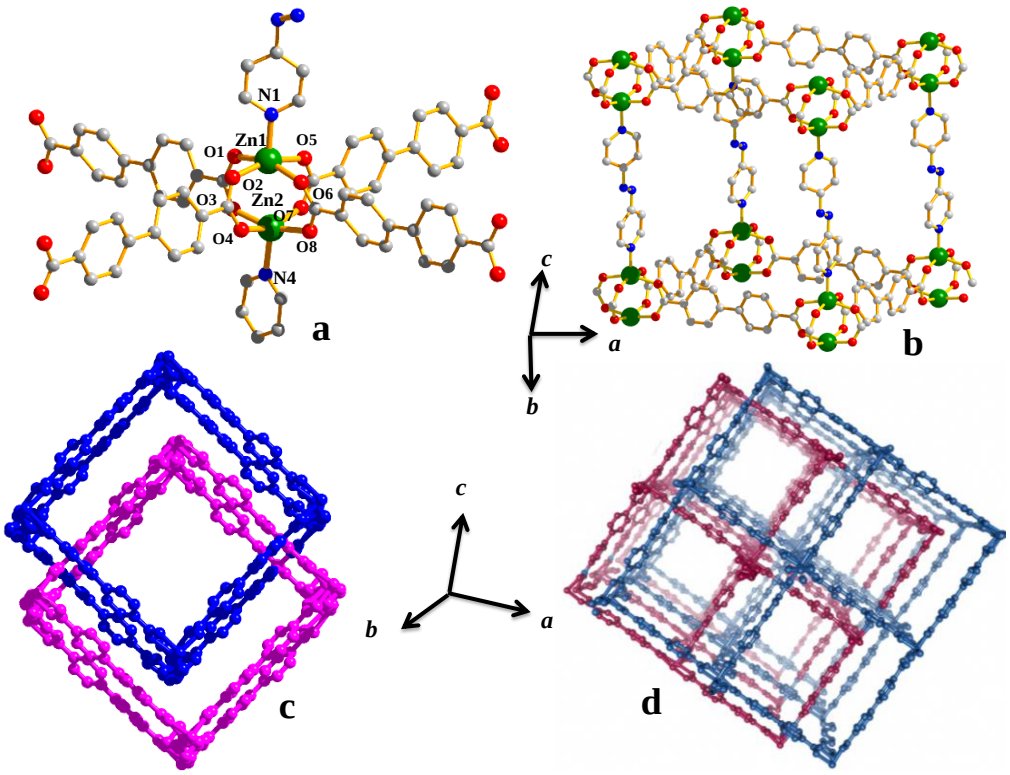

Fig. 1: a. Coordination environment of Zn in **1** b. Building unit of **1** c. Two fold interpenetrated nets of **1** d. Overall 3D structure along with pore view along *b* direction.

framework and the 3D channels are filled with guest DMF and water molecules. As a result of interpenetration, the pore volume and dimensions reduce significantly and these are of 4.2

× 6.9 Å^2, 3.5× 6.7 Å^2 and 7.2× 8.2 Å^2 along *a, b* and *c* direction respectively. Calculation using PLATON suggests the presence of void volume of ~ 1300 Å i.e. ~ 40 % of the total cell volume.Compound **2** is crystallized in monoclinic $P2_1/n$ space group and has a two-fold interpenetrated pillared-layer 3D framework. The structure of **2** possesses three crystallographically independent Zn^{II} centres (Zn1, Zn2, Zn3) which have been found to arrange as trinuclear metal cluster interconnected through μ_2-O2 and μ_2-O9. The asymmetric

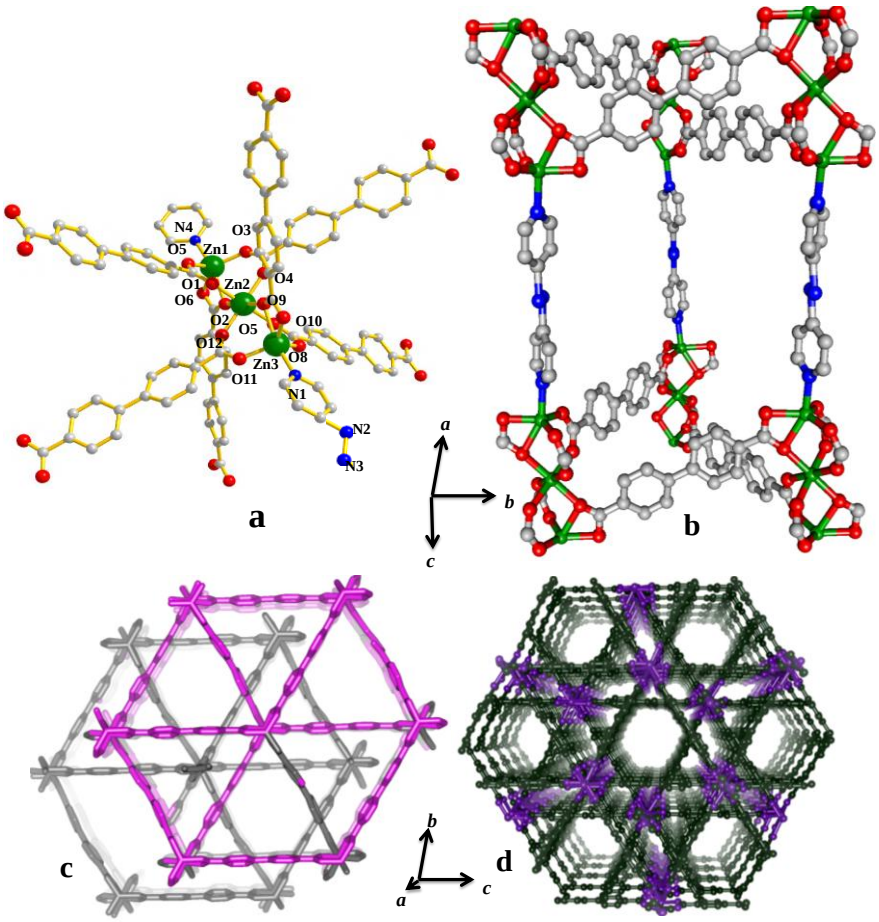

Fig. 2: a. Coordination environment of Zn in **2** b. Building unit of **2** c. Two fold interpenetrated nets of **2** d. Overall 3D structure along with pore view along *a* direction.

unit of **2** comprises of three crystallographically independent Zn^{II} centres (Zn1, Zn2 Zn3), three bpdc ligands and one azpy linker. In the framework, octahedral Zn2 is centred in the middle and are linked with six different carboxylate oxygens (O3, O4,O9, O10, O1,O12)), of bpdc whereas Zn1 and Zn3 are in distorted trigonal bipyramidal geometry, connected to four

carboxylate oxygen from three different bpdc and one nitrogen from azpy linker. The carboxylate oxygens, $\{\mu_2\text{-OCO}\}_2$ and (O2,O9) bridged the three Zn^{II} centres, resulting in trinuclear $\{Zn_3(\mu_2\text{-OCO})_2(COO)_4\}$SBU. Three such centres are connected through bpdc and forms triangular grid and these are being connected in alternate fashion and extended into 2D net along *ac* plane. Three Zn^{II} centres are connected by oxo or carboxylate bridges, resulting in a trinuclear $\{Zn_3(\mu_2\text{-OCO})_2(COO)_4\}$ SBU of the framework. These are interconnected through bpdc linkers, forming a triangular 2D net along *ac* plane. 2D net is further extended by azpy linker resulting in a 3D framework with cavity dimension of 11.9 × 11.2 $Å^2$. Similar to **1**, **2** also undergoes two-fold interpenetration due to presence of large void space. Unlike **1**, it possess a 1D channel (filled up with guest solvent molecules) along *a* direction with dimension of 7.3 × 7.1 $Å^2$. The Zn···Zn, Zn-O, Zn-O(μ_2) and Cd-N bond distances range as 3.983, 2.320(5)-2.549(5) Å, 2.381 Å and 2.340(7)-2.343(7) Å respectively. Calculation of void space using PLATON after removal of guest molecules suggests the presence of void volume of ~1496 Å i.e. 31 % of the total cell volume.

Table 1: Crystal data and structure refinement parameters of **1** and **2**

Parameters	**Compound 1**	**Compound 2**
Empirical formula	$C_{41}H_{35}Zn_2N_5O_{11}$	$C_{62}H_{58}Zn_3N_6O_{16}$
Formula weight	904	1338
Crystal system	Triclinic	Monoclinic
Space group	$P\bar{1}$	$P2_1/n$
a, Å	15.2090(4)	14.1046(5)
b, Å	15.2245(4)	19.9260(7)
, Å	15.8758(4)	25.9898(9)
α, deg	92.427(1)	90
β, deg	99.183(1)	90.005(1)
γ, deg	90.052(1)	90
V, $Å^3$	3625.55(16)	7304.4(4)
Z	2	4
T, K	180	180

μ, mm^{-1}	0.690	1.037
D_{calcd}, g/cm^3	0.729	1.172
F (000)	808	2408
Reflections[$I>2\sigma(I)$]	12187	8922
Total reflections	59824	72555
Unique reflections	19406	15030
λ(Mo-Kα)	0.71073	0.71073
R_{int}	0.0702	0.0784
GOF on F^2	1.09	1.09
R_w[all data]^b	0.2843	0.2888

Table 2. Selected bond lengths (Å) for **1**

Zn1-O2	2.025(3)	Zn1-O4	2.046(3)	Zn1-N1	2.033(3)	Zn1-O6_b	2.048(3)
Zn1-O8_f	2.039(3)	Zn2-O1	2.050(3)	Zn2-O3	2.017(3)	Zn2-O5_b	2.032(3)
Zn2-N4_d	2.038(3)	Zn2-O7_f	2.036(3)				

Table 3. Selected bond angles (°) for **1**

O2-Zn1-O4	88.49(12)	O2-Zn1-N1	102.52(13)
O2-Zn1-O6_b	88.38(12)	C30-N1-C31	117.7(4)
O2-Zn1-O8_f	161.14(13)	O4-Zn1-N1	99.02(12)
O4-Zn1-O6_b	157.70(16)	O4-Zn1-O8_f	88.55(12)
O6_b-Zn1-N1	103.22(16)	O8_f-Zn1-N1	96.34(12)
O6_b-Zn1-O8_f	87.32(13)	O1-Zn2-O3	87.87(12)
O1-Zn2-O5_b	87.65(15)	O1-Zn2-N4_d	99.46(16)
O1-Zn2-O7_f	158.20(13)	O3-Zn2-O5_b	161.65(13)
O3-Zn2-N4_d	99.86(16)	O3-Zn2-O7_f	88.73(12)

O5_b-Zn2-N4_d	98.42(16)	O5_b-Zn2-O7_f	88.85(16)
O7_f-Zn2-N4_d	102.33(16)		

Symmetry transformations used to generate equivalent atoms in **1**: b = x,-1+y,z, d = x,y,1+z, f = 1+x,y,z

Table 4. Selected bond lengths (Å) for **2**

Zn-O1	1.943(3)	Zn1-O006	1.943(3)
Zn1-O9	2.095(3)	Zn1-O10	2.219(3)
Zn1-N2	2.082(3)	Zn2-O2	2.042(3)
Zn2-O013	2.056(3)	Zn2-O10	2.138(3)
Zn2-O12_b	2.137(3)	Zn2-O3_i	2.056(3)
Zn2-O7_j	2.051(3)	Zn3-O11	2.091(3)
Zn3-O12	2.226(3)	Zn3-N1_d	2.065(3)
Zn3-O4_k	1.941(3)	Zn3-O8_l	1.950(3)

Table 5. Selected bond angles (º) for **2**

O1-Zn1-O006	120.32(12)	O7_j-Zn2-O12_b	92.26(11)
O1-Zn1-O9	113.54(13)	O3_i-Zn2-O7_j	92.28(11)
O1-Zn1-O10	97.21(11)	O11-Zn3-O12	59.36(11)
O1-Zn1-N2	95.11(13)	O11-Zn3-C65	29.83(12)
O1-Zn1-C42	107.07(12)	O11-Zn3-N1_d	94.88(14)
O006-Zn1-O9	123.64(13)	O4_k-Zn3-O11	123.11(13)
O006-Zn1-O10	97.21(11)	O8_l-Zn3-O11	114.11(13)
O006-Zn1-N2	96.35(13)	O12-Zn3-C65	29.55(12)
O006-Zn1-C42	113.35(12)	O12-Zn3-N1_d	154.14(14)
O9-Zn1-O10	59.64(11)	O4_k-Zn3-O12	97.19(11)

O9-Zn1-N2	94.22(14)	O8_l-Zn3-O12	97.57(11)
O9-Zn1-C42	30.09(12)	N1_d-Zn3-C65	124.70(15)
O10-Zn1-N2	153.81(14)	O4_k-Zn3-C65	113.25(12)
O10-Zn1-C42	29.56(12)	O8_l-Zn3-C65	107.44(12)
N2-Zn1-C42	124.31(15)	O4_k-Zn3-N1_d	95.58(13)
O2-Zn2-O013	92.56(11)	O8_l-Zn3-N1_d	95.23(13)
O2-Zn2-O10	92.05(11)	O4_k-Zn3-O8_l	120.30(12)
O2-Zn2-O12_b	89.56(11)	O2-Zn2-O3_i	178.99(11)
O2-Zn2-O7_j	87.65(11)	O013-Zn2-O10	89.54(11)
O013-Zn2-O12_b	88.72(11)	O013-Zn2-O3_i	87.54(11)
O013-Zn2-O7_j	179.00(11)	O10-Zn2-O12_b	177.68(11)

Symmetry transformations used to generate equivalent atoms in 2: b = 1+x,y,z, d = 1+x,1+y, z i = 1/2+x,1/2-y,-1/2+z, j = 1/2+x,1/2-y,1/2+z, l = 3/2+x,1/2-y,1/2+z

3.3.2 Thermal and PXRD Analysis

Thermogravimetric analysis (TGA) of **1** shows (Fig. 3) rapid initial mass loss of two bound guest water molecules in the temperature range of 80-85 °C (expt.,4% cald.,3.6%). The next consecutive steps exhibit release of one guest DMF molecules from the framework (expt., 8 cald., 7.5) in the temperature range of 103-155 °C. The desolvated **1′** is thermally stable up to 325 °C and then decomposes to an unidentified product. Similarly **2** shows (Fig. 3) first initial weight loss of two water molecule (expt.,8% cald.,7.2%) within 90 °C and in the next step loss of two DEF molecules (expt.,16% cald.,15.8%). The desolvated **2′** is thermally stable up to 345 °C and then decomposes.

1N follows similar trend with respect to **1** (Fig. 4)**,** first two water molecules within 90 °C (expt.,4% cald.,3.8%) and then one DMF within 160 °C (expt., 8% cald., 7.8%) with exact similar thermal stability upto 325 °C. This clearly indicates the **1N** is structurally closely similar to the bulk **1.**

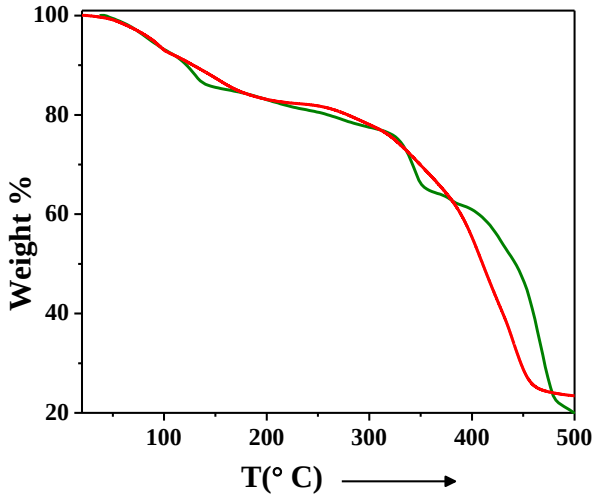

Fig. 3: TGA curves for **1** (black), **2** (red) in the temperature range 25−500 ºC

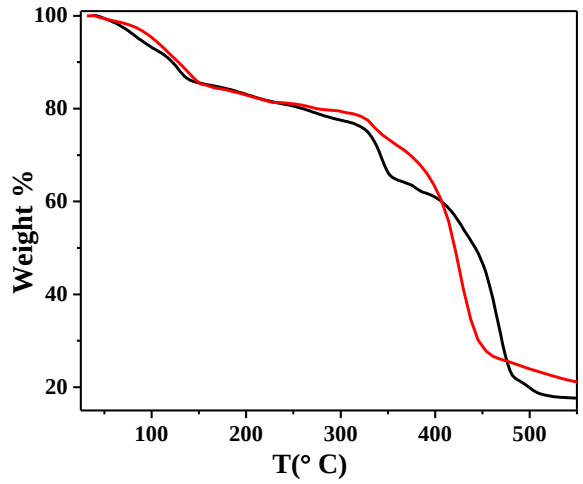

Fig. 4: (a) TGA curves for **1** (black), **1N** (red)

The PXRD patterns of **1** were recorded in different states and are shown in (Fig. 5 and 6). As-synthesised **1** shows sharp peaks, suggesting high crystallinity and well correspondence with the simulated pattern indicating high purity of the sample. Slight shifting of some of the peaks is probably due to desolvation (at room temperature) confirmed from change in crystal surface on keeping outside from the mother solution after some time. After complete removal of solvent molecules, the Bragg's diffractions get broadened; shift further along with regeneration of new peaks indicating poor crystallinity and structural transformation. On resolvation, **1′** shows clear regeneration of low angle diffraction peak and

almost well correspondent to the desolvated pattern indicating the flexible nature of the framework.

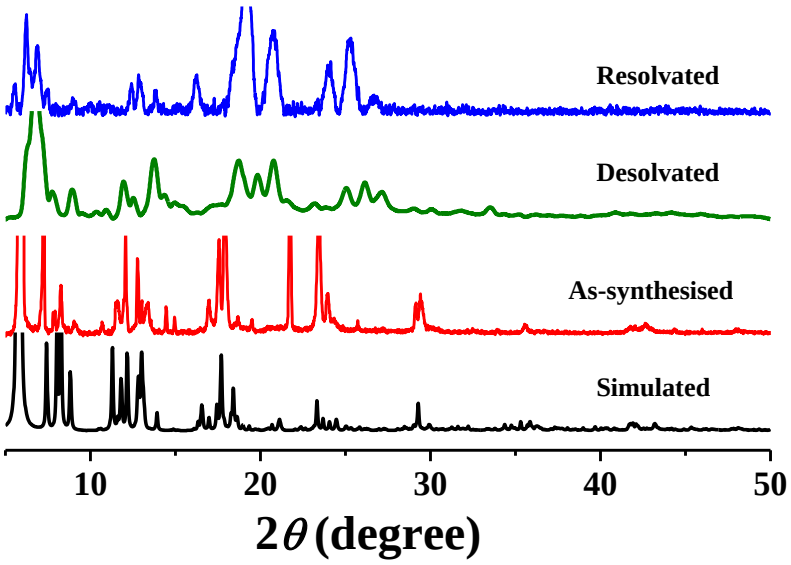

Fig. 5: PXRD of **1** recoded at different states

Same argument is also valid for **2** also. The as-synthesised pattern also shows presence of all

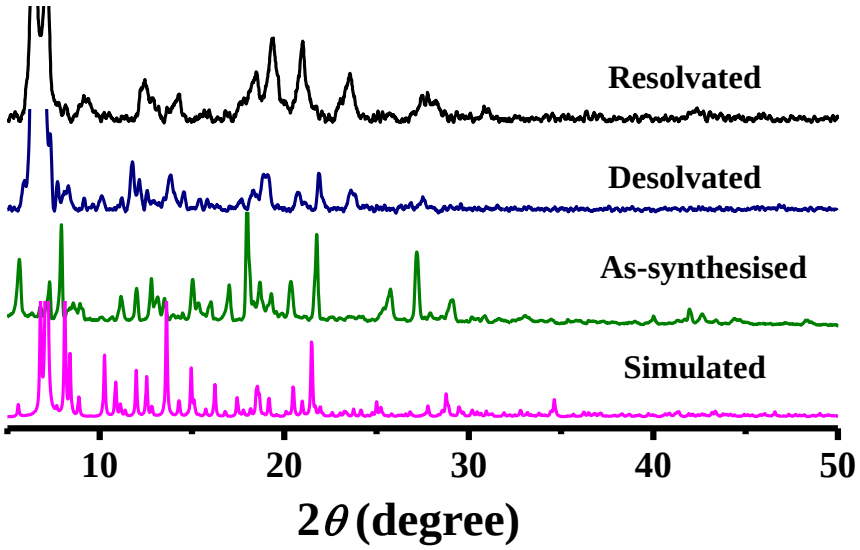

Fig. 6: PXRD of **2** recoded at different states.

peaks but among them some are very minutely shifted. This might be also due to partial desolvation at room temperature because this crystal also behaves in a similar manner as **1** on

keeping outside for some time. In desolvated **2′**, there is also presence of significant shifted and broadened peak and on resolvation it remains almost same but some of them are little shifted. The PXRD pattern clearly indicates this framework is also quite flexible in nature as **1**. PXRD (Fig. 7) of **1N** completely agree with **1** indicating their purity, similar phase and structural integrity at nanoscale. Noticeably, the broadening of the Bragg's reflections is observed, suggesting formation of smaller crystals with narrower size distribution compared to bulk **1.**

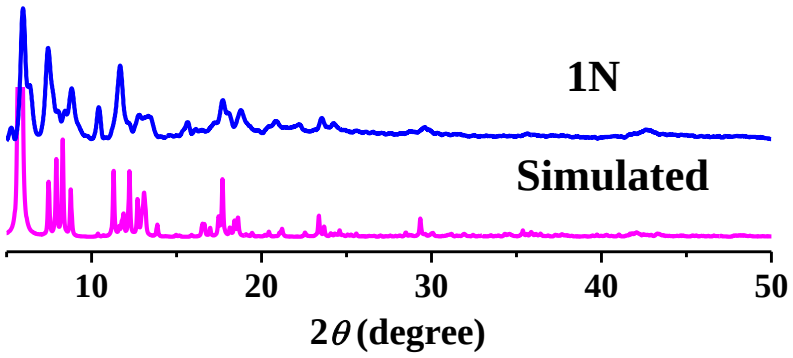

Fig. 7: PXRD of simulated and **1N**

3.3.3 Fabrication to Nanoscale (1N)

It has been possible to fabricate the bulk MOF **1** to nanoscale **(1N)** adopting well established coordination modulation (in solvothermal condition) method by acetate as modulator. Here the acetate source is $Zn(OAc)_2$ and two OAc^- ions are equivalent to two carboxylate groups in one bpdc linker. It is expected that, this monocarboxylate modulator would alter the coordination equilibrium at the crystal surface during the growth process due to competitive interactions with bpdc and the modulator. But the structural integrity will be preserved even after modulation. PXRD and TGA patterns of **1N** completely support this explanation. The morphology and the particle sizes of NMOFs were investigated by field emission scanning electron microscopy (FESEM) (Fig. 8). Here we have succeeded in controlling the crystal morphology from block shaped mm sized crystals to completely powdered spherical nanocrystals (**1N**). The average diameters of the spherical particles range within 500 ± 250 nm although the fine-tuning of the crystal size yet to be achieved.

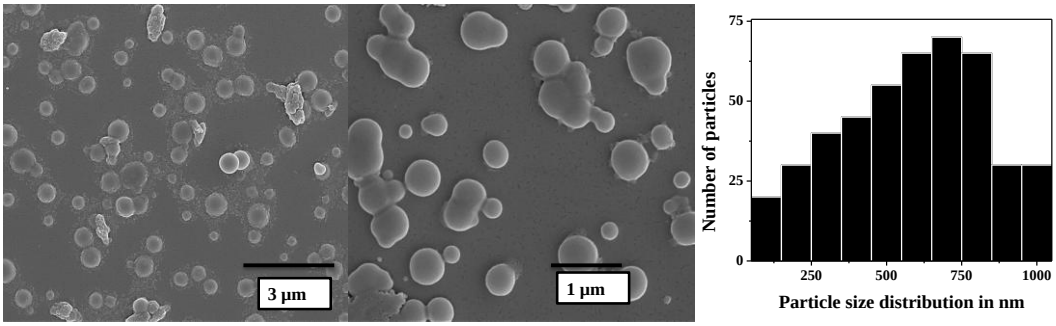

Fig. 8: FESEM images of nanospheres (**1N**) and particle size distribution

3.3.4 Adsorption Studies

To acquire more information about porous properties at bulk scale and nanoscale, N_2 and CO_2 sorption isotherms were recorded for **1′**, **1N′** and **2′** at 77 K and 195 K respectively. Despite of having sufficient pore size, **1′** and **2′** both show type II adsorption isotherm in case of N_2 (kinetic diameter 3.64 Å) at 77 K. Two probable reasons might be considered to this non-porous nature to N_2. The completely different diffraction patterns of PXRD in both cases **1′** and **2′**, clearly indicate structural transformation of the framework on desolvation of the framework. This structural change might have caused contraction of pores and probably the pore size is not sufficient enough to capture bigger N_2 molecules inside the pores. In other

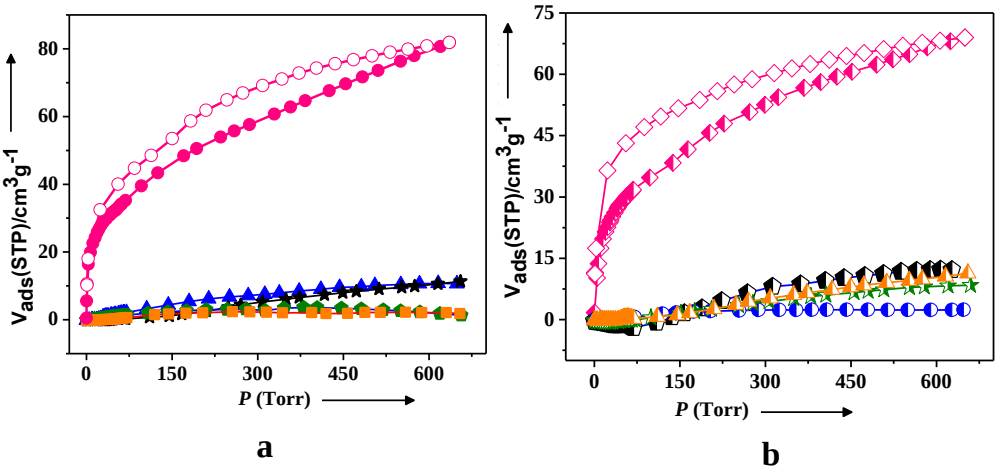

Fig. 9: Selectivity plot of CO_2 at 195 K (a) **1′** and (b) **2′** ; Pink: adsorption–desorption isotherms for **1′** and **2′** ; Orange: Ar; Black: N_2; Green: H_2 and Blue: O_2

way, it might be due to activated diffusion effects associated with the low thermal energy of the adsorbate relative to the high diffusion barrier.[29,30] But the measurements of CO_2 (kinetic diameter 3.4 Å) at 195 K (Fig. 9) for **1′** and **2′** up to 1 atm exhibit uptake amount of 16 wt% (81 cm^3 g^{-1} , 2.8 CO_2 per formula unit) and 13.5 wt% (69 cm^3 g^{-1} , 3.4 CO_2 per formula unit). The Langmuir and BET surface areas calculated from the CO_2 isotherms are ~ 251 and 235 m^2 g^{-1} for **1′** and ~ 214 and 200 m^2 g^{-1} for **2′** respectively. The single step type I isotherms are indicative of microporous nature of the both frameworks.

This indicates pore sizes in both cases are sufficient enough in order to accommodate CO_2 molecules. The hysteretic nature of desorption curves in both cases is due to strong interaction of the CO_2 molecules with the adsorption sites of the framework. The exclusion over other gases (N_2/Ar/O_2/H_2) at 195 K (Fig. 9) exhibits the selective nature of both **1′** and **2′** frameworks towards CO_2. The considerable affinity toward CO_2 in contrast to N_2/Ar/O_2/H_2 by both the compounds is probably because of the quadrupolar nature of the CO_2 molecule (quadrupole moment of CO_2: -1.4×10^{-39} Cm^2) and its strong interaction with the adsorptive sites (e.g. –N=N– and –COO) of the framework giving rise to selectivity. The strong interaction of CO_2 with **1′** and **2′** are also reflected in the high value of isosteric heat of adsorption values, $q_{st,\phi}$, ~ 32.8 and 31.5 kJmol^{-1} respectively as calculated from the Dubinin–Radushkevich [31] (DR) equation.

3.3.5 Solvent Vapour Adsorption Isotherms

To analyse the effect of solvent molecules on the pore surfaces of **1′** and **2′**, we have carried out solvent vapour adsorption study with different solvent molecules (H_2O, C_6H_6 at 298 K and MeOH at 293 K) with different polarities (Fig. 10). The **1′** shows similar double step adsorption profiles with polar H_2O (kinetic diameter, 2.65 Å) and MeOH (3.8 Å) but does not show any tendency for nonpolar benzene (5.8 Å) uptake. The H_2O sorption profile of **1′**, (Fig. 10a) first showed a gradual type I uptake up to P/P_0 = 0.46 (36 cm^3 g^{-1}) followed by stepwise uptake upto P/P_0 = 0.93 with a total adsorbed capacity of 103 cm^3 g^{-1} (3.6 H_2O molecule per formula unit). The pore is hydrophilic in nature because the step at low pressure i.e. at P/P_0 = 0.46 indicative of strong interaction of water molecules with the pore surface (possibly through hydrogen bonding).[33a] The desorption curve does not retrace the adsorption curve and shows hysteretic nature. The existence of threshold pressure at P/P_0 =

0.46 indicates that the adsorption process is blocked by diffusion barrier or weak host-guest interaction below that specific onset pressure. And this has been overcome by means of structural transformation for further accommodation of solvent molecules.[32] The MeOH sorption profile also supports its hydrophilic pore nature. In case of MeOH, the steep type I uptake is up to P/P_0 = 0.84 (52 cm^3 g^{-1}), then there is an almost linear increase with pressure in the second step leading to total uptake of 98 cm^3 g^{-1} (3.5 MeOH per formula unit). Since the polarity of the MeOH molecule is lesser than the water molecule, high pressure (P/P_0 = 0.84) might be needed in order to show stepwise uptake. The significant hysteretic nature and almost similar amount of uptake for both cases, water and MeOH, are definitely indicative of very strong polar pore surface of **1′**, otherwise lesser MeOH uptake would have been obtained. Both water and MeOH vapour adsorption isotherms directly point out toward the flexible nature of **1′.** All the profiles were analyzed by the DR equation and the values of βE_0, which reflect adsorbate-adsorbent affinity, are 5.00 kJ/mol for H_2O, 5.78 kJ/mol for MeOH for **1′.** Similar trend is also followed by **2′**, 4.91 kJ/mol H_2O and 5.75 kJ/mol for MeOH. This can be easily explained on the basis of two different parts of MeOH, hydrophobic (-CH_3) and hydrophilic (-OH). Probably the included MeOH molecules are oriented in pores in such a way that the -OH is certainly projected towards the polar part of the linkers whereas the -CH_3 is spacially accommodated near the non-polar part.[33b] The benzene being nonpolar could not interact with the pore surface and shows no inclusion.

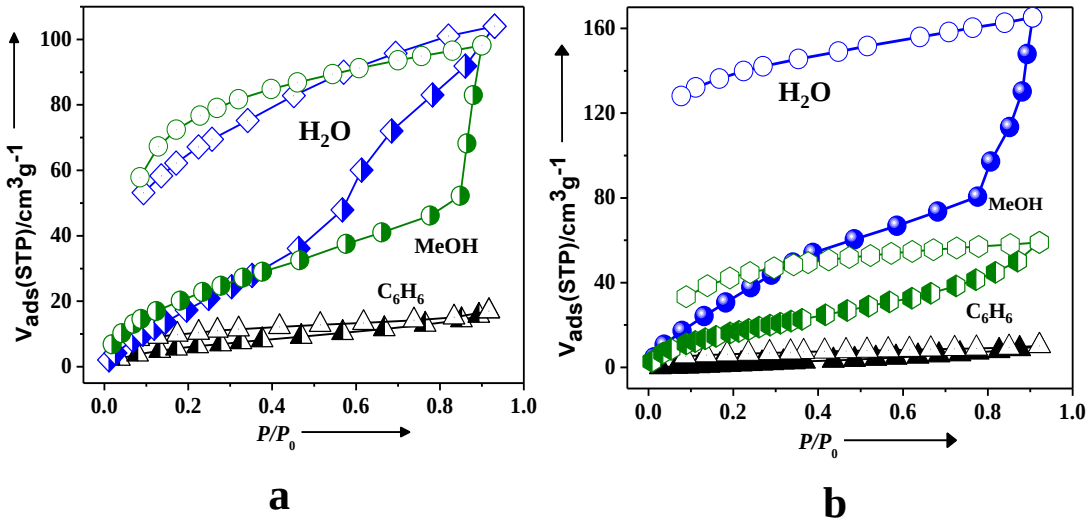

Fig. 10: Solvent vapour adsoption isotherms for (a) **1′** and (b) **2′**; H_2O at 298 K, MeOH at 293 K and C_6H_6 at 298 K.

In case of **2′** (Fig. 10b) water adsorption profile shows double step broad hysteretic profile. The first step is upto P/P_0 = 0.77 with an uptake of 80 cm^3 g^{-1} (4 H_2O molecules per formula unit) followed by stepwise rise and the final adsorbed amount is 165 cm^3 g^{-1} (8 H_2O molecules per formula unit). The broad hysteresis is due to strong interaction of water molecules with the adsorptive sites of the framework. This behaviour is clearly indicative of hydrophilic nature of the pore surface and also supports framework flexibility. MeOH being nonpolar, the interaction is not that much strong in order to cause structural transformation. Hence, the MeOH profile is type I in nature. The benzene is nonpolar and the framework do not show any trace of interaction with these molecules.

3.3.6 Gas Adsoption Studies of Nanosphere 1N

As expected, **1N** nanospheres show interesting sorption behaviour with respect to bulk **1**. Adsorption isotherm of N_2 of **1N′** at 77 K shows similar signature as bulk **1′** and this non-inclusion of adsorbate into **1N′** can be reasoned due to high diffusion barrier which is also evident in bulk **1′**. But the results obtained from CO_2 sorption isotherm (Fig. 11a) have been found to be slightly different, activated **1N** nanospheres show type I profile and the total

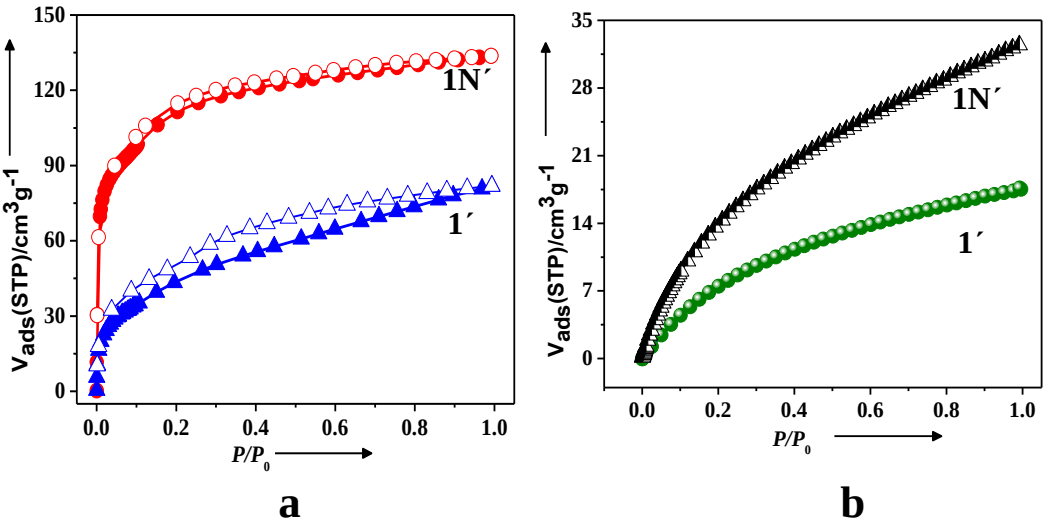

Fig. 10: (a) CO_2 adsorption isotherms at 195 K (b) CO_2 adsorption isotherm at 273 K

uptake is 26.2 wt% (133 cm^3 g^{-1} , 4.7 CO_2 per formula unit) whereas the bulk **1′** has been found to adsorb only 16 wt% (81 cm^3 g^{-1} , 2.8 CO_2 per formula unit) cm^3 g^{-1}. The Langmuir

and BET surface areas calculated from the CO_2 isotherm of **1N′** are 412, 385 m^2 g^{-1} respectively. Similar trend also has been followed by **1N** and **1** at 273 K (Fig. 11b), the uptake amounts are 6.2 wt% and 3.3 wt% (32 cm^3 g^{-1} and 17 cm^3 g^{-1}) respectively. The enhanced uptake in case of nanospheres can be explained on the basis of higher surface area and lesser diffusion barrier in nanoscale compared to bulk material. On decreasing size to nanorange, the specific surface area increases dramatically and in case of sphere, the surface area is inherently higher compared to other geometric shaped system with similar volume. The isosteric heat of adsorption (q_{st},ϕ) as calculated from by Dubinin-Radushkevich (DR) equation also supports this observation, for **1′**, it is 29.1 kJ mol^{-1} but for **1N′**, the value is 30.27 kJ mol^{-1} indicating stronger interaction with the pore surface in nanoscale.

3.3.7 Solvent Vapour Adsorption Isotherms of 1N′

In order to prove the proposed explanation of diffusion behaviour in nanoscale, solvent vapour adsorption has been carried for each case .The thermodynamic and kinetic approach, both have been studied into details. The solvent vapour adsorption isotherm of **1N′** (Fig. 12) nanosphere shows different sorption profiles compared to bulk. In case of water, it exhibits type I nature rather than stepwise manner with a total uptake of 129 cm^3 g^{-1} (4.6 H_2O per formula unit), higher than **1′**.

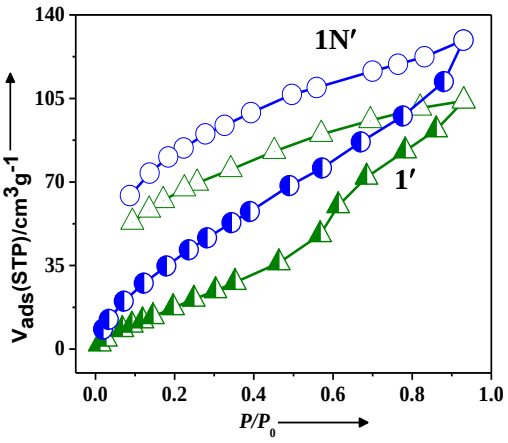

Fig. 12: Water vapour adsorption isotherms at 298 K

Since in nanocrystals, the diffusion barrier is significantly small compared to bulk, there was no necessity of structural transformation for accommodation of solvent molecules on increasing pressure. Generally for nanocrystal, the extent of adsorbed guest molecules per

unit volume i.e. adsorption capacity changes. βE_0 value calculated from Dubinin-Radushkevich (DR) equation shows almost similar adsorbate-adsorbent interactions 4.8 and 4.9 kJ mol^{-1} . Hence it can be anticipated that only diffusion barrier is playing crucial role for higher amount of uptake. But for flexible nanocrystals, size related effect on adsorption kinetics as well as on the activation energy required for transformation would be altered.[29] It might have so happened that guest induced phase transition behaviour (such as intermediate formation during measurement) could have been altered and changed depending upon the crystal size and morphology and the framework could not achieve that particular pressure in order to exhibit stepwise uptake.

3.3.8 Solvent Vapour Adsorption Kinetics of 1N′

The higher surface area and lesser diffusion barrier encouraged us to look and study this phenomenon in details from kinetic point of view. For convenience and considering instrumental set-up, solvent vapour adsorption kinetics with water has been carried out in order to compare the rate of diffusion of adsorbates in nanoscale.

Linear driving force (LDF),[30, 33-55] provide satisfactory descriptions in most cases of the adsorption kinetics of various gases/vapors on carbon molecular sieves and active carbons, depending on the adsorptive and experimental conditions. The LDF model is described by eq 1,

$$M_t/M_e = 1- \exp(-kt) \qquad (1)$$

Where M_t is the mass uptake at time t, M_e is the mass uptake at equilibrium, and k is the kinetic rate constant. The adsorption kinetics can be compared in terms of the rate constant (k) for the LDF model, which can be determined from either the gradient of the ln(1 - M_t/M_e) against time plot or by fitting the adsorption uptake curves to eq 1. Table 6 shows distinct differences between rate constants for **1** and **1N.** The rate constant gradually increases, reaches a maximum value and then starts to decrease for both cases. First, the rate of surface coverage increases and obtains highest value for monolayer formation followed by decreases with further coverage. Hence, the rate is always higher for **1N** than **1**, even at 16^{th} point there is tenfold increment and this is because of considerable decrease in diffusion barrier in nanospheres compared to bulk.

Temperature (K)	Step	$\underline{P/P_0}$	k (Kinetic rate constant) of **1N**	k (Kinetic rate constant) **1**
293	3	0.018774	4.45×10^{-3}	3.28×10^{-3}
	4	0.029246	5.23×10^{-3}	4.45×10^{-3}
	5	0.044187	6.26×10^{-3}	5.94×10^{-3}
	6	0.059388	6.85×10^{-3}	6.61×10^{-3}
	7	0.077649	7.77×10^{-3}	7.60×10^{-3}
	16	0.2914	1.20×10^{-2}	1.24×10^{-3}
	21	0.5578	1.31×10^{-2}	1.22×10^{-2}
	23	0.699	1.26×10^{-2}	1.15×10^{-2}
	24	0.7539	1.07×10^{-2}	1.06×10^{-2}
	26	0.8036	1×10^{-2}	9.65×10^{-3}
	29	0.9153	9.82×10^{-3}	9.31×10^{-3}

Table 6: Kinetic rate constant (k, sec^{-1}) values for **1′** and **1N′** at different points.

3.4 Conclusion

SBU directed two different 3D frameworks could have been possible to achieve from the identical struts but at two different conditions. One of these flexible frameworks, **1** has been fabricated to nanoscale **(1N)** through coordination modulation method (solvothermally) in order to study the effect of its flexible nature on adsorption of guest molecules from thermodynamic as well as kinetic point of view. **1N** shows 10 wt% increment in CO_2 storage behaviour could be attributed to a combined effect of nanocrystal size and smaller diffusion barrier in **1N** than bulk **1**. In order to prove, that kinetic measurements on water vapour has been carried out and shows higher rate of diffusion in **1N** due to higher surface area, completely supporting the given explanation. The further work of growth mechanism of the spherical nanocrystals and its effect on adsorption (from thermodynamic as well as kinetic point of view) are currently under investigation

3.5 References

1. *(a)* G. Férey, *Chem. Soc. Rev*., 2008, **37**, 191; *(b)* S. Kitagawa, R. Kitaura and S. I. Noro, *Angew. Chem., Int. Ed*., 2004, **43**, 2334; *(c)* T. K. Maji and S. Kitagawa, *Pure Appl. Chem.*, 2007, **79**, 2155; *(d)* T. K. Maji, R. Matsuda and S. Kitagawa, *Nat. Mater*., 2007, **6**, 142.

2. *(a)* H. K. Chae, M. Eddaoudi, J. Kim, S. I. Hauck, J. F. Hartwig, M. ÓKeeffe and O. M. Yaghi, *J. Am. Chem. Soc*., 2001, **123**, 11482; *(b)* M. Eddaoudi, D. B. Moler, H. L. Li, B. L. Chen, T. M. Reineke, M. ÓKeeffe and O. M. Yaghi, *Acc. Chem. Res*., 2001, **34**, 319; *(c)* L. Pan, B. Parker, X. Huang, D. H. Olson, J. Y. Lee and J. J. Li, *J. Am. Chem. Soc*., 2006, **128**, 4180; *(d)* R. Matsuda, R. Kitaura, S. Kitagawa, Y. Kubota, R. V. Belosludov, T. C. Kobayashi, H. Sakamoto, T. Chiba, M. Takata, Y. Kawazoe and Y. Mita, *Nature*, 2005, **436**, 238.

3. *(a)* P. Kanoo, R. Matsuda, M. Higuchi, S. Kitagawa and T. K. Maji, *Chem. Mater*., 2009, **21**, 5861; *(b)* P. Kanoo, K. L. Gurunatha and T. K. Maji, *J. Mater. Chem*., 2010, **20**, 1322; *(c)* S. Q. Ma, D. F. Sun, J. M. Simmons, C. D. Collier, D. Q. Yuan and H. C. Zhou, *J. Am. Chem. Soc*., 2008, **130**, 1012; *(d)* P. Kanoo, R. Matsuda, M. Higuchi, S. Kitagawa and T. K. Maji, *Chem. Mater*., Vol. 21, **24**, 2009

4. *(a)* H. K. Liu, W. Y. Sun, W. X. Tang, T. Yamamoto and N. Ueyama, *Inorg. Chem*., 1999, **38**, 6313

5. *(a)* J. Fan, W. Y. Sun, T. A. Okamura, J. Xie, W. X. Tang and N. Okamura, *New J. Chem*., 2002, **26**, 199; *(b)* A. N. Parvulescu, G. Marin, K. Suwinska, V. C. Kravtsov, M. Andruh, V. Parvulescu and V. I. J. Parvulescu, *J. Mater. Chem*., 2005, **15**, 4234.

6. *(a)* P. Horcazada, C. Serre, M. Sebban, F. Taulelle and G. Férey, *Angew. Chem., Int. Ed*., 2006, **45**, 5974; *(b)* P. Horcazada, C. Serre, G. Maurin, N. A. Ramsahye, F. Balas, M. Vallet-Regi, M. Sebban, F. Taulelle and G. Férey, *J. Am. Chem. Soc*., 2008, **130**, 6774.

7. *(a)* S. Henke, R. Schmidt and J. D. Grunwaldt, *Chem. Eur. J*., 2010, **16**, 14296; *(b)* Z. Q. Wang and S. M. Cohen, *J. Am. Chem. Soc*., 2009, **131**, 16675.

8. S. Diring, S. Furukawa, Y. Takashima, T. Tsuruoka and S. Kitagawa, *Chem. Mater*., 2010, **22**, 4531.

9. A. Carne, C. Carbonell, I. Imaz and D. Maspoch, *Chem. Soc. Rev.*, 2011, **40**, 291.

10. G. Fe´rey, and C. Serre, *Chem. Soc. Rev*., 2009, **38**, 1380.

11. D. Bradshaw, J. E Warren, and M. J. Rosseinsky, *Science*, 2007, **315**, 977.

12. M. P. Suh, and Y. E. Cheon, *Aust. J. Chem*. 2006, **59**, 605.

13. C. J. Kepert, *Chem. Commun*., 2006, **7**, 695.

14. A. J. Fletcher, K. M. Thomas, and M. J. Rosseinsky, *J. Solid State Chem*., 2005, **178**, 2491.

15. K. Uemura, R. Matsuda, and S. Kitagawa, *J. Solid State Chem*., 2005, **178**, 2420.

16. A. Kondo, H. Noguchi, L. Carlucci, D. M. Proserpio, G. Ciani, H. Kajiro, T. Ohba, H. Kanoh, K. Kaneko, *J. Am. Chem. Soc*., 2007, **129**, 12362.

17. P. L. Llewellyn, S. Bourrelly, C. Serre, Y. Filinchuk, and G. Fe´rey, *Angew. Chem. Int. Ed.*, 2006, **45**, 7751.

18. T. Uemura, Y. Hoshino, S. Kitagawa, K. Yoshida, and S. Isoda, *Chem. Mater*., 2006, **18**, 992.

19. P. Horcajada, C. Serre, D. Grosso, C. Boissière, S. Perruchas, C. Sanchez, G. Férey, *Adv. Mater.* 2009, **21**, 1931

20. O. K. Farha, A. M. Spokoyny, K. L. Mulfort, S. Galli, J. T. Hupp, and C. A. Mirkin, *Small*, 2009, **5**, 1727.

21. T. Tsuruoka, S. Furukawa, Y. Takashima, K. Yoshida, S. Isoda, and S. Kitagawa, *Angew. Chem. Int. Ed.* 2009, **48**, 4739.

22. *SMART (V 5.628), SAINT (V 6.45a), Xprep, SHELXTL*; Bruker AXS Inc. Madison, Wisconsin, USA, 2004.

23. G. M. Sheldrick, *Siemens Area Detector Absorption Correction Program*, University of Götingen, Götingen, Germany, 1994.

24. A. Altomare, G. Cascarano, C. Giacovazzo and A. Gualaradi, *J. Appl. Crystallogr*., 1993, **26**, 343.

25. G. M. Sheldrick, SHELXL-97, *Program for Crystal Structure Solution and Refinement*, University of Götingen, Götingen, Germany, 1997.

26. A. L. Spek, *J. Appl. Crystallogr*., 2003, **36**, 7.

27. G. M. Sheldrick, SHELXS 97, *Program for the Solution of Crystal Structure*, University of Götingen, Germany, 1997.

28. L. J. Farrugia, *J. Appl. Crystallogr*., 1999, **32**, 837

29. D. Tanaka1, A. Henke1, K. Albrecht1, M. Moeller1, K. Nakagawa, S. Kitagawa and J. Groll, *Nature*, 2010, **2**, 410.

30. A. J. Fletcher, E. J. Cussen, T. J. Prior, M. J. Rosseinsky, C. J. Kepert and K. Mark Thomas**,** *J. Am. Chem. Soc.*, 2001, **123**, 10001.

31. M. M. Dubinin, *Chem. Rev*., 1960, **60**, 235.

32. P. Kanoo, R. Matsuda, R. Kitaura, S. Kitagawa and T. K. Maji, *Inorg. Chem.*, 2012, **51**, 9141.

33. (*a*) C. R. Reid, I. P. O'koye, and K. M Thomas, *Langmuir* 1998, **14**, 2415 (*b*) K. L. Gurunatha and T. K. Maji, *Inorg. Chem*. 2009, 48, 10886.

34. C. R. Reid and K. M Thomas, *Langmuir* 1999, **15**, 3206.

35. A. W. Harding, N.J. Foley, P. R. Norman, D. C. Francis, K. M. Thomas, *Langmuir* 1998, **14**, 3858.

Chapter 4

Control of Interpenetration through Rational Choice of Strut Molecules and Adsorption Studies

Abstract

This chapter depicts a new strategy to control the interpenetration in MOFs by simple rational designing of organic building blocks based on dicarboxylate linkers acid. In general, it has been observed that, 3D framework with α-Po type topology (a simple pillared bilayer network connected through paddle-wheel SBU) undergoes interpenetration. Such as, $\{[Zn_2(bdc)_2(bpNDI)]\cdot 4DMF\}_n$ (**1**) [bdc = 1,4-benzenedicarboxylic acid; bpNDI = *N*,*N*′-dipyrid-4-yl-1,4,5,8-naphthalenediimide] framework is interpenetrated due to presence of 1,4- dicarboxylic acid (bdc) and long linker bpNDI. Replacing bdc by bulky 9,10-anthracenedicarboxylic acid (adc) (which acts as a strut-impenetrable scaffolds), successfully has led to achieve highly desired non-catenated materials $\{[Zn(adc)(bpNDI)_{0.5}]\cdot 2H_2O\cdot DMF\}_n$ (**2**) with higher void space in a controlled fashion. Adsorption studies [N_2 (77 K)/CO_2 (195 K)] proved that both of the frameworks are microporous in nature. Furthermore framework **1** shows double step CO_2 uptake at 195 K (upto 1 bar) and also at high pressure and different temperatures. This has been attributed to specific CO_2 and host framework interaction and this resulted into translational movement of networks. Strong interaction has been also realized by high isosteric heat of adsorption (35 kJ mol^{-1}) calculated from virial-type equation. This framework **1** has been also found to exhibit 0.69 wt% of H_2 storage capacity at 77 K with isosteric heat of adsorption of 6.7 kJ mol^{-1}. Moreover, Framework **2** has been found to exhibit interesting luminescence property. Additionally both of the frameworks are redox active due to highly electron deficient redox linker bpNDI and interestingly framework **2** shows fairly stabilized complete charge separated state through long range electron transfer from strut to strut.

4.1 Introduction

The recent upsurge of metal-organic frameworks (MOFs) or porous coordination polymers (PCPs) have been distinguished from other existing porous systems because of their ultralow densities, high surface area, modular nature of pore size and tunable pore functionality. Based on these, several advanced applications such as gas storage and separation, catalysis, sensing, ion exchange and drug delivery have been well studied.[1-7] In order to modulate the surface area, several aspects such as length, functional group, polarity of the constituting organic linkers have been considered as primary and crucial parameter to be varied.[8] However with increasing the length of the organic linker/ligand, the framework interpenetration becomes inevitable and it threats the permanent porosity of the overall framework. Although, recent results suggest that, interpenetration increases the thermal stability of the framework and this kind of flexible frameworks show interesting guest responsive structural transformation by means of translational movements of networks. Several interesting applications have been reported based on these structural characteristics of interpenetrated framework [14] such as these materials have been found to be good adsorbent for small molecules for example carbon dioxide and especially for hydrogen.[9] But most of the time 2, 3, 4, 5 and even higher degree of catenation have been routinely encountered in MOF and resulting to non-porous behaviour. Achieving a single network (non- catenated) is the soul route to the highest porosity and thus control over interpenetration in a MOF system is of paramount importance for practical applications. For suppressing the degee of catenation, several synthetic strategies have been adopted such as high degree of dilution (for IRMOFs) [10], applying 'liquid-phase epitaxy' on an organic template [11], employing a step by step growth method [12] and rational designing of tetratopic ligand [13]. But those techniques cannot be generalised in terms of avoiding catenation. Additionally some are restricted to surface-related applications only.

It has been realised that, in α-polonium type structures, paddle wheel SBUs $\{M_2(COO)_4\}$ are connected through dicarboxylate units, extending to 2D square grid kind of network followed by pillaring of N-ligand to the lattice points perpendicular to the 2D layer and undergoes interpenetration. We have envisioned that, if it is possible to rationally increase the width of the dicarboxylate ligand in such a way that, the available free space in

2D layer effectively can be minimised and it would not certainly stop spontaneous self-catenation.

1,4,5,8-naphthalenediimide (NDI) has been found to be potentially effective for designing of optoelectronic active materials. It has attracted much attention due to their tendency to form *n*-type over *p*-type semiconductor materials. The naphthalenediimides are rigid, planar and electron deficient aromatic compounds capable of being self-organised in different solvent systems and can be intercalated into larger multicomponent assemblies [(14)]. N-based long linker bpNDI (*N*,*N*′-di(4-pyridyl)-1,4,5,8-naphthalenediimide) has been first introduced in MOFs by Hupp *et al.* [(15)] to tune the channel dimension and internal surface area. Later, it has been further explored by this same group along with tetratopic tetracarboxilic ligand [(13)] in order to control interpenetration as well as surface area. Work has been further progressed by Kitagawa *et al.* for exploring its photoactive property. [(14 c)]

We have realized that it would be a worthy effort to design and construct a redox active non-interpenetrated framework with a long linker bpNDI for exploration further the properties in a better way. To realize our conjecture we have targeted a well-known framework $\{[Zn_2(bdc)_2(bpNDI)]\cdot 4DMF\}_n$ (**1**) reported by Kitagawa *et al*. It is a pillared-layer, two-fold interpenetrated, porous framework and has shown interesting photophysical property. We have rationalised that, the use of simple diatopic carboxylic ligand anthracene based dicarboxylic linker (bulky enough compared to benzene) could be effective in order to resist catenation (Scheme 1) even in presence of long linker bpNDI. Hence, the free space in 2D layer would not be available in this case and could be efficient enough to control entanglement. Here we have synthesized a novel, non-interpenetrated pillared layer paddle wheel luminescent framework $\{[Zn(adc)(bpNDI)_{0.5}]\cdot 2H_2O\cdot DMF\}_n$ (**2**) [adc = 9,10-anthrcenedicarboxylic acid]. This can be credited to the steric effect of extra benzene rings (attached with bdc core part) which are occupying most of the available free spaces in 2D layer and results into non-interpenetration. The void space calculation shows 43.4 % void space for **1** whereas **2** exhibits 58 %. CO_2 adsorption studies on **1**, show double step hysteretic adsorption isotherms for CO_2 indicating structural transformation on guest inclusion, which is the characteristic behaviour for interpenetrated framework. But **2** exhibits only type I uptake supporting its non-interpenetrated framework nature. Although interpenetration could have been controlled successfully but the gas storage capacity has been reduced significantly due to effective blocking of pore window by bulky bpNDI. But this

method, however, can be generalised for potential non-interpenetrated frameworks consisting of anthracene core unit. Photophysical studies of **2** show its luminescent nature and additionally long range one electron transfer from donor adc unit to acceptor bpNDI moiety through coordination bonding via metal centres.

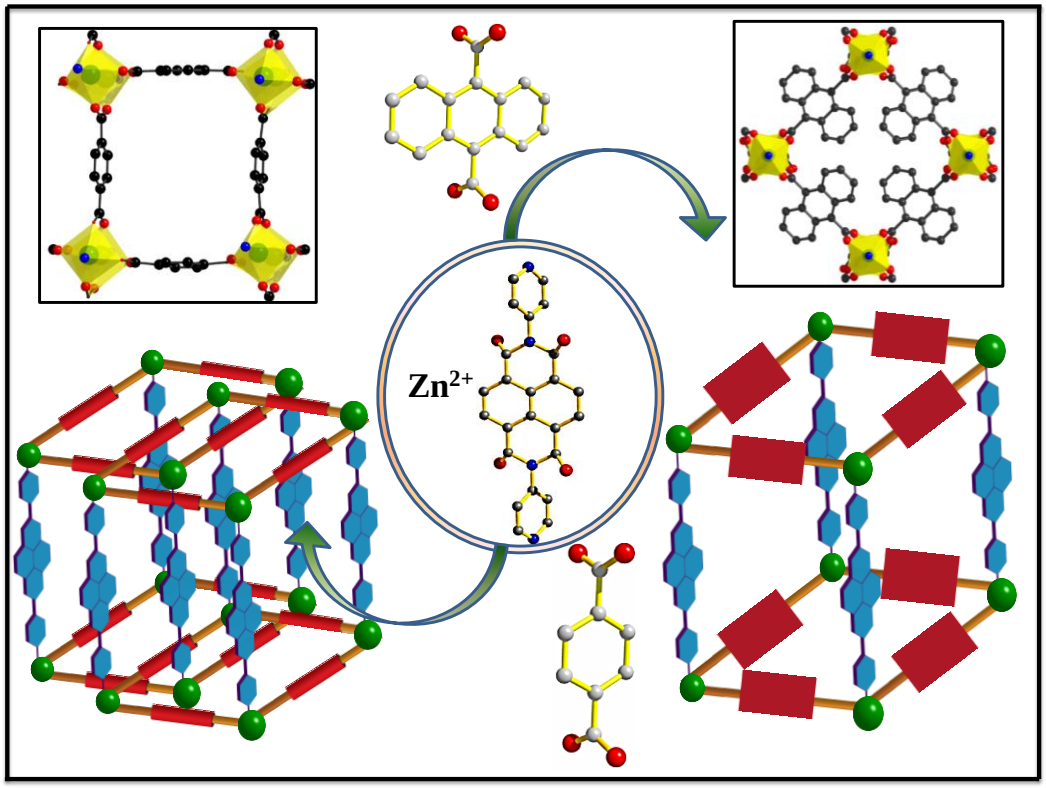

Scheme 1: Schematic view of control of interpenetration

4.2 Experimental Section

4.2.1 Materials

All the reagents employed were commercially available and used as provided without further purification. Metal salt was obtained from Spectrochem. 1,4-benzenedicarboxylic acid, 9,10-anthracenedicarboxylic acid were obtained from Sigma Aldrich chemicals. *N*,*N*′-di(4-pyridyl)-1,4,5,8-naphthalenediimide was synthesised following the literature procedure [16].

4.2.2 Physical Measurements

Elemental analysis was carried out using a Thermo Fischer Flash 2000 ElementalAnalyzer. Thermogravimetric analysis (TGA) was carried out (MetlerToledo) in nitrogen atmosphere (flow rate = 50 mL min^{-1}) in the temperature range 30–500 °C (heating rate 3 °C min^{-1}). Powder XRD pattern of the products were recorded by using Mo-Kα radiation (Bruker D8 Discover; 40 kV, 30 mA).The pattern was agreed with those calculated from single crystal structure determination. Electronic absorption spectra were recorded on a Perkin Elmer Lambda 900 UV-VIS-NIR Spectrometer and emission spectra were recorded on Perkin Elmer Ls 55 Luminescence Spectrometer.

4.2.3 X-Ray Crystallography

X-Ray single-crystal structural data of **2** was collected on a Bruker Smart-CCD diffractometer equipped with a normal focus, 2.4 kW sealed tube X-ray source with graphite sprogram SAINT [17] was used for integration of diffraction profiles and absorption correction was made with SADABS [18] program. All the structures were solved by SIR92 [19] and refined by full-matrix least-squares method using SHELXL-97.[20] All the hydrogen atoms were geometrically fixed and placed in ideal positions. Potential solvent accessible area or void space was calculated using the PLATON multipurpose crystallographic software.[21] All crystallographic and structure refinement data of **1** are summarized in Table 1. Selected bond lengths and angles for **1**, are given in Table 2 and 3, respectively. All calculations were carried out using SHELXL 97, [20] PLATON, [21] SHELXS 97 [22] and WinGX system, Ver 1.70.01.[23]

4.2.4 Adsorption Study

The adsorption isotherms of CO_2, H_2, N_2, CH_4 using the dehydrated **1** (**1′**) and **2** (**2′**) were measured by using a QUANTACHROME QUADRASORB-SI and AUTOSORB-*iQ2* analyzer. **1′** has been prepared by heating at 140 °C under a 1×10^{-1} Pa vacuum for about 10 h prior to measurement of the isotherms. . **2′** was prepared by heating at 200 °C under the same conditions. Helium gas (99.999% purity) at a certain pressure was introduced in the gas chamber and allowed to diffuse into the sample chamber by opening the valve. The amount of gas adsorbed was calculated readily from pressure difference (P_{calc}- P_e), where P_{calc} is the

calculated pressure with no gas adsorption and P_e is the observed equilibrium pressure. All operations were computer-controlled and automatic.

High-pressure CO_2 (273, 283 and 298 K), H_2 (77 K) and CH_4 (273 and 298 K) sorption measurements were carried out on a fully computer controlled volumetric BELSORP-HP, BEL Japan high pressure instrument. All the gases used for the high pressure measurements are scientific/research grade with 99.999% purity. For the measurements, an approximately 300 mg sample was taken in a stainless-steel sample holder and degassed at 200 °C for a period of 18 h under 10^{-1} Pa vacuum. Dead volume of the sample cell was measured with helium gas of 99.999% purity. Non ideal correction for each gas was made by applying virial coefficients at the respective measurement temperature.

4.2.5 Synthesis of $\{[Zn_2(bdc)_2(bpNDI)]\cdot 4DMF\}_n$ (1)

The crystals (**1**) have been synthesized following the literature [14 c)] procedure and have been characterized through TGA, PXRD, (Fig. 2 a,b) and elemental analysis. Anal. Calc. for $Zn_2C_{52}O_{17}H_{48}N_8$: C: 53.43; H: 3.76; N: 9.59; Found C: 53.40; H: 3.729; N: 9.53. FTIR (KBr pellet, 4000–400 cm^{-1}): 3052(m), 1690(m), 1605(S), 1520(m), 1390(S).

4.2.6 Synthesis of $\{[Zn(adc)(bpNDI)_{0.5}]\cdot 2H_2O\cdot DMF\}_n$ (2)

A mixture containing $Zn(NO_3)_2\cdot 6H_2O$ (0.1 mmol), adc (0.1 mmol) and bpNDI (0.05mmol) was suspended in DMF (8 ml) and heated to 120 °C for a period of 3 days. The brown yellow crystals (**2**) were then collected after washing with DMF for several times. **2**: Yield: 80%. Anal. Calc. for $C_{31}H_{17}ZnN_3O_7$: C: 53.59; H: 3.81; N: 7.62; Found C: 53.53; H: 3.76; N: 7.60. FTIR (KBr pellet, 4000–400 cm^{-1}): 3250–3580(S), 3042(w), 1661(w), 1602(S), 1515(m), 1391(S).

4.3 Results and Discussion

4.3.1Crystal Structure Description of $\{[Zn_2(bdc)_2(bpNDI)_{0.5}]\cdot 4DMF\}_n$ (1)

X-ray single crystal structure determination reveals that **1** is crystallized in tetragonal *C*2/*c* space group. It is a pillared-layer, two-fold interpenetrated, porous structure with paddle-wheel SBU. The paddle-wheel cores $\{Zn_2(COO)_4\}$ are connected through bdc linkers

along *c*-direction and forms 2D layer. These 2D networks are further connected with dipyridyls and extended to a 3D framewowk with a primitive cubic topology. Finally interpenetration occurs because of available free space in 2D layer and accommodates more nets.

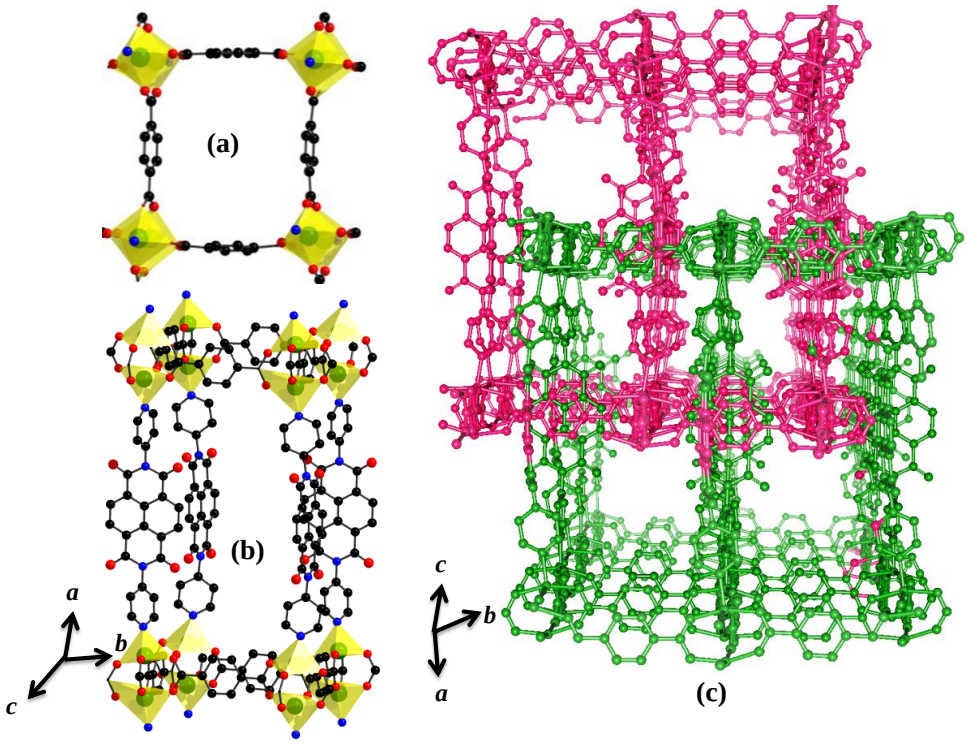

Fig. 1: (a) Top view of building unit along *a* direction (2D layer) of **1** (b) Building unit of **1** (c) 2-Fold interpenetration of **1.**

4.3.2 Crystal Structure Description of $\{[Zn(adc)(bpNDI)_{0.5}]\cdot 2H_2O\cdot DMF\}_n$ (2)

X-ray single crystal structure determination reveals that **2** is crystallized in tetragonal *I*4/*mcm* space group. It has non-catenated pillared layer 3D framework and exhibits α-Po type network topology. In 3D framework, each Zn^{II} ion is five-coordinated with four carboxylate O atoms [O1] from four adc linkers and one N atom [N1] from one bpNDI ligand in a square-pyramidal geometry. Zn^{II} centers are further bridged by same four dicarboxylate units leading to a paddle-wheel dinuclear $\{Zn_2(COO)_4\}$ SBU. Further, these paddle wheels are mutually interconnected through adc and extended into 2D net along *ab* plane. This 2D layers are further pillared by the bpNDI linkers through pyridyl coordination-N along *c* direction to generate an elongated 3D tetragonal framework. It shows bidirectional channel and the

corresponding channel size is 3.13×4.35 $Å^2$ (along *a* and *b* direction). The Zn···Zn separation distance and Zn-O and Zn-N bond distances range as 2.920(4), 2.029(5) and 1.988(7) Å respectively. The presence of adc linkers sterically block the available free space along *c* direction and self-catenation could have been avoided controlled successfully. Calculation of solvent accessible void space, using PLATON after removal of guest molecules suggests the presence of void volume of ~ 4570.0 $Å^3$ i.e. 58 % of the total cell volume.

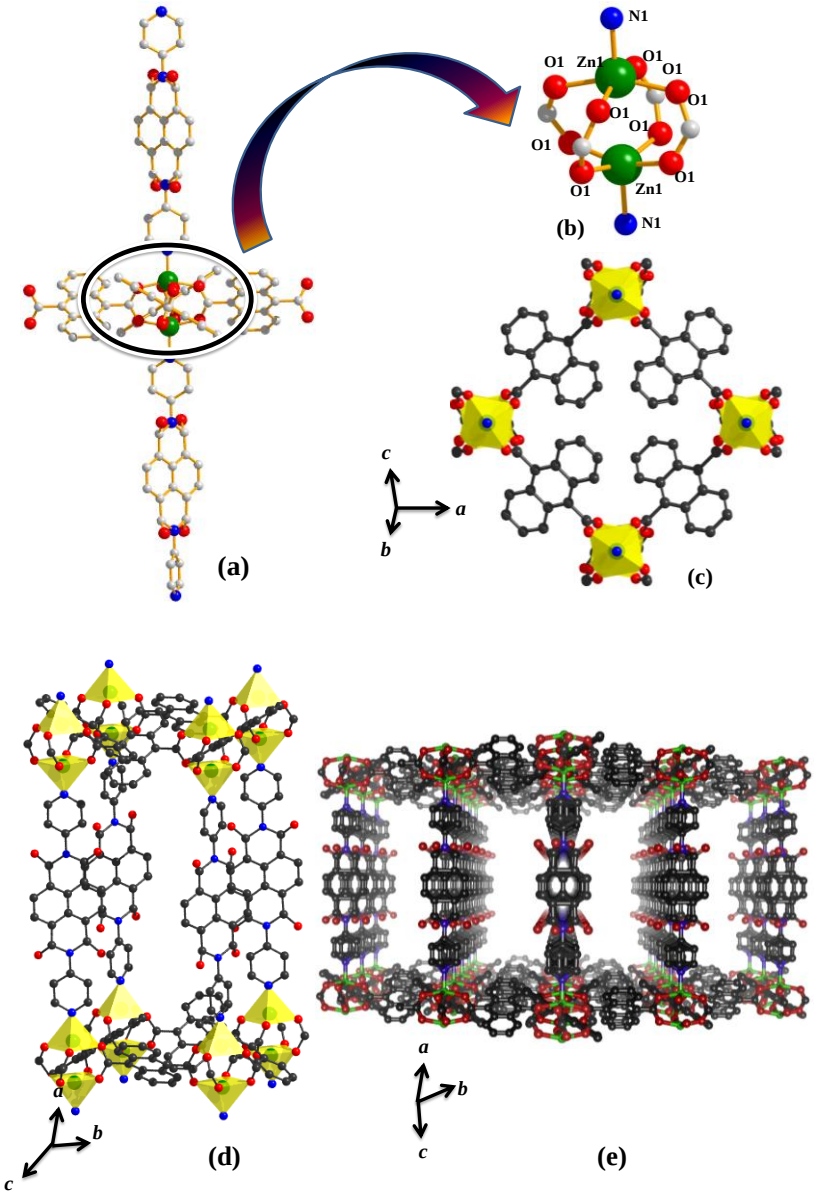

Fig. 2: (a) View of coordination environment of Zn^{II} in **2** (b) Closer view of coordination environment of Zn^{II} (c) Top view of building unit along *b* direction (d) Building unit of **2** (e) Overall pore view of the structure along *c* direction.

Table 1: Crystal data and structure refinement parameters

Parameters	**2**
Empirical formula	$C_{31}H_{17}ZnN_3O_7$
Formula weight	642.7
Crystal system	Tetragonal
Space group	*I*4/*mcm*
a, Å	15.259(5)
b, Å	15.259(5)
c, Å	44.489(5)
α, deg	90
β, deg	90
γ, deg	90
V, Å^3	10359(7)
Z	8
T, K	100
μ, mm^{-1}	0.496
D_{calcd}, g/cm^3	0.684
F (000)	2144
Reflections[$I>2\sigma(I)$]	5250
Total reflections	40241
Unique reflections	8422
λ(Mo-Kα)	0.71073
R_{int}	0.102
GOF on F^2	0.94
$R_1[I>2\sigma(I)]^a$	0.0625
R_w[all data]^b	0.1739

Table 2. Selected bond lengths (Å) for **2**

Zn1-O2	2.030(5)	Zn1-O2_a	2.030(5)	Zn1-N1	1.988(9)

The CO_2 adsorption isotherm at 195 K, measured up to 1 atm, exhibited a double-step profile (Fig. 4 b) with a significant stepwise hysteretic desorption curve. In the first step, **1′** shows initial steep uptake of 12.3 wt% at a very low pressure (P/P_0 = 0.0095), then it gets saturated and exhibits type I nature with storage capacity of 17.5 wt% (89 cm^3 g^{-1}, 1.7 CO_2 molecule per formula unit). In the next step, at P/P_0 = 0.40264, there is an abrupt jump indicating guest induced structural transformation on increasing external pressure. After P/P_0 = 0.60715, the curve is gradually saturated with a total storage capacity of 45.3 wt% CO_2 (231 cm^3 g^{-1}, 4.5 molecule per formula unit). The desorption isotherm does not exhibit steps at those corresponding inflection points and hence does not retrace the adsorption process at all. The first and the second inflection points in the desorption curve are at P/P_0 = 0.0044 and 0.195 respectively and certainly these are not coinciding with the corresponding points in adsorption plot except in the very low pressure region. This significant deviation with marked broad hysteresis loops strongly confirms that the adsorbed CO_2 is not immediately released on reducing the external pressure and is thus quite firmly trapped within the framework at very low pressures.

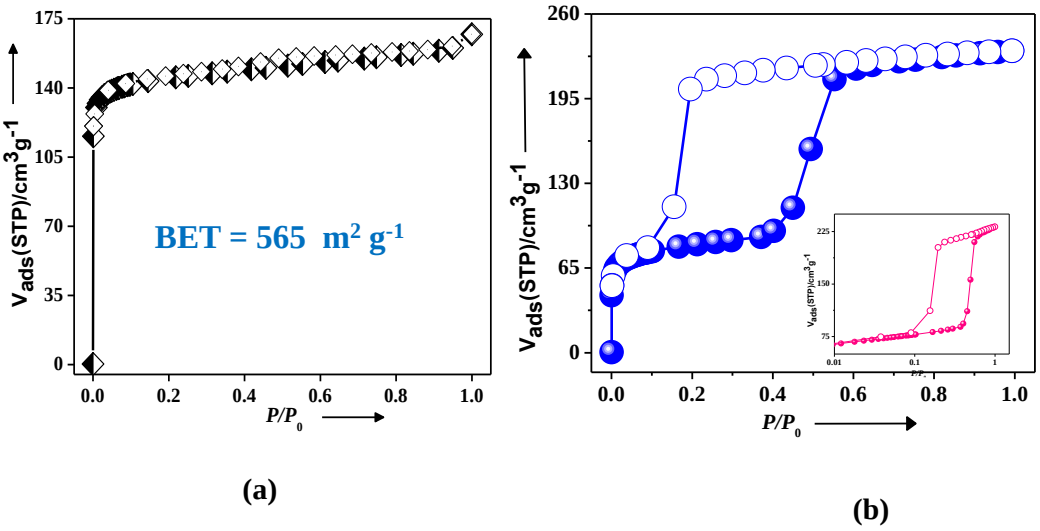

Fig. 4: (a) N_2 adsorption isotherm at 77 K of 1′ (b) CO_2 adsorption isotherms for **1′** (In inset the plot of 195 K in log scale).

This quite good amount of uptake prompted us to measure the CO_2 storage capacity at 293 and 273 K. For both temperatures, the profiles are type I in nature and it indicates that at higher temperatures, the pressure is not sufficient enough to cause translational movement of

networks. At 293 and 273 K, the CO_2 uptake amounts are 8.4 wt% (43 cm^3 g^{-1}, 0.84 molecule per formula unit) and 9.4 wt% (48 cm^3 g^{-1} , 0.94 ~1 CO_2 molecule per formula unit). To extract the coverage-dependent isosteric heat of adsorption, the data were modelled with a virial-type expression composed of parameters a_i and b_i that are independent of temperature.[24]

$$\ln P = \ln N + 1/T \sum_{i=0}^{m} a_i N^i + \sum_{i=0}^{n} b_i N^i \quad \text{.....(1)}$$

$$Q_{st} = -R \sum_{i=0}^{m} a_i N^i \quad \text{.....(2)}$$

Here, P is the pressure expressed in Torr, N is the amount adsorbed in mmol g^{-1}, T is the temperature in K, a_i and b_i are virial coefficients, and m, n represents the number of coefficients. The isosteric heat of adsorption has been found to be 35 kJ mol^{-1} indicating significant strong binding with the adsorptive sites of the framework (such as pending = CO, carboxylate O atoms, N atoms and also aromatic π-cloud).

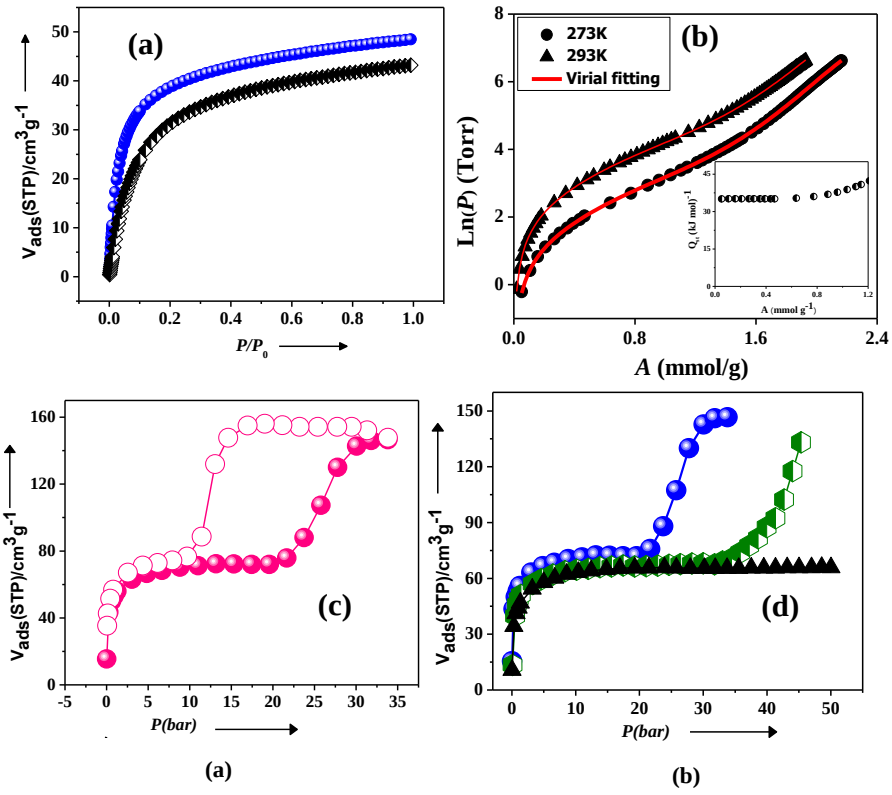

Fig. 5: (a) CO_2 adsorption isotherms of **1′** : Black : 273 K and Blue : 293 K (b) Fitted curves through

virial type expression showing corresponding Q_{st} value (in inset) (c) CO_2 adsorption-desorption isotherm of **1′** at 273 K and 33 bar (d) CO_2 adsorption isotherms of **1′**; Blue: at 273K and 33 bar ; Green: at 283 K, 46 bar and Black: 298 K and 52 bar.

High Pressure CO_2 measurement at 273 K (P = 33 bar) exhibited similar double step adsorption (Fig. 5 c) characteristics with large hysteretic desorption loop. Here also, the curve begins with similar steep initial uptake followed by saturation with total storage capacity of 29.0 wt%. At 283 K (P = 46 bar), it also showed double step signature with an uptake amount of 26.1 wt% (133 $cm^3\ g^{-1}$) but the second inflection point has been moved to higher pressure (P = 33.3 bar) compared to adsorption curve obtained in 273 K . Increase in temperature to 298 K (P = 52 bar) completely removed steps and showed purely type I nature with 12.9 wt% (65.8 $cm^3\ g^{-1}$) storage capacity. Desorption curves measured at 283 and 293 K could not have been achieved due to the condensation problem of CO_2 at higher pressure but it has been possible to obtain the adsorption curves (Fig. 5 d). It has been observed that there is significant shrinkage of the framework **1** on removal of guest DMF molecules (**1′**) and also drastic reduction in solvent accessible void space from 43.4% to 27.6%. Now **1′** with shrunken pores on adsorption of CO_2 molecules might have expanded the pore volume at a particular pressure and is being responsible for phase change with dynamic stepped adsorption.

This compound also proves to be a good adsorbent for H_2 storage. The H_2 gas adsorption isotherms of **1′** at 77 K and 87 K show 0.68 wt%, (77 $cm^3\ g^{-1}$) and 0.58 wt% (65 $cm^3\ g^{-1}$) and storage capacity. A virial type expression (equation 1) has been fitted to 77 K and 87 K and the coverage-dependent isosteric heat of adsorption has been calculated and it is found to be to be 6.7 kJ mol^{-1} (Fig. 6(b)). However, at 77 K and high pressures (P = 52 bar), **1′** adsorbs up to 1.25 wt% H_2 (140 $cm^3\ g^{-1}$) (Fig. 6(b)).

Whereas in case of CH_4, it shows 4.13 wt% of CH_4 (58 $cm^3\ g^{-1}$) uptake at 273 K and 3.55 wt% (50 $cm^3\ g^{-1}$) at 298 K under pressure of 45 bar with type I nature (Fig. 6 c) . Considering the kinetic diameters and the polarities of the adsorbates such as H_2 (kinetic diameter = 2.89Å, no dipole moment), CO_2 (kinetic diameter = 3.3 Å, quadrupole moment = 4.30×10^{26} esu cm^{-2}), N_2 (kinetic diameter = 3.6 Å, quadrupole moment = 1.52×10^{26} esu cm^{-2}) and CH_4 (kinetic diameter = 3.8 Å), it can be explained that here not only the size but also the polarity of the adsorbate molecules, onset pressure all are playing crucial role for gate opening behaviour of the framework through pore expansion and movement of the networks.

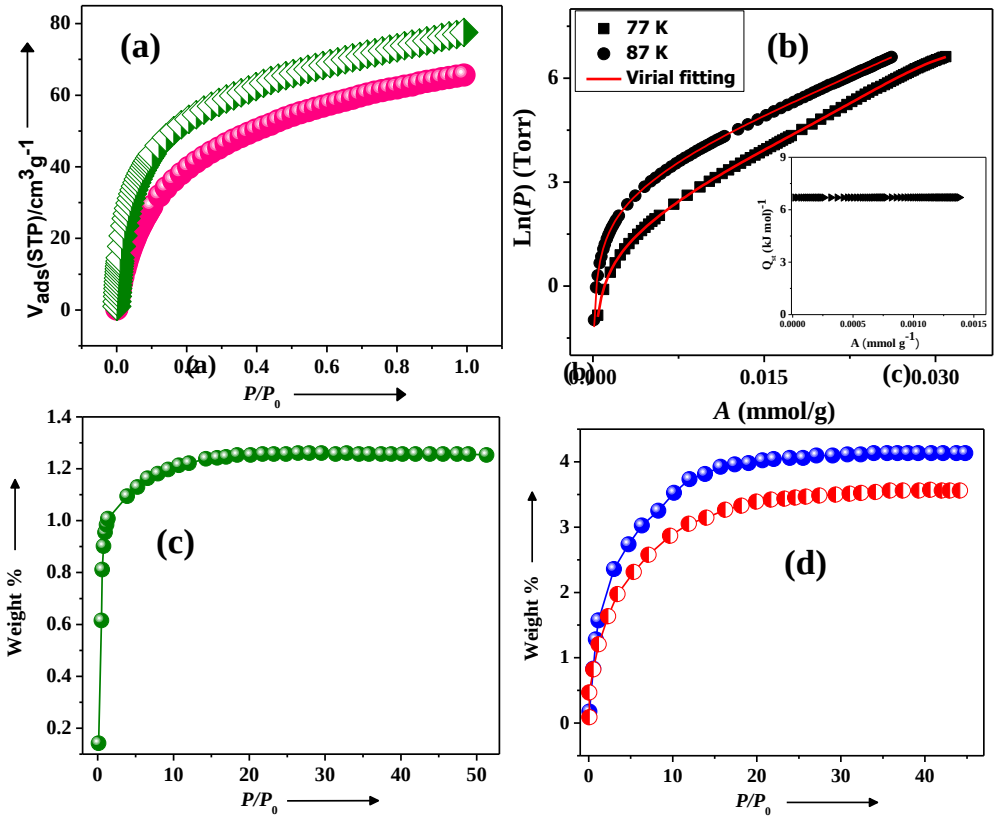

Fig. 6: (a) H_2 adsorption isotherms of **1′** at Pink : 77 K and Blue : 87 K (b) Fitted curves through virial type expression showing corresponding Q_{st} value (in inset) (c) High Pressure (P = 50 bar) H_2 adsorption isotherm at 77 K (in weight %) (d) High pressure CH_4 uptake; Blue: 273 K (P = 45 bar); Red: 298 K (P = 45 bar).

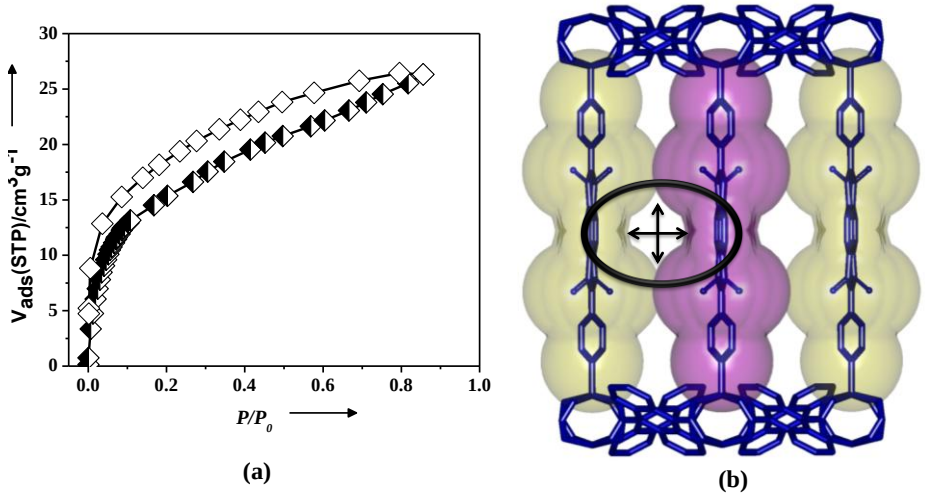

Fig. 7: (a) CO_2 adsorption isotherm of **2′** at 195K (b) Effective pore view (after surface addition) along *a* direction showing blocking of pore window.

Surprisingly measurement of N_2 on non-interpenetrated **2′** does not show any uptake though there has been 58.6 % void space in the framework. Even CO_2 uptake at 195 K shows only 5.1 wt% (26 cm^3 g^{-1}) of storage capacitty (Fig. 7 a). Here the orientation of the bulky bpNDI is blocking the pore window and effectively decreasing the pore size (3.13×4.35 $Å^{2)}$ (Fig. 7 b) along with increment in diffusion behaviour.

4.3.5 Luminescence Property

Coordination polymers, especially those with d^{10} metal centers, have been vastly investigated for their luminescent properties and potential applications. **2** has been found to exhibit quite interesting photophysical property. Solid state UV-Vis spectrum (Fig. 8 a) of **2** showed a broad band in visible region along with main characteristics band in UV region. The broad band in visible region can be easily discriminated into two bands; λ_{max} for the first band is at 476 nm and for the second band λ_{max} is at 532 nm. Broad band in visible region is generally attributed to ground state charge transfer i.e. partial charge separation or complete charge separation (electron transfer). In order to confirm that, EPR has been performed and it showed one electron transfer. There are only three possible pathways for exhibiting electron transfer. First, from donor adc to electron deficient bpNDI though they are not in close proximity other than long range electron transfer through coordination bonds. [25] Second, from donor to acceptor, in space, through solvent molecules [25] and third, from bpNDI to bpNDI considering optimum distance of 3.5 Å.[26] But the separation between two bpNDI ligands is 8.0 Å and the donor adc and solvent molecules are also not within perfect distance. Thus, the only possibility of transferring electron is from adc to bpNDI through coordination bonds. Thus, both bpNDI and adc must be in the radical ion-pair state. The band at 476 nm can be correlated to radical ion-pair state of bpNDI.[27] Hence the next band at 528 nm might be due to radical ion-pair state for adc and its confirmation is yet to be done.

The luminescent properties of **2** and free ligand (adc) were measured in the solid and solution state respectively (Fig. 8 c, d). The λ_{max} values of monomer at 397, 420, 445 and 472 in the emission spectra corresponded to the π–π^* electronic transitions of the anthracene unit and its respective bands in the ultraviolet region (λ_{mon} = 450 nm) have been given in the excitation spectra.[28]. But, **2** showed considerable bathochromic shift in the emission spectrum as compared to the monomeric emission and its broad nature might be assigned as ligand (adc) to metal (Zn^{II}) charge transfer transition (LMCT).[29-37] Hence a part of total adc

ligand is interacting with metal and the remaining ligand is involved with bpNDI in electron transfer process. bpNDI Ligand has negligible contribution in emission due to its very low fluorescent quantum yield (Φ_f ~ 0.003) and additionally it exists in radical ion-pair state [14 c].

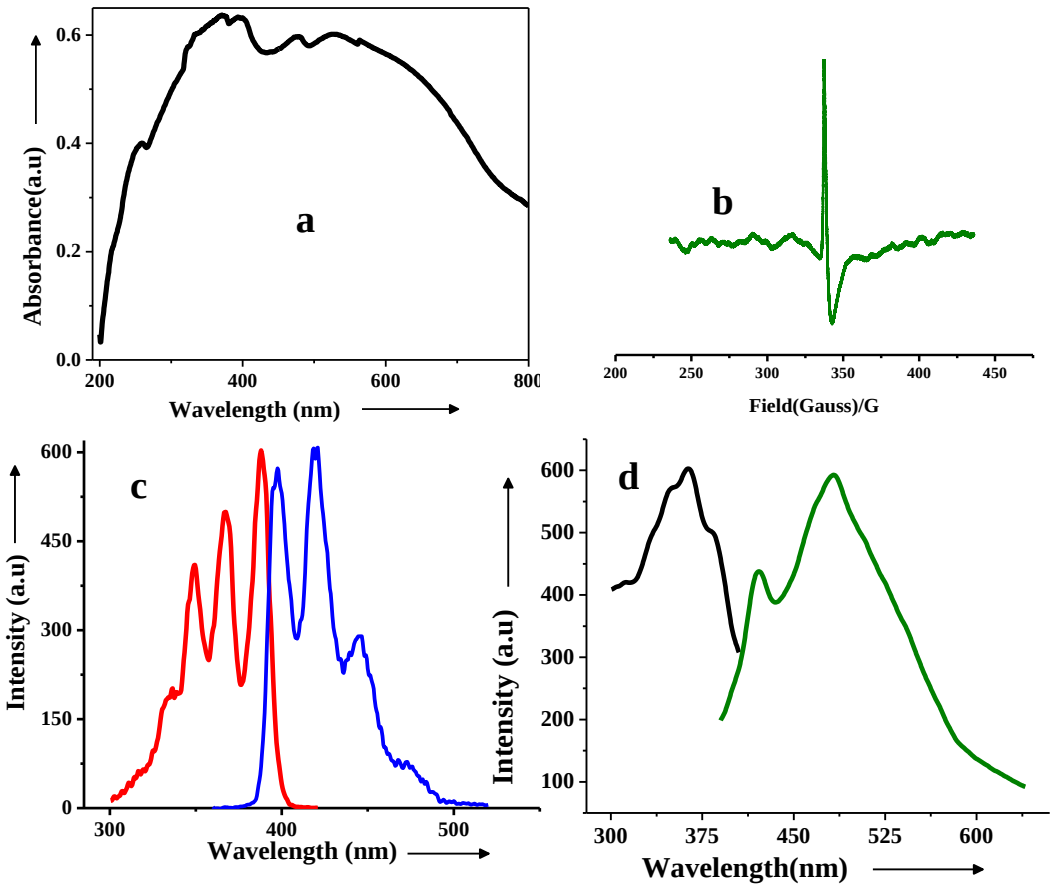

Fig. 8: (a) Solid state UV-Vis spectra of **2** (b)) EPR signal of **2** (g = 2.2543). c. Excitation spectra (λ_{mon} = 450 nm) and emission spectra of monomer adc (λ_{ex} = 360 nm) d. Emission spectra of **2** (λ_{ex} = 360 nm) and corresponding excitation spectra (λ_{ex} = 485 nm).

Excitation spectrum of **2** indicates presence of characteristics adc π–π* electronic transitions . The molecular formula of the framework **2** and the close view of the building unit clearly suggest that the ratio of adc to bpNDI in **2** is 2:1. Thus, it is obvious that one molecule of adc ligand is involved in transfer of one electron to one bpNDI and the other ligand is free to couple with metal orbital responsible for LMCT.

Coordination of the metal cations will help in the electronic coupling between the constituting ligands with the metal ions considerably. This could change the energy of their molecular orbitals, and rearrange the metal-based orbitals. Thus, if the electron-transfer pathway is being involved through the metalloligand complex moiety, one would expect a significant change in reaction rate.[25] But in this case, it has not been possible to monitor the rate of transfer since during solvothermal synthesis of the crystals, the electron transfer might have occurred.

4.4 Conclusion

In conclusion, we have introduced a very simple and straight forward strategy by judicial designing of organic building struts and successfully the degree of interpenetration in MOFs could have been controlled. Bulky 9,10-anthracenedicarboxylic acid unit has been found to be very effective over 1,4-benzenedicarboxylic acid although there has been presence of long linker bpNDI. But due to steric effect of bpNDI, the desired porosity could not have been achieved but we are currently being involved in investigating other MOF systems to confirm to what extent this method can be further utilised, modified and generalised. But interestingly this framework shows long range electron transfer along with strong luminescence and probably this would be the first example exhibiting this kind of behaviour in a system. Though this framework could not stand as expected but here we have succeeded to introduce a new very simple, straightforward method based on diatopic ligand and we are trying to exploit this in our extended work.

4.5 References

1. *(a)* G. Férey, *Chem. Soc. Rev*., 2008, **37**, 191; *(b)* S. Kitagawa, R. Kitaura and S. I. Noro, *Angew. Chem., Int. Ed*., 2004, **43**, 2334; *(c)* T. K. Maji and S. Kitagawa, *Pure Appl. Chem.*, 2007, **79**, 2155; *(d)* T. K. Maji, R. Matsuda and S. Kitagawa, *Nat. Mater*., 2007, **6**, 142.

2. *(a)* H. K. Chae, M. Eddaoudi, J. Kim, S. I. Hauck, J. F. Hartwig, M. ÓKeeffe and O. M. Yaghi, *J. Am. Chem. Soc*., 2001, **123**, 11482; *(b)* M. Eddaoudi, D. B. Moler, H. L. Li, B. L. Chen, T. M. Reineke, M. ÓKeeffe and O. M. Yaghi, *Acc. Chem. Res*., 2001, **34**, 319; *(c)* L. Pan, B. Parker, X. Huang, D. H. Olson, J. Y. Lee and J. J. Li, *J. Am. Chem. Soc*., 2006, **128**, 4180; *(d)* R. Matsuda, R. Kitaura, S. Kitagawa, Y. Kubota, R. V. Belosludov, T. C.

Kobayashi, H. Sakamoto, T. Chiba, M. Takata, Y. Kawazoe and Y. Mita, *Nature*, 2005, **436**, 238.

3. *(a)* P. Kanoo, R. Matsuda, M. Higuchi, S. Kitagawa and T. K. Maji, *Chem. Mater*., 2009, **21**, 5861; *(b)* P. Kanoo, K. L. Gurunatha and T. K. Maji, *J. Mater. Chem*., 2010, **20**, 1322; *(c)* S. Q. Ma, D. F. Sun, J. M. Simmons, C. D. Collier, D. Q. Yuan and H. C. Zhou, *J. Am. Chem. Soc*., 2008, **130**, 1012; *(d)* P. Kanoo, R. Matsuda, M. Higuchi, S. Kitagawa and T. K. Maji, *Chem. Mater*., Vol. 21, **24**, 2009.

4. *(a)* H. K. Liu, W. Y. Sun, W. X. Tang, T. Yamamoto and N. Ueyama, *Inorg. Chem*., 1999, **38**, 6313.

5. *(a)* J. Fan, W. Y. Sun, T. A. Okamura, J. Xie, W. X. Tang and N. Okamura, *New J. Chem*., 2002, **26**, 199; *(b)* A. N. Parvulescu, G. Marin, K. Suwinska, V. C. Kravtsov, M. Andruh, V. Parvulescu and V. I. J. Parvulescu, *J. Mater. Chem*., 2005, **15**, 4234.

6. *(a)* P. Horcazada, C. Serre, M. Sebban, F. Taulelle and G. Férey, *Angew. Chem., Int. Ed*., 2006, **45**, 5974; *(b)* P. Horcazada, C. Serre, G. Maurin, N. A. Ramsahye, F. Balas, M. Vallet-Regi, M. Sebban, F. Taulelle and G. Férey, *J. Am. Chem. Soc*., 2008, **130**, 6774.

7. *(a)* S. Henke, R. Schmidt and J. D. Grunwaldt, *Chem. Eur. J*., 2010, **16**, 14296; *(b)* Z. Q. Wang and S. M. Cohen, *J. Am. Chem. Soc*., 2009, **131**, 16675.

8. *(a)*O. K. Farha, I. Eryazici, N. C. Jeong, B. G. Hauser, C. E. Wilmer, A. A. Sarjeant, R. Q. Snurr, S. B. T. Nguyen, A. Ö. Yazaydin and J. T. Hupp, *J. Am. Chem. Soc*., 2012, **134**, 5016.

9. *(a)* A. Hazra, P. Kanoo and T. K. Maji, *Chem. Commun*., 2011, **47**, 538–540; *(b)* X. S. Wang, S. Ma, P. M. Forster, D. Yuan, J. Eckert, J. J. Lopez, B. J. Murphy, J. B. Parise and H. C. Zhou, *Angew. Chem. Int. Ed*., 2008, **47**, 7263.

10. J. Hafizovic, M. Bjorgen, U. Olsbye, P. D. C. Dietzel, S. Bordiga, C. Prestipino, C. Lamberti and K. P. Lillerud, *J. Am. Chem. Soc*., 2007, **129**, 3612.

11. O. Shekhah, H. Wang, M. Paradinas, C. Ocal, B. Schupbach, A. Terfort, D. Zacher, R. A. Fischer and C. Woll, *Nat. Mater*., 2009, **8**, 481.

12. O. Shekhah, H. Wang, S. Kowarik, F. Schreiber, M. Paulus, M. Tolan, C. Sternemann, F. Evers, D. Zacher and R. A. Fischer, C. Woll, *J. Am. Chem. Soc*., 2007, **129**, 15118.

13. O. K. Farha, C. D. Malliakas, M. G. Kanatzidis and J. T. Hupp, *J. Am. Chem. Soc*. 2010, **132**, 950.

14. *(a)* B. Liu, Y. Li, L. Hou, G. Yang, Y. Y. Wang and Q. Z. Shi, *J. Mater. Chem. A*, 2013, **1**, 6535; *(b)* K. L. Mulfort, O. K. Farha, C. D. Malliakas, M. G. Kanatzidis and J. T. Hupp, *Chem. Eur. J*. 2010, **16**, 276; *(c)* Y. Takashima, V. M. Martínez, S. Furukawa, M. Kondo, S. Shimomura, H. Uehara, M. Nakahama, K. Sugimoto and S. Kitagawa, *Nat. Commun*., 2011, **2**, 168.

15. B. Q. Ma, K. L. Mulfort and J. T. Hupp, *Inorg. Chem*., 2005, **44**, 4912.

16. P. H. Dinolfo, M. E. Williams, C. L. Stern and J. T. Hupp, *J. Am. Chem. Soc*., 2004, **126**, 12989.

17. *SMART (V 5.628), SAINT (V 6.45a), Xprep, SHELXTL*; Bruker AXS Inc. Madison, Wisconsin, USA, 2004.

18. G. M. Sheldrick, *Siemens Area Detector Absorption Correction Program*, University of Götingen, Götingen, Germany, 1994.

19. A. Altomare, G. Cascarano, C. Giacovazzo and A. Gualaradi, *J. Appl. Crystallogr*., 1993, **26**, 343.

20. G. M. Sheldrick, SHELXL-97, *Program for Crystal Structure Solution and Refinement*, University of Götingen, Götingen, Germany, 1997.

21. A. L. Spek, *J. Appl. Crystallogr*., 2003, **36**, 7.

22. G. M. Sheldrick, SHELXS 97, *Program for the Solution of Crystal Structure*, University of Götingen, Germany, 1997.

23. L. J. Farrugia, *J. Appl. Crystallogr*., 1999, **32**, 837.

24. Z. Zhang, S. Xiang, X. Rao, Q. Zheng, F. R. Fronczek, G. Qian and B. Chena, *Chem. Commun.*, 2010, **46**, 7205.

25. M. Andersson, M. Linke, J. C. Chambron, J. Davidsson, V. Heitz, L. Hammarström and J. P. Sauvage, *J. Am. Chem. Soc*., 2002, **124**, 4347.

26. L. Han, L. Qin, L. Xu, Y. Zhou, J. Sunb and X. Zou, *Chem. Commun*., 2013, **49**, 406.

27. S. Guha and S. Saha, *J. Am. Chem. Soc*., 2010, **132**, 17674.

28. D. Tanaka, S. Horike, S. Kitagawa, M. Ohba, M. Hasegawa, Y. Ozawac and K. Toriumi, *Chem. Commun*., 2007, **43**, 3142.

29. M. D. Allendorf, C. A. Bauer, R. K. Bhakta, and R. J. T. Houk, *Chem. Soc. Rev*., 2009, **38**, 1330.

30. J. C. Dai, X. T. Wu, Z. Y. Fu, S. M. Hu, W. X. Du, C. P. Cui, L. M. Wu, H. H. Zhang and R. Q. Sun, *Chem. Commun*., 2002, **12**, 12.

31. Q. Fang, G. Zhu, G. W. Xin Shi, R. W. Ge Tian and S. Qiu, *J. Solid State Chem*., 2004, **177**, 1060.

32. Q. Fang, G. Zhu, M. Xue, J. Sun, F. Sun and S. Qiu, *Inorg. Chem*., 2006, **45**, 3582.

33. J. Fan, H. F. Zhu, T. A. Okamura, W. Y. Sun, W. X. Tang and N. Ueyama, *New J. Chem*., 2003, **27**, 1409.

34. Q. Fang, G. Zhu, M. Xue, J. Sun, G. Tian, G. Wu and S. Qiu, *Dalton Trans*., 2004, **14**, 2202.

35. J. C. Dai, S. M. Hu, X. T. Wu, Z. Y. Fu, W. X. Du, H. H. Zhang and R. Q. Sun, *New J. Chem*., 2003, **27**, 914.

36. J. C. Dai, X. T. Wu, Z. Y. Fu, C. P. Cui, S. M. Hu, W. X. Du, L. M. Wu, H. H. Zhang and R. Q. Sun, *Inorg. Chem*., 2002, **41**, 1391.

37. J. X. Chen, S. X. Liu and E. Q. Gao, *Polyhedron*, 2004, **23**, 1877.

Chapter 5

Guest Induced Electron Transfer at Room Temperature in a Redox-Active Porous Framework: Tuning of Adsorption Property

Abstract

This chapter has reported the synthesis, structural details, characterization of a photoactive, luminescent, permanently porous, three dimensional interpenetrated framework $\{[Cd(bpdc)(bpNDI)]\cdot 4H_2O\cdot DMF\}_n$ (**1**)**.** A detailed photophysical study has been performed on this framework containing photoactive N,N′-dipyrid-4-yl-1,4,5,8-naphthalenediimide (bpNDI) strut. Strut bpdc, being a poor donor and well separated from the strong electron acceptor bpNDI, does not interact strongly with it. In order to achieve better photophysical property, different benzene and naphthalene based good electron donor molecules have been successfully incorporated into the framework. Due to very strong confinement effect, it has been possible to observe strong host-guest interaction through a little bit rare room temperature one electron transfer from donor guest to acceptor host. After the electron transfer, the framework retains its luminescent property though the origin of luminescence has been found to be shifted from LMCT to linker (bpdc) based emission. It has been also possible to tune its adsorption property through inclusion of guest donor molecules. To the best of our knowledge this would be the first example showing this kind of guest induced very strong host-guest interaction through a well charge separated state and the corresponding room temperature electron transfer.

5.1 Introduction

The last one decade has witnessed a dramatic progress of synthesis, structural characterizations and versatile applications of metal-organic frameworks, a novel class of porous crystalline materials.[1-4] The well-defined, nanoscale tunable coordination space of such framework materials has been well utilized for gas storage, luminescence, separation, catalysis, sensing and drug delivery applications.[5–10] Much work is being currently involved in selective functionalization of MOFs through addition of different functional groups to the organic linkers or tuning of the inorganic building blocks of the host framework so that the accessible void spaces of these materials can be utilised in a better way. In this way redox-active organic molecules can be embedded into the framework as the framework scaffold in order to explore MOFs for different potential purposes such as colorimetric sensors, optoelectronic materials etc[11-16].

Photo/thermal induced electron transfer is of paramount importance in solar energy conversion, molecular photonics and the mimicry of natural photosynthetic system. For the fabrication of such species, the most important parameter is spatial-organization of donor and acceptor molecules in appropriate manner to create effective channels for electron transfer. Long lived charge separated state with high quantum yield and high lifetime are the primary criteria for the construction of an efficient solar cell and conversion of light to electrical energy.[1]

In this regard, MOFs based on D-A array systems have several advantages [2] over other supramolecular organizations or aggregates such as a. both donor (D) and or acceptor as a linker can be integrated in a framework system through coordinate bonding b. traditional MOFs can also be considered as a stable host for accommodation of guest D or A molecules that can well organize individually or both in coordination space c. guest responsive electron transfer based on supramolecular interactions (π-π/ or H-bonding) is beneficial for photovoltaic application as charge recombination would be inhibited by long D-A distance. d. versatile systems can be introduced and electron transfer pathway can be controlled.

1,4,5,8-naphthalenediimide (NDI) has been found to be robust, redox-active organic strut which can be an excellent candidate for constructing optoelectronic active MOFs. It has been a very well-known molecule because of its efficient electron accepting capability due to large conjugate planes and special electronic properties. It can be readily

reduced by chemical or electrochemical method (E = -1.1 V in CH_2Cl_2 solvent) to form stable radical anions [(1)] and exhibit n-type over p-type semiconducting nature with high electron mobility.[(14)]

Expectedly 1,4,5,8-naphthalenediimides (NDIs) based linker have attended significant attention for the synthesis of MOFs. N-based long linker bpNDI (*N*,*N*′-di(4-pyridyl)-1,4,5,8-naphthalenediimide) has been first introduced in MOFs by Hupp *et al.*[(12a)] In this paper, several MOFs based on this bpNDI have been synthesised along with different carboxylate linker to tune the channel dimension and specific surface area. Later, same group has shown Li ion reduction of bpNDI based MOF $[Zn_2(NDC)_2(bpNDI)]_n$ (bpNDI which is reversibly reducible at -0.79 to -1.30V versus the ferrocene couple) and its substantially increases in the N_2 and H_2 uptake (0.93 wt % to 1.63 wt %) with increase of isosteric heat of adsorption.[(12b)] Later Kitagawa *et.al.* reported other novel NDI based MOF where charge-transfer interactions with electron-donating aromatic donor molecules.[(12c)] Later, this kind of study has been continued further by this same group in a different NDI based system. This system, $\{[Zn_2(bDC)_2(bpNDI)]\cdot 4DMF\}_n$ exhibits strut induced long range charge separated state and has been utilised for molecular decoding on changing different organic vapours. But very few have investigated the photophysical and photochemical properties of these type of redox active frameworks so far. It could be anticipated that combining photoactivity and porosity together would offer a new kind of multifunctional materials [(12)] in this field and could have potential applications ien information storage, optical switches, photomechanics, and so on.[(16)]

Here we report synthesis, structural characterizations of a photoactive luminescent novel Cd based MOF $\{[Cd(bpdc)(bpNDI)]\cdot 4H_2O\cdot DMF\}_n$ (**1**) (bpdc= 4,4′-biphenyldicarbixylic acid; dpNDI, *N*,*N*′-di(4-pyridyl)-1,4,5,8-naphthalenediimide), derived from extended N-pyridyl NDI linker and biphenyl dicarboxilate. It is a dinuclear 3D porous framework with two fold entanglement .High framework stability is realized by special type of SBU, inhibiting network movements. Framework shows highly selective CO_2 uptake properties. Further, long lived complete charge separated state has been achieved based on electron rich aromatic donor guest molecules followed by tuning of luminescent properties. Guest responsive CO_2 uptake characterestics have been modulated and further studied.

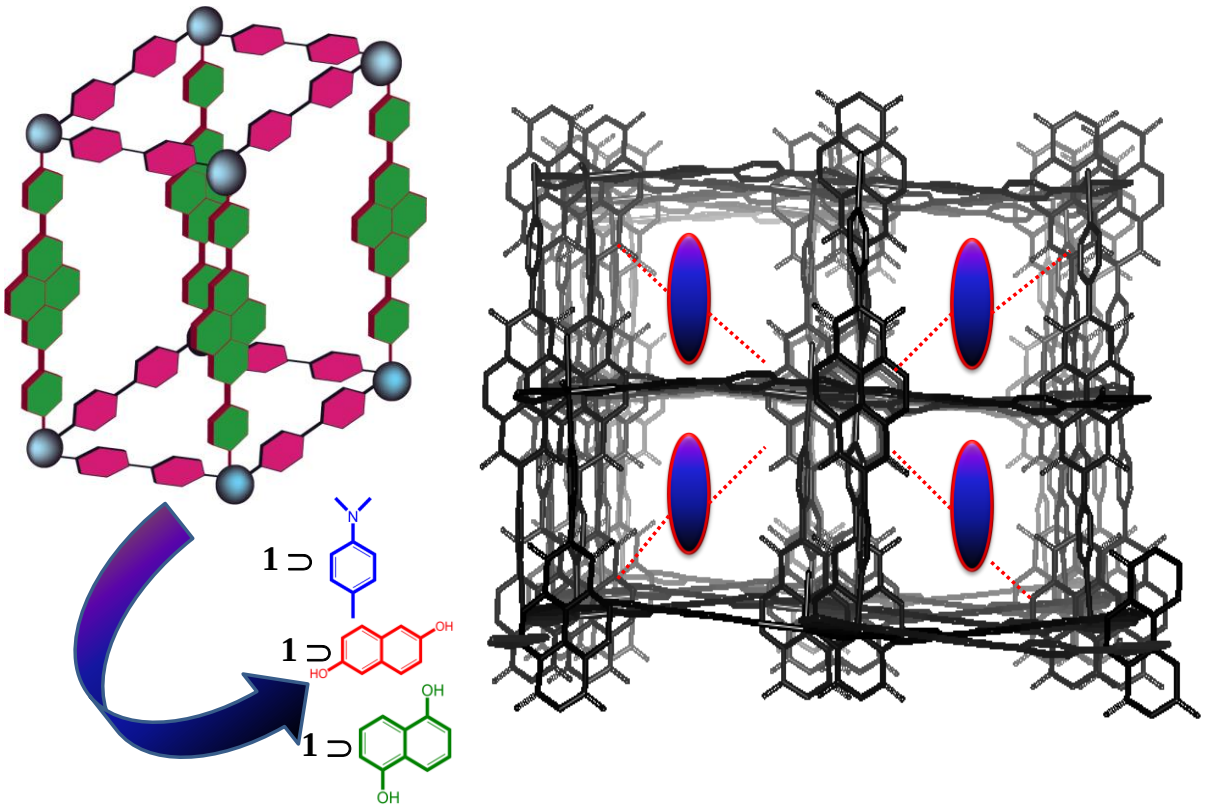

Scheme 1: Schematic view of confinement effect

5.2 Experimental Section

5.2.1 Materials

All the reagents employed were commercially available and used as provided without further purification. Metal salt was obtained from Spectrochem. 4,4′-biphenyldicarbixilic acid, 1,5-dinaphthol, 2,6-dinaphthol and 4,*N*,*N*-trimethylaniline were obtained from Sigma Aldrich Co. *N*,*N*′-di(4-pyridyl)-1,4,5,8-naphthalenediimide was synthesised following the literature procedure [(17)].

5.2.2 Physical Measurements

Elemental analysis was carried out using a Thermo Fischer Flash 2000 Elemental Analyzer. Thermogravimetric analysis (TGA) was carried out (Metler Toledo) in nitrogen atmosphere (flow rate =50 mL min^{-1}) in the temperature range 30–500 °C (heating rate 3 °C min^{-1}). Powder XRD pattern of the products were recorded by using Mo-Kα radiation (Bruker D8 Discover; 40 kV, 30 mA).The pattern was agreed with those calculated from

single crystal structure determination. NMR spectra were obtained with a Bruker AVANCE 400 (400 MHz) Fourier transform NMR spectrometer with chemical shifts reported in parts per million (ppm). Electronic absorption spectra were recorded on a Perkin Elmer Lambda 900 UV-VIS-NIR spectrometer and emission spectra were recorded on Perkin Elmer Ls 55 Luminescence Spectrometer.

5.2.3 X-Ray Crystallography

X-ray single-crystal structural data of **1** was collected on a Bruker Smart-CCD diffractometer equipped with a normal focus, 2.4 kW sealed tube X-ray source with graphite monochromated Mo-Kα radiation (λ= 0.71073 Å) operating at 50 kV and 30 mA. The program SAINT [(18)] was used for integration of diffraction profiles and absorption correction was made with SADABS [(19)] program. All the structures were solved by SIR92 (20) and refined by full-matrix least-squares method using SHELXL-97.[(21)] All the hydrogen atoms were geometrically fixed and placed in ideal positions. Potential solvent accessible area or void space was calculated using the PLATON multipurpose crystallographic software. [(22)] All crystallographic and structure refinement data of **1** are summarized in Table 1. Selected bond lengths and angles for **1**, are given in Table 1 and 2, respectively All calculations were carried out using SHELXL 97, [(21)] PLATON, [(22)] SHELXS 97 [(23)]) and WinGX system, Ver 1.70.01.[(24)]

5.2.4 Adsorption Study

The adsorption isotherms of CO_2, H_2, N_2, Ar and O_2 (195 K) using the dehydrated sample of **1** (**1′)** were measured by using a QUANTACHROME QUADRASORB-SI analyzer. Sample **1′** has been prepared after MeOH exchange for continuous 3 days followed by heating at 80° C under a 1×10^{-1} Pa vacuum for about 12 h prior to measurement of the isotherms. Helium gas (99.999% purity) at a certain pressure was introduced in the gas chamber and allowed to diffuse into the sample chamber by opening the valve. The amount of gas adsorbed was calculated readily from pressure difference (P_{calc}- P_e), where P_{calc} is the calculated pressure with no gas adsorption and P_e is the observed equilibrium pressure. All operations were computer-controlled and automatic.

5.2.5 Synthesis of {[Cd(bpdc)(bpNDI)]·4H_2O·DMF}$_n$ (1)

A mixture containing $Cd(NO_3)_2·4H_2O$ (0.1 mmol, 0.030 g), bpdc (0.1 mmol, 0.012g) and bpNDI (0.1 mmol,0.021g) was suspended in DMF (10 mL) and heated to 80 °C for a period of 3 days. The slightly yellow crystals of **1** were then collected after washing with DMF for several times. Yield: 88%. Anal. Calc. for **1** ,: C: 53.59; H: 3.81; N: 7.62; Found C: 53.53; H: 3.76; N: 7.60. FTIR (KBr pellet, 4000–400 cm^{-1}): 3200–3620(S), 3053(m), 1654(w), 1609(S), 1544(S), 1388(S).

5.2.6 Preparation of 1 @ 2,6-dinaphthol, 1 @ 1,5-dinaphthol and 1 @ DMPT:

Around 140 mg (0.16 mmol) of **1′** have been continuously stirred with methanolic solution (8 mL) of 2,6-dinaphthol, 1,5-dinaphthol [56 mg (0.32 mmol)] for 3 days prior to inclusion. For preparing of **1** @ DMPT (DMPT = 4,*N*,*N*-trimethylaniline), **1′** has been stirred with around 8 mL of DMPT. Within one day, the colour of **1′** changes from yellowish to dark bluish green. The precipitates are collected, washed with MeOH for several times, dried in open atmosphere and used for all experiments. These have been characterised through PXRD (Fig. 5), TGA (Fig. 6), NMR (Fig. 7a,7b,7c), and elemental analysis. The inclusion amount for each guest molecule e.g. DMPT,1,5-dinaphthol and 2,6-dinaphthol have been confirmed well from TGA, NMR and elemental analysis and it has been found to be 50%, 90% and 98% respectively. Anal. Calcd. for **1** @ DMPT [$C_{38}O_{12}CdH_{28}N4$, 0.5 DMPT]: C: 63.78; H: 4.31; N: 7.88; Found C: 63.71; H: 4.3; N: 7.83; for **1** @ 1,5-dinaphthol [$C_{38}O_8Cd\ H_{20}N_4$, 0.9(1,5-dinaphthol], 1.5 H_2O]: C: 64.25; H: 3.14; N: 6.14; Found C: 64.21; H: 3.10; N: 7.81 and for **1** @ 2,6-dinaphthol [$C_{38}O_{11}CdH_{26}N_4$, 0.98(2,6-dinaphthol)]: C: 64.31; H: 3.64; N: 6.14; Found C: 64.30; H: 3.62; N: 6.10.

5.3 Results and Discussion:

5.3.1Crystal Structure Description of {[Cd(bpdc)(bpNDI)]·4H_2O·DMF}$_n$ (1) :

X-ray single crystal structure determination reveals that **1** crystallizes in monoclinic $P2_1/n$ space group and shows a 3D framework of Cd^{II} bridged by bpdc and bpNDI linkers. The asymmetric unit of **1** comprises one Cd^{II} centers (Cd1), one molecule of bpdc, one molecule of bpNDI along with one guest DMF molecule and four water molecules. The carboxylate oxygen $\{\mu_2\text{-OCO}\}_2$ (O3) bridged the two Cd^{II} centres, resulting in a binuclear$\{Cd_2(\mu_2\text{-OCO})_2\}$SBU, which are extended into 2D rhombic layer by bpdc linkers along [101] direction . This 2D layer is further pillared by bpNDI linkers through pyridyl-N coordination to generate a 3D framework structure with α-Po type topology. The each Cd^{II} centre in the framework is seven-coordinated with distorted pentagonal bipyramidal geometry. The equatorial 3rd, 4th, 5th and 6th coordinations are furnished by two bidentate bpdc ligands (O1, O2, O3 and O4) through chelation and one position is oxobridged by μ_2-O3 of another bpdc ligand. This dinuclear $\{Cd_2(\mu_2\text{-OCO})_2\}$ SBU direct to connect two bpNDI parallelly along *b* direction and satisfy the remaining two axial positions (N1 and N4). Here, the versatile coordination geometry of Cd^{II} dictates this type of bipillared layer type 3D framework with bidirectional channel sizes of 1.5×2.5 $Å^2$ (along *c* direction) and 2.5×6.0 $Å^2$ (along [101] direction). Due to presence of long linker bpNDI, it results into large cavities in the structure but further nucleation takes place along those cavities and lead to similar 3D networks resulting to overall two-fold interpenetration. However, this causes drastic reduction in pore volume although the framework still exhibits considerable microporous nature in which the solvent molecules reside. The Cd···Cd, Cd-O, Cd-O (μ_2) and Cd-N bond distances range as 3.983, 2.320(5)-2.549(5) Å, 2.381 Å and 2.340(7)-2.343(7) Å respectively. Calculation of void space using PLATON after removal of guest molecules suggests the presence of void volume of ~1496 Å i.e. 32 % of the total cell volume.

Table 1: Crystal data and structure refinement parameters of **1**

Parameters	**1**
Empirical formula	$C_{38}H_{20}CdN_5O_{13}$
Formula weight	909.08
Crystal system	Monoclinic

Space group	$P2_1/n$
a, Å	11.7797(6)
b, Å	29.1825(9)
c, Å	14.2285(6)
α, deg	90
β, deg	100.679(4
γ, deg	90
V, Å^3	4806.5(4)
Z	4
T, K	293
μ, mm^{-1}	0.515
D_{calcd}, g/cm^3	1.256
F (000)	1836
Reflections[$I>2\sigma(I)$]	5353
Total reflections	50241
Unique reflections	9422
λ(Mo-Kα)	0.71073
R_{int}	0.102
GOF on F^2	0.94
$R_1[I>2\sigma(I)]^a$	0.0625
R_w[all data]^b	0.1739

Table 2. Selected bond lengths (Å) for **1**

Cd1-O1	2.467(4)	Cd1-N4_b	2.335(5
Cd1-N1	2.341(5)	Cd1-O3_c	2.555(4)
Cd1-O4_c	2.340(4)	Cd1-O3_g	2.379(4)

Table 2. Selected bond angles (º) for **1**

O1-Cd1-O2	54.20(14)	Cd1-O1-C1	88.3(3)

O1-Cd1-N1	95.51(15)	Cd1-O2-C1	94.6(3)
O1-Cd1-C1	26.74(15)	Cd1_d-O3-C14	87.6(3)
O1-Cd1-N4_b	87.12(16)	Cd1_f-O3-C14	164.8(3)
O1-Cd1-O3_c	140.82(13)	Cd1_d-O3-Cd1_f	107.58(14)
O1-Cd1-O4_c	88.44(14)	Cd1_d-O4-C14	97.6(3)
O1-Cd1-O3_g	146.38(13)	Cd1-N1-C15	119.6(3)
O2-Cd1-N1	90.45(15)	Cd1-N1-C16	122.6(4)
O2 –Cd1-C1	27.46(16)	C15-N1-C16	117.7(5)
O2-Cd1-N4_b	87.13(15)	C19-N2-C20	117.7(5)
O2-Cd1-O3_c	164.61(14)	C19-N2-C21	117.0(4)
O2-Cd1-O4_c	142.49(15)	C20-N2-C21	125.3(5)
O2-Cd1-O3_g	92.34(14)	C32-N3-C33	123.9(5)
N1-Cd1-C1	93.76(16)	C32-N3-C34	117.2(5)
N1-Cd1-N4_b	174.46(17)	C33-N3-C34	118.6(5)
O3_c-Cd1-N1	90.84(13)	C37-N4-C38	116.5(5)
O4_c-Cd1-N1	90.09(15)	Cd1_a-N4-C37	121.8(4)
O3_g-Cd1-N1	87.02(14)	Cd1_a-N4-C38	121.5(4)
N4_b-Cd1-C1	86.39(16)	C1D-N1D-C3D	124.6(16)
O3_c-Cd1-C1	167.21(15)	Cd1-C1-O1	65.0(3)
O4_c-Cd1-C1	115.15(16)	Cd1-C1-C2	174.6(4)
O3_g-Cd1-C1	119.71(15)	O1-C1-O2	123.0(5)
O3_c-Cd1-N4_b	90.18(14)	O1-C1-C2	120.3(5)
O4_c-Cd1-N4_b	94.86(16)	O2-C1-C2	116.8(5)
O3_g-Cd1-N4_b	88.10(16)	Cd1-C1-O2	58.0(3)
O3_c-Cd1-O4_c	52.85(13)	C1-C2-C3	120.3(7)
O3_c-Cd1-O3_g	72.42(12)	C1-C2-C4	123.0(5)
O3_g-Cd1-O4_c	125.14(13)	C3-C2-C4	116.7(6)

Symmetry transformations used to generate equivalent atoms: b: =1+x,y,-1+z; c: 1/2-x,-1/2+y,-1/2-z and g: 1/2+x,1/2-y,1/2+z

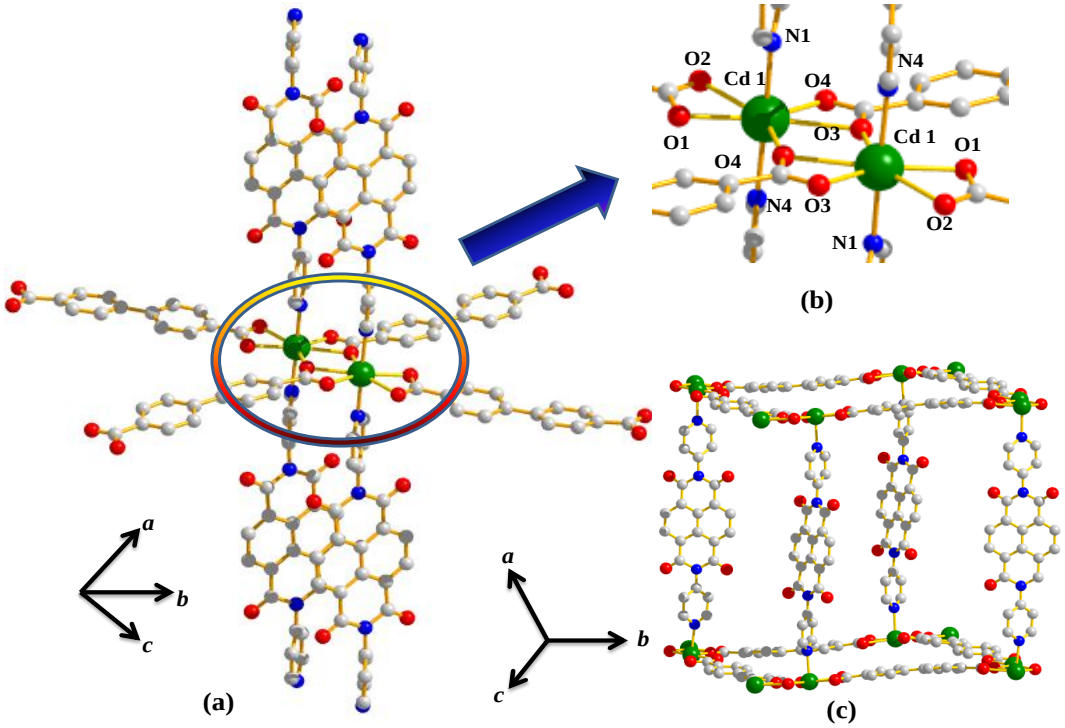

Fig. 1: (a) View of coordination environment of Cd^{II} in **1** (b) Closer view of coordination environment of Cd^{II} (c) Building unit of **1**.

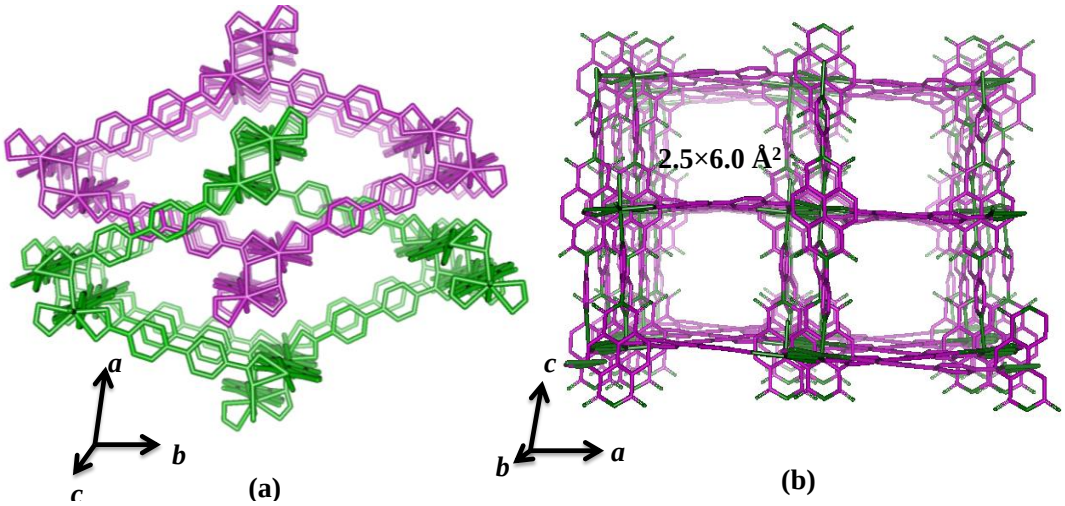

Fig. 2: (a) View of two-fold interpenetration along crystallographic *c*-axis (b) Pore view along crystallographic [101] direction.

5.3.2 Thermal and PXRD Analysis

Thermogravimetric analysis (TGA) of **1** shows rapid initial mass loss of one loosely bound guest water molecule in the temperature range of 55-90 °C (expt., 2.2% cald., 1.9%) and this is consistent with solvent loss as calculated from structural data (Fig. 3). The next

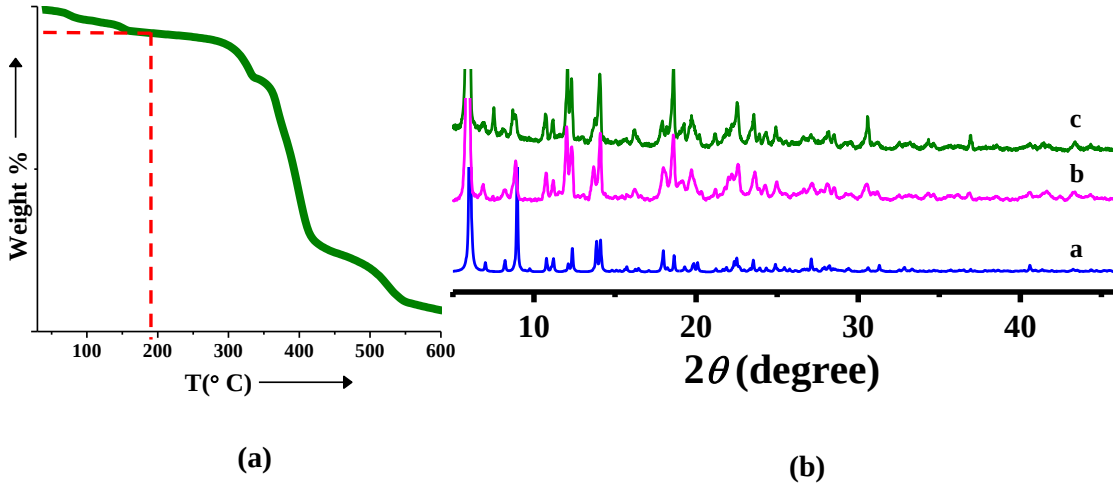

Fig. 3: (a) TGA of as-synthesised **1** (b) PXRD pattern of a. Simulated b. **1** and c. desolvated **1′**.

consecutive steps exhibit release of three guest water molecules from the framework (expt., 6.6% cald.,6 %) in the temperature range of 105-155 °C. The next step reveals the loss of one guest DMF molecule in the temperature range of 160-240 °C (expt., 8% cald., 7.82 %). The **1′** is thermally stable up to 345 °C and then decomposes to an unidentified product. The PXRD patterns of **1** were recorded in different states and are shown in (Fig. 3). The PXRD pattern of **1′** exhibits no such significant change compared to that of **1** suggesting structural rigidity and robust nature of the framework.

5.3.3 Adsorption Studies

To acquire more information about porous properties, N_2 and CO_2 sorption isotherms were recorded at 77 K and 195 K respectively. Despite an adequate effective pore size, N_2 (kinetic diameter 3.64 Å) adsorption study at 77 K with **1′** showed a type II adsorption profile. Considering pore aperture N_2 molecules might have interacted strongly with pore aperture and block other molecules to pass through, and resulting in high diffusion barrier [7e].

But at 195 K, **1′** showed a type I CO_2 sorption isotherm without hysteresis (Fig. 4), giving an apparent Langmuir and BET surface areas of 286 $m^2 g^{-1}$.and 267 $m^2 g^{-1}$

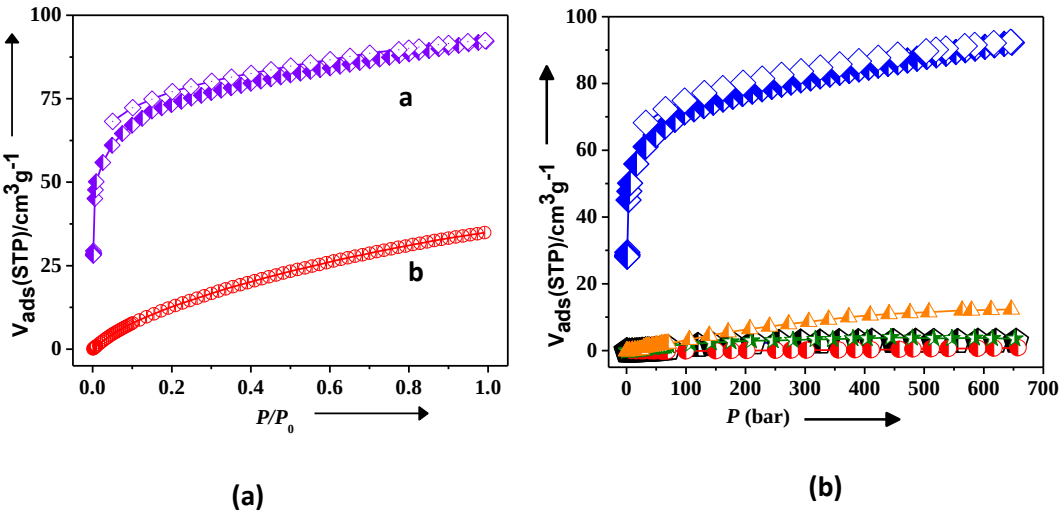

Fig. 4: (a) CO_2 adsorption isotherms for compound **1′** a. at 195 K and b. at 293 K (b) Selectivity plot at 195 K ; Blue: adsorption–desorption isotherms for compound **1′**; Orange: Ar; Black: N_2; Green: H_2 and Red: O_2.

The saturated CO_2 uptake at 195 K is 92 cm^3 g^{-1}, corresponding to18 wt% or 3.1 CO_2 per formula unit. At 293 K, it shows CO_2 uptake of 34 cm^3 g^{-1} (Fig. 4), and it corresponds to 6.8 wt%, 1.1 CO_2 per formula unit. The exclusion over other gases at 195 K (Fig. 4) is not rare but it has importance in the separation of mixtures of gases. The considerable affinity toward CO_2 in contrast to N_2/Ar/O_2/H_2 by **1′** is probably because of the quadrupolar nature of the CO_2 molecule (quadrupole moment of CO_2: -1.4×10^{-39} Cm^2) and its strong interaction with the adsorption sites (e.g., uncoordinated carbonyl oxygen in NDI core) of the framework giving rise to considerably higher CO_2/N_2, Ar, O_2, H_2 selectivity. The strong interaction of CO_2 with **1′** is also reflected in the high value of isosteric heat of adsorption, $q_{st,\phi}$, (33.3 kJ mol^{-1}) as calculated by the Dubinin–Radushkevich [25] (DR) equation.

5.3.4 Inclusion of Guest Molecules

Considering the characteristic photophysical features of NDI, several electron rich guest molecules have been encapsulated into the framework scaffold in order to study the effective donor-acceptor interactions. Three different donating guest molecules, 4,*N*,*N*-trimethyl aniline (DMPT), 2,6-dinaphthol (2,6-dinaphthol) and 1,5-dinaphthol (1,5-

dinaphthol) could have been successfully incorporated into the pores of the framework. The resulting visible colour change for each case after incorporation of guest molecules is a clear indication of effective host-guest interaction in solid matrix.

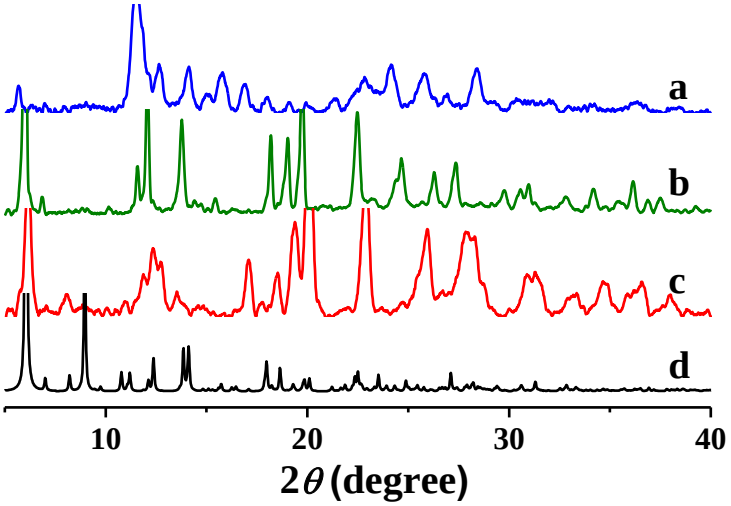

Fig. 5: PXRD pattern of the hybrids a. **1** @ DMPT b. **1** @ 1,5-dinaphthol c. **1** @ 2,6-dinaphthol d. **1**

Powder X-ray diffraction (PXRD) (Fig. 5), measurements were carried out on all the hybrids to determine the structural changes in response to the guest molecule inclusion. All the hybrids show some shifting of the peaks with appearance of new peaks suggesting structural recognization after accommodation of the large guest molecules in the frameworks. Such change can be attributed to different size and shape of the molecules. The incorporation of such large molecules is probably is driven by the effective host-guest π-π interactions and the corresponding confinement effect.

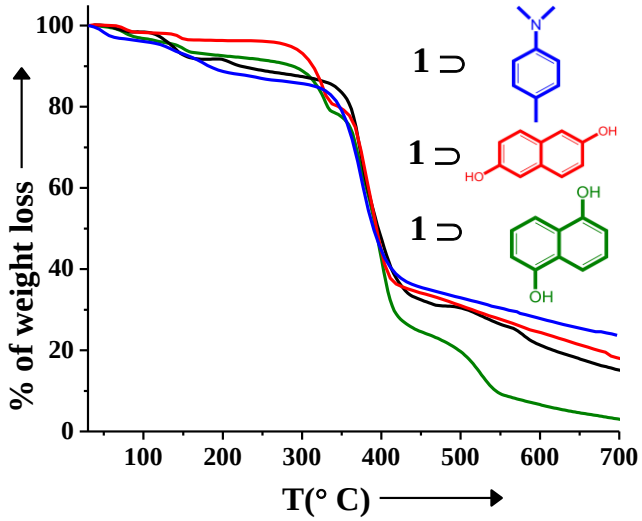

Fig. 6: TGA curve : Black: **1**; Blue: **1** @ DMPT(50%) (expt., 7.82% cald.,8 %); Red: **1** @ 1,5-dinaphthol (90%) (expt., 14.3% cald.,14.4 %); Green : **1** @ 2,6-dinaphthol (98%) (expt., 15.6% cald.,15.68 %)

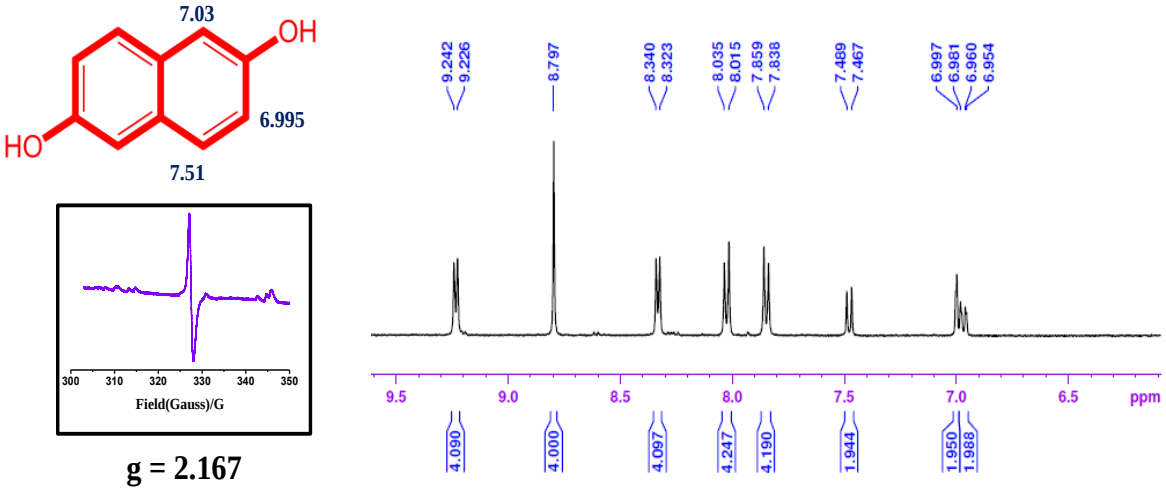

Fig. 7a: ^{1}H-NMR spectra of **1** @ 2,6-dinaphthol in DMSO-d6 after digestion with DCl showing 98 % inclusion.

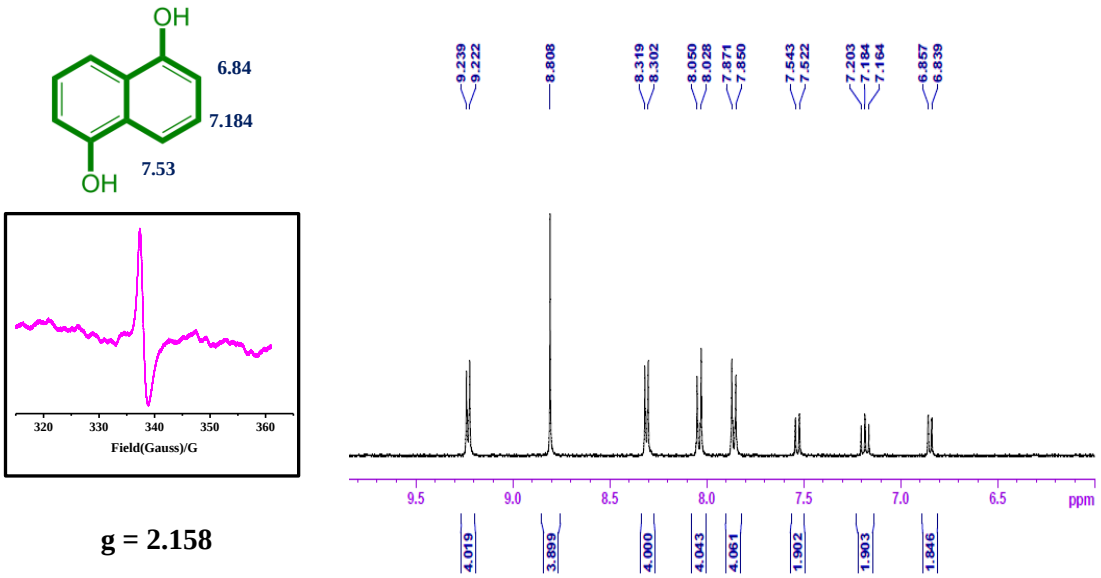

Fig. 7b: ^{1}H-NMR spectra of **1** @ 1,5-dinaphthol in DMSO-d6 after digestion with DCl showing 90 % inclusion.

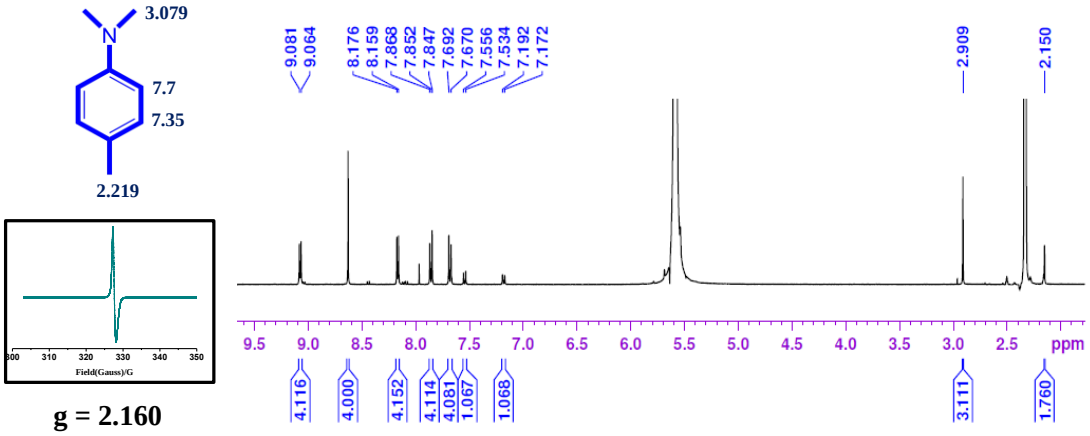

Fig. 7c: ^{1}H-NMR spectra of **1** @ DMPT in DMSO-d6 after digestion with DCl showing 50 % inclusion.

The adsorption isotherms (Fig. 8) for these compounds also support this behaviour. Prior to measurement, the compounds were activated by removing the guest solvent molecules at 130 °C under a vacuum. At 195 K, **1** @ 2,6-dinaphthol and **1** @ 1,5-dinaphthol do not show any uptake of CO_2 molecules and it could be well explained by its inclusion amount present per pore. But to our surprise, **1** @ DMPT shows uptake of 72

cm^3 g^{-1} indicating sufficient void space even after incorporation of guest molecule considering structural transformation after inclusion.

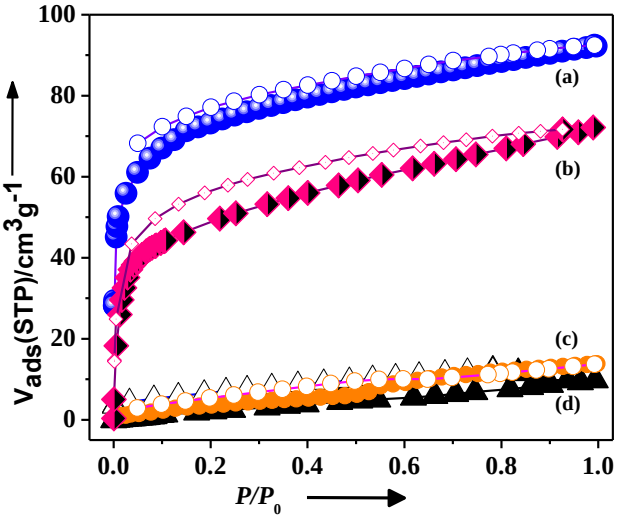

Fig. 8: CO_2 adsorption isotherms at 195 K a. **1** b. **1** @ DMPT c. **1** @ 1,5-dinaphthol c. **1** @ 2,6-dinaphthol.

5.3.5 Luminescence Property

Coordination polymers, especially those with d^{10} metal centres, have been investigated for their luminescent properties and potential applications. Hence, the luminescent properties of **1** and free ligand bpdc were measured in the solid state, as shown in (Fig. 9). The maximum of the emission band is observed at 400 nm (λ_{ex} = 270 nm) for free bpdc at solid state, which is ascribed to the $\pi^* \rightarrow n$ electronic transition of the free ligand. The UV–Vis spectrum of **1** (Fig. 10) in the solid state exhibits a broad absorption and a corresponding green emission (Fig. 11) at 440 nm (λ_{ex} = 255 nm) in the solid state at room temperature. This emission is 40 nm red shifted compared to free bpdc ligand (at solid state) and this can be assigned to ligand to metal charge transfer transition (LMCT).[26-39] Ligand bpNDI does not have any contribution in emission because of its very low fluorescent quantum yield ($\Phi_f \sim 0.003$).[13]

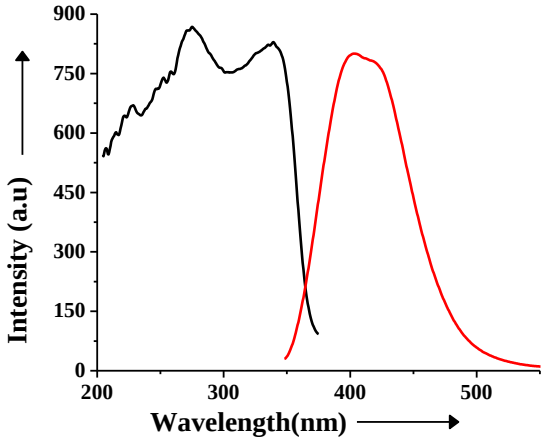

Fig. 9: Black: solid state extitation spectra of bpdc (λ_{ex} = 400 nm) ; Red: solid state emission spectra of bpdc (λ_{ex} = 270 nm).

From (Fig 11), it can be easily visualised that the new red shifted absorption shoulders arise in the lower energy region (within 500 to 700 nm) with respect to the main absorption band of the **1** on inclusion of several guest donor molecules. These new shoulders can be attributed either to the CT complex between the NDI moiety (acceptor or A) and the aromatic guest molecule (donor or D) in the ground state or electron transfer between them with

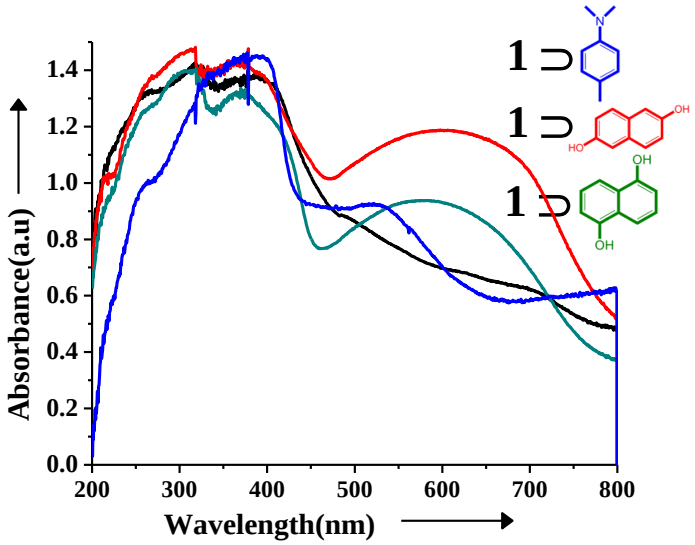

Fig. 10: Solid state absorbance spectra of **1** (black) , **1** @ 1,5-dinaphthol (green), **1** @ 2,6-dinaphthol (red), **1** @ DMPT (blue)

complete charge separated state. To ensure this, electron paramagnetic resonance measurements (EPR) were carried out (Fig. 7a,b,c), for each case and it clearly confirmed one electron transfer from guest to host moiety at room temperature. This broad absorption is most likely attributed to radical ion-pair state of bpNDI [(4)].

The normalized emission spectra (Fig. 11) exhibited different nature compared to the **1**. In case of **1** @ 2,6-dinaphthol there is not such significant peak shifting (λ_{max} = 436 nm)

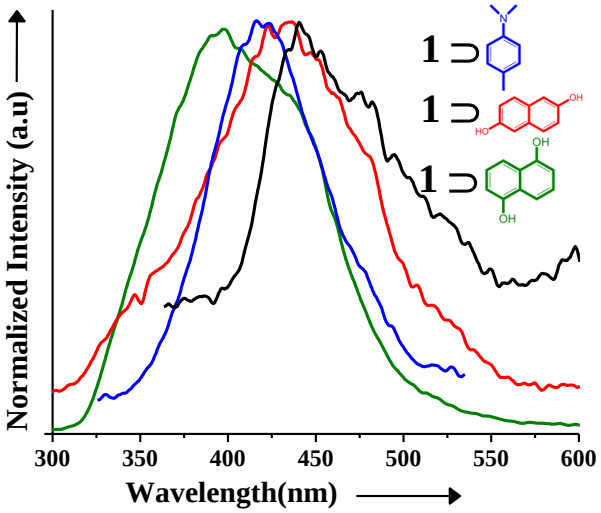

Fig. 11: Solid state emission spectra of **1** (black) , **1** @ 1,5-dinaphthol (green), **1** @ 2,6-dinaphthol (
red), **1** @ DMPT (blue) [(λ_{ex} = 270 nm) in all cases]

with respect to **1** (λ_{max} = 440 nm) and it can be assigned to LMCT transition. But the broad- ness of this peak suggests the contribution from linker based emission as well. But **1** @ DMPT and **1** @ 1,5-dinaphthol luminesces only because of free ligand bpdc. The PXRD pattern of **1** @ 2,6-dinaphthol is practically identical to **1** and the emission also has been found to be closely similar to the host framework. But for **1** @ 1,5-dinaphthol and **1** @ DMPT there are significant changes in PXRD pattern and it could be clearly distinguished from its luminescence shifting.

5.4 Conclusion

In conclusion, we have prepared a new cadmium-based luminescent, photoactive

porous MOF. It shows room temperature one electron transfer through host-guest confinement effect upon inclusion of guest donor molecules. To the best of our knowledge, this would be the first report showing this kind of guest induced electron transfer. Tuning of adsorption after incorporation has been also made possible and well-studied in details. Even after electron transfer it retains its luminescence property which could have important applications in optoelectronic devices. Further research on spectroelectrochemical and conductivity studies are in progress.

5.5 References

1. S. V. Bhosale, C. H. Jani and S. J. Langford, *Chem. Soc. Rev.*, 2008, **37**, 331.

2. E. D. Bloch,; Z. R. Herm, T.-H. Bae and J. R Long, *Chem. Soc. Rev*., 1997, **26** ,365.

3. (*a*) J.-R. Li, J. Sculley and H.-C. Zhou, *Chem. Rev*., 2012, **112**, 869; (*b*) K. Sumida, D. L. Rogow, J. A. Mason, T. M. McDonald, E. D. Bloch, Z. R. Herm, T.-H. Bae and J. R. Long, *Chem. Rev*., 2012, **112**, 724; (*c*) H. Wu, Q. Gong, D. H. Olson and J. Li, *Chem. Rev*., 2012, **112**, 836; (*d*) M. Yoon, R. Srirambalaji and K. Kim, *Chem. Rev*., 2012, **112**, 1196; (*e*) P. Horcajada, R. Gref, T. Baati, P. K. Allan, G. Maurin, P. Couvreur, G. Fe´rey, R. E. Morris and C. Serre, *Chem. Rev*., 2012, **112**, 1232.

4. (*a*) S. Kitagawa, R. Kitaura and S. Noro, *Angew. Chem*., 2004, **116**, 2388; (*b*) C. Janiak, *Dalton Trans*., 2003, 2781; *c*) T. K. Maji and S. Kitagawa, *Pure Appl. Chem*. 2007, **79**, 2155; *d*) G. Fe´rey, *Chem. Soc. Rev*., 2008, **37**, 191; *e*) O. M. Yaghi, M. O_Keeffe, N. W. Ockwig, H. K. Chae and M. Eddaoudi, J. Kim, *Nature*, 2003, **423**, 705.

5. (*a*) A. M. Shultz, O. K. Farha, J. T. Hupp and S. T. Nguyen, *J. Am. Chem. Soc*., 2009, **131**, 4204; (*b*) L. Q. Ma, C. Abney and W. B. Lin, *Chem. Soc., Rev*. 2009, **38**, 1248;

6. (*a*) J. Lee, O. K. Farha, J. Roberts, K. A. Scheidt, S. T. Nguyen and J. T. Hupp, *Chem. Soc., Rev.*, 2009, **38**, 1450; (*b*) D. M. Jiang, A. Urakawa, M. Yulikov, T. Mallat, G. Jeschke and A. Baiker, *Chem. Eur. J*., 2009, **15**, 12255.

7. (*a*) J. R. Li, R. J. Kuppler and H. C. Zhou, *Chem. Soc. Rev*., 2009, **38**, 1477; (*b*) Q. K. Liu, J. P. Ma and Y. B. Dong, *Chem. Eur. J*., 2009, **15**, 10364; (*c*) K. H. Li, D. H. Olson, J. Seidel, T. J. Emge, H. W. Gong, H. P. Zeng and J. Li, *J. Am. Chem. Soc.*, 2009, **131**, 10368; (*d*) C. D. Wu, A. Hu, L. Zhang and W. B. Lin, *J. Am. Chem. Soc*., 2005, **127**, 8940. (*e*) R. Haldar, and T. K. Maji, *CrystEngComm.*, 2012, **14**, 684.

8. (*a*) B. L. Chen, L. B. Wang, Y. Q. Xiao, F. R. Fronczek, M. Xue, Y. J. Cui and G. D. Qian, *Angew. Chem*., 2009, **121**, 508; (*b*) M. Cametti and K. Rissanen, *Chem. Commun*., 2009, **20**, 2809; (*c*) L. G. Qiu, Z. Q. Li, Y. Wu, W. Wang, T. Xu and X. Jiang, *Chem. Commun*.**,** 2008, **31**, 3642.

9. (*a*) P. Kanoo, C. Madhu, G. Mostafa, T. K. Maji, A. Sundaresan, S. K. Pati and C. N. R. Rao, *Dalton Trans*., 2009, 5062; (*b*) Z. M. Wang, K. L. Hu, S. Gao and H. Kobayashi, *Adv. Mater*., 2010, **22**, 1526.

10. (*a*) P. Kanoo, R. Matsuda, M. Higuchi, S. Kitagawa and T. K. Maji, *Chem. Mater*., 2009, **21**, 5861; (*b*) P. Kanoo, K. L. Gurunatha and T. K. Maji, J. Mater. Chem., 2010, **20**, 1322.

11. P. M. Usov , C. Fabian and D. M. D'Alessandro, *Chem. Commun*., 2012, **48**, 3945.

12. (*a*) B.-Q. Ma, K. L. Mulfort, J. T. Hupp, *Inorg. Chem*., 2005, **44**, 4912; (b) K. L. Mulfort and J. T. Hupp, *J. Am. Chem. Soc***.** 2007, **129**, 9604; (c) Y. Takashima, S. Furukawa and S. Kitagawa, *CrystEngComm*, 2011, **13**, 3360.

13.Y.Takashima1, V. M. Martínez, S. Furukawa, M. Kondo, S. Shimomura , H. Uehara , M. Nakahama , K. Sugimoto and S. Kitagawa, *Nat. Commun*., 2011, **2**,168.

14. H. E. Kat, A. J. Lovinger, J. Johnson, C. Kloc, T. Siegrist, W. Li, Y.-Y.Lin and A. Dodabalapur, *Nature*, 2000, **404**, 478.

15. W. W. Stewart, *Nature*, 1981, **292**, 17.

16 (a) M.-S. Wang, G. Xu, Z.-J. Zhang and G.-C. Guo, *Chem. Commun*., 2010, **46**, 361; (b) R. Pardo, M. Zayat and D. Levy, *Chem. Soc. Rev*., 2011, **40**, 672.

17. P. H. Dinolfo, M.E. Williams, C.L. Stern and J. T. Hupp, *J. Am. Chem. Soc*., 2004, **126**, 12989.

18. SMART (V 5.628), SAINT (V 6.45a), Xprep, SHELXTL; Bruker AXS Inc. Madison, Wisconsin, USA, 2004.

19. G. M. Sheldrick, Siemens Area Detector Absorption Correction Program, University of G€otingen, G€otingen, Germany, 1994.

20. A. Altomare, G. Cascarano, C. Giacovazzo and A. Gualaradi, *J. Appl. Crystallogr*., 1993, **26**, 343.

21. G. M. Sheldrick, SHELXL-97, Program for Crystal Structure Solution and Refinement, University of G€otingen, G€otingen, Germany, 1997.

22. A. L. Spek, *J. Appl. Crystallogr*., 2003, **36**, 7.

23. G. M. Sheldrick, SHELXS 97, Program for the Solution of Crystal Structure, University of G€otingen, Germany, 1997.

24. L. J. Farrugia, WinGX-A Windows Program for Crystal Structure Analysis, *J. Appl. Crystallogr*., 1999, **32**, 837.

25. M. M. Dubinin, *Chem. Rev*., 1960, **60**, 235.

26. M. D. Allendorf, C. A. Bauer, R. K. Bhakta, and R. J. T. Houk, *Chem. Soc. Rev*., 2009, **38**, 1330.

27. J.-C. Dai, X.-T. Wu, Z.-Y. Fu, S.-M. Hu, W.-X. Du, C.-P. Cui, L.-M. Wu, H.-H. Zhang and R.-Q. Sun, *Chem. Commun*., 2002, **12**, 12.

28. Q. Fang, G. Zhu, G. W. Xin Shi, R. W. Ge Tian and S. Qiu, *J. Solid State Chem*., 2004, **177**, 1060.

29. J. Fan, H. F. Zhu, T. A. Okamura, W. Y. Sun, W. X. Tang and N. Ueyama, *New J. Chem.*, 2003, **27**, 1409.

30. J.-C. Dai, S.-M. Hu, X.-T. Wu, Z.-Y. Fu, W.-X. Du, H.-H. Zhang and R.-Q. Sun, *New J. Chem*., 2003, **27**, 914.

31. J.-C. Dai, X.-T. Wu, Z.-Y. Fu, C.-P. Cui, S.-M. Hu, W.-X. Du, L.-M. Wu, H.-H. Zhang, and R.-Q. Sun, *Inorg. Chem*., 2002, **41**, 1391.

32. J.-X. Chen, S.-X. Liu and E.-Q. Gao, *Polyhedron.*, 2004, **23**, 1877.

33. E.-C. Yang, J. Li, B. Ding, Q.-Q. Liang, X.-G. Wang and X.-J. Zhao, *CrystEngComm.*, 2008, **10**, 158.

34. K. L. Zhang, H. Y. Gao, Z. C. Pan, W. Liang and G. W. Diao, *Polyhedron.*, 2007, **26**, 5177.

35. M. Du, X. J. Jiang and X. J. Zhao, *Inorg. Chem*., 2007, **46**, 3984.

36. W.-G. Lu, L. Jiang, X.-L. Feng and T.-B. Lu, *Cryst. Growth Des*., 2006, **6**, 564.